To the Graduate Council:

I am submitting herewith a dissertation written by Joshua S. Shimony entitled "Axial Vector Meson Production in Neutrino- Freon Interactions." I have examined the final copy of this document for form and content and recommend that it be accepted in partial fulfillment of the requirements for the degree of Doctor of Philosophy, with a major in Physics.

Wm M. Bugg

William M. Bugg, Major Professor

We have read this dissertation
and recommend its acceptance:

James E. Brau

Edmund L. Hart

George T. Condo

E. Marcia Katz

Accepted for the Council:

C W Minkel

Vice Provost
and Dean of the Graduate School

MESON PRODUCTION IN PHOTON AND NEUTRINO EXPERIMENTS

A Dissertation
Presented for the
Doctor of Philosophy
Degree
The University of Tennessee, Knoxville

Joshua Shai Shimony

August 1988

ACKNOWLEDGEMENTS

I am indebted to many for their assistance in the course of this work. I especially wish to express my gratitude to the following:

To Bill Bugg, thank you for the many hours dedicated to this work under the constraints of a busy schedule, for the many useful comments and suggestions, and for being a mentor and a friend.

To Jim Brau, thank you for guidance during the BC 72-73 work, for suggesting a thesis topic that made everything fit together, and for useful comments on this work.

To George Condo, for patient reading of my pour Inglish in early drafts of this work, useful comments, and honest advice throughout.

To Tom Handler, for comments on the early drafts, and computer help all along.

To Ed Hart and Hans Cohn, for your comments on this work, and for running the scanning and measuring operation.

To Joe Hargis, for computer assistance from the beginning.

To Kevin Pitts, for the state of the art 3D graphics in this work, and some tough running workouts. FA!

To Kaushik De and John Harton, for sharing long grave yard shifts, fast food dinners, useful advice, and companionship.

To the scanning crew, for their work on the data.

To the University of Tennessee High Energy Physics group, for generous financial support.

To the University of Tennessee for a great educational environment — Go Vols!

On a personal note:

To Becky, thank you for your love, patience, and support (not to mention the typing, and editing). I couldn't have done it without you.

To my parents Uri and Haya, my grandmother Rivka, my brothers Ilan, Yuval, and Benny, thank you for your love, support, and a wonderful environment to grow up in (not to mention tuition).

Finally I wish to dedicate this work to the memory of my grandparents: Moshe, Shifra, Joshua, and Yehuda.

ABSTRACT

The reaction $\gamma p \rightarrow \rho^0_{fast} p\pi^+\pi^-$ has been studied with the linearly polarized 20 GeV monochromatic photon beam at the SLAC Hybrid Facility, to test the prediction of s channel helicity conservation in inelastic diffraction for $t' < 0.4(GeV/c)^2$. In a sample of 1934 events from this reaction, the ρ^0 decay angular distributions and spin density matrix elements are consistent with s channel helicity conservation. The $\pi^+\pi^-$ mass shape displays the same skewing as seen in the reaction $\gamma p \rightarrow p\pi^+\pi^-$, and the $p\pi^+\pi^-$ mass distribution compares well and scales according to the vector dominance model with that produced in $\pi^\pm p \rightarrow p\pi^+\pi^-$.

Coherent production of the a_1 meson has been observed through the reaction $\nu Fr \rightarrow \mu^- a_1^+ Fr$ in the Tohoku 1m freon bubble chamber hybrid system. The bubble chamber was exposed to the Fermilab wide-band neutrino beam, generated by 800 GeV protons at the Tevatron. The observed rate from the final charged current sample of 1792 events was $1.1 \pm 0.47\%$, and the $a_1 - W$ coupling is calculated to be $f_a^2/f_\rho^2 = 5.2 \pm 2.2$. A comparison of the cross section and the kinematical parameters with the theoretical predictions of the vector dominance model, gives reasonable agreement with the data.

A Monte-Carlo study was performed to check the possibility of detecting the radiative decay of the D_s^* in our bubble chamber. Using the most favorable predicted rate through the ϕ branching ratio, it was determined that three times our data sample would be needed for a one σ effect above background.

Contents

List of Figures

List of Tables

CHAPTER 1

INTRODUCTION

On an elementary level, a high energy physics experiment involves colliding elementary particles and observing the produced debris. The neutrino and the photon, both point-like particles that only react through the electroweak force, are an excellent choice for beam particles because of their simplicity, and indeed both neutrino experiments and photoproduction experiments have contributed significantly to our understanding of matter and the forces that hold it together.

The data used in this thesis was obtained from two experiments. A photoproduction experiment, BC 72-73 at SLAC, and a neutrino experiment, E745 at Fermilab. In BC 72-73, the SLAC Hybrid Facility consisting of a 40-in. hydrogen bubble chamber and a downstream detector system, was exposed to a linearly polarized photon beam backscattered from the SLAC 30 GeV primary electron beam. In E745, the Tohoku 1m freon bubble chamber and its downstream system were exposed to the Fermilab wide-band neutrino beam produced, using 800 GeV protons from the Tevatron. Most of the E745 data was generated during the 1985 run, but some data from the 1988 run was also included as it became available.

The early analysis on BC 72-73 involved a test of the Vector Dominance Model (VDM). The VDM, first introduced by Sakurai [2], proposes to explain the diffractive hadronic interactions of the photon by hypothesizing that the photon converts into a vector meson [3]. Several authors [4,5,6,7,8] have predicted the extension of the VDM to the weak interactions; instead of the photon, the intermediate vector boson converts into vector and axial vector mesons. This served as a motivation to continue work on the VDM in the E745 neutrino experiment also.

Chapter 2 will cover theoretical aspects of the model needed for the experimental work that follows. Chapter 3 describes the experimental apparatus of E745. The author joined BC 72-73 at the very end of its run, so only a brief experimental description is offered in the result chapter. Chapter 4 concerns the data hybridization process - connecting the bubble chamber data with the electronic data. The preliminary steps of the data analysis and the charged current selection cuts are presented in Chapter 5. Chapter 6 contains the BC 72-73 results, Chapter 7, the E745 results, and Chapter 8, the summary and conclusion.

CHAPTER 2

THEORY

This chapter will first describe the naive quark-parton model (QPM) and introduce the important kinematical variables involved in deep inelastic lepton nucleon scattering. The vector meson dominance model (VDM) will also be introduced and its cross section predictions for vector meson production will be discussed. Because of their importance to the interpretation of experimental data the decay angular distributions of vector mesons produced by photons, leptons and neutrinos will be discussed in detail. The effect of s-channel helicity conservation (SCHC) on the decay distributions will also be considered.

2.1 The Quark Parton Model and Kinematics

In the QPM, the target nucleon is assumed to be made of three valence quarks bound by the strong interaction. The quarks are spin one half, point-like objects that come in several flavors. The target nucleons, the proton and neutron, are made from only the up quark (charge $+\frac{2}{3}$) and the down quark (charge $-\frac{1}{3}$). We define the following four momentum vectors in the interaction (Fig. 2.1):

1. The incoming neutrino (or lepton) $l = (E_\nu, \vec{p}_\nu)$.

2. The outgoing muon (or lepton) $l' = (E_\mu, \vec{p}_\mu)$.

3. The target nucleon $P = (M, \vec{n})$.

4. The outgoing nucleon system $P' = (M', \vec{n'})$.

5. The vector meson $v = (m_V, \vec{v})$.

6. The momentum transfer $q = l - l' = (\nu, \vec{q}) = (E_\nu - E_\mu, \vec{p}_\nu - \vec{p}_\mu)$.

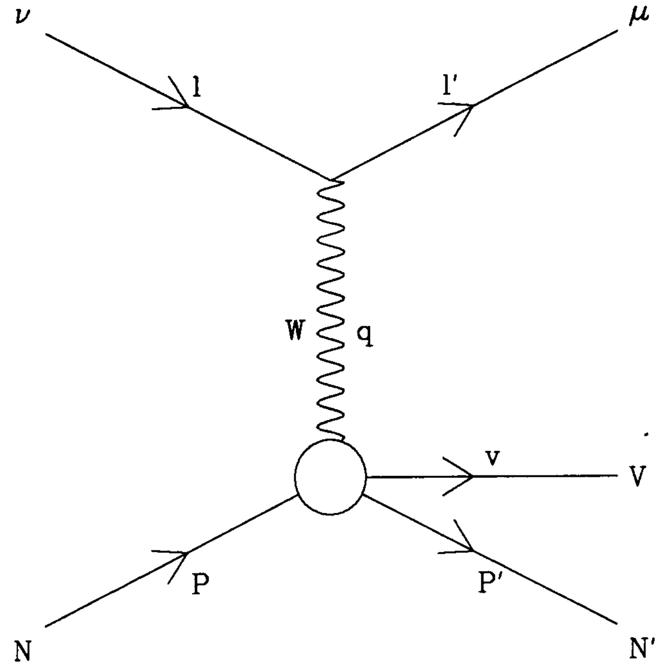

Figure 2.1: Feynman diagram for $\nu + N \rightarrow \mu + N' + V$

The Fermi motion of the nucleon is neglected so in the lab frame $\vec{n} = 0$. The momentum transfer squared Q^2 is defined as

$$\begin{aligned} Q^2 = -q^2 &= (\vec{p_\nu} - \vec{p_\mu})^2 - (E_\nu - E_\mu)^2 \\ &= 2E_\nu E_\mu - 2\vec{p_\nu} \cdot \vec{p_\mu} - m_\mu^2 \\ &= 2E_\nu E_\mu (1 - \beta_\mu \cos\theta) - m_\mu^2, \end{aligned} \tag{2.1}$$

where θ is the angle between the muon and neutrino and β_μ is the muon velocity. Since $2E_\nu E_\mu(1-\beta_\mu) > m_\mu^2$, q^2 is always negative and Q^2 is always positive. The hadronic mass after the collision W^2 is defined as

$$\begin{aligned} W^2 = (P+q)^2 &= M^2 + 2P\cdot q + q^2 \\ &= M^2 + 2M\nu - Q^2. \end{aligned} \tag{2.2}$$

Since conservation of baryon number requires that among the hadrons produced there be at least a nucleon $W \geq M$, this implies that $P \cdot q = M\nu = M(E_\nu - E_\mu) > 0$. Two more important normalized variables introduced by Bjorken are very helpful in the event analysis. The first is

$$y = \frac{P\cdot q}{P\cdot l} = \frac{\nu}{E_\nu} = 1 - \frac{E_\mu}{E_\nu}. \tag{2.3}$$

y can be understood as the fraction of the neutrino energy transferred to the nucleus. It is clear from conservation of energy that y can only take values from zero to one. The second variable is

$$x = \frac{Q^2}{2P\cdot q} = \frac{Q^2}{2M\nu} = 1 - \frac{W^2 - M^2}{2M\nu}. \tag{2.4}$$

From the last form, one can see that x also only takes values between zero and one. To understand the interpretation of x, the QPM is useful (for a detailed treatment of the QPM see [14]). The QPM assumes that only one of the quarks is struck elastically by the neutrino, since they are both point like particles. The struck quark and the remaining di-quark proceed to fragment into particles that are detected. The x in this model can be interpreted as the fraction of the four momentum of the nucleon that was carried by the struck quark giving for that four momentum xP. After the collision, the quark momentum will be $xP + q$, but because of the elastic collision assumption, the mass of the quark does not change. Equating the mass squared before and after:

$$x^2P^2 = (xP + q)^2 = x^2P^2 + 2xP \cdot q + q^2, \tag{2.5}$$

and then solving for x:

$$x = \frac{-q^2}{2P \cdot q}, \tag{2.6}$$

which is the same as the previous result for x. This analysis is only an approximation since the more energetic the collision the higher the chances for the emission of a radiative photon or gluon that will reduce the measured x compared to the real x.

2.2 The Vector Dominance Model

The VDM, first introduced by Sakurai [2], has been used for years to describe the diffractive interactions of photons and leptons with nucleons [3]. In the model, the photon or virtual photon, transforms into a transverse vector meson which interacts with the nucleon. Several theoretical papers predict [4,5,6,7,8] an analogous process in the weak interactions, where the weak current (intermediate vector boson) couples to a vector or axial-vector meson, which interacts diffractively with the nucleon (Fig. 2.1). In diffractive scattering, pomeron (vacuum) exchange dominates, and this can reveal information on the structure of the weak currents. QCD-based models of the pomeron, such as two gluon exchange, lead naturally to SCHC [9], which will be discussed later. The derivation of the cross section follows the treatment of Piketty and Stodolsky [4].

The matrix element between the initial and final state for the scattering process presented in Fig. 2.1 is given by (with G the Fermi coupling constant):

$$M = L_\mu H^\mu = \frac{G}{\sqrt{2}} \langle l' | j_\mu | l \rangle \langle P', v | J^\mu | P \rangle, \tag{2.7}$$

where L_μ, j_μ are the leptonic matrix element and current and H^μ, J^μ are the hadronic matrix element and current. The hadronic matrix element is made of a vector and an axial-vector component:

$$\begin{aligned} L_\mu &= \frac{G}{\sqrt{2}} \bar{u}(l') \gamma_\mu (1 - \gamma_5) u(l), \qquad (2.8) \\ H^\mu &= \langle P', v | V^\mu + A^\mu | P \rangle = V^\mu + A^\mu. \end{aligned}$$

The final cross section is derived from averaging over initial states and summing over the final states of the square of the matrix element:

$$\sigma \propto \overline{\sum_i} \sum_f |M|^2 = L_{\mu\nu} H^{\mu\nu}. \tag{2.9}$$

The result factors into two independent tensors with

$$\begin{aligned} L_{\mu\nu} &= \frac{2G^2}{m_\mu} [l_\mu l'_\nu + l_\nu l'_\mu - (l \cdot l') g_{\mu\nu} \mp \epsilon_{\mu\nu\alpha\beta} l^\alpha l'^\beta], \qquad (2.10) \\ H^{\mu\nu} &= \overline{\sum_i} \sum_f H^{\mu *} H^\nu \qquad (2.11) \\ &= \overline{\sum_i} \sum_f V^{\mu *} V^\nu + V^{\mu *} A^\nu + A^{\mu *} V^\nu + A^{\mu *} A^\nu, \end{aligned}$$

where the $\mp$ refers to ν and $\bar{\nu}$. The explicit form of $H_{\mu\nu}$ is unknown. Lorentz invariance, hermiticity, and a hypothesis on current conservation, (conservation of vector current (CVC), partial conservation of axial current (PCAC)), place constraints on the final form of $H_{\mu\nu}$. Each term in $H_{\mu\nu}$ has unique features, and will be treated separately. It should be noted that for the electromagnetic scattering case, the tensors are very similar: $L_{\mu\nu}$ has a different coupling constant and does not have the antisymmetric tensor $\epsilon_{\mu\nu\alpha\beta}$, and $H_{\mu\nu}$ has only the vector contribution.

2.2.1 Vector-Vector Term

After the summations, the only independent four vectors left in the problem are P_μ and q_μ, leaving the most general form for a tensor $H_{\mu\nu}(VV)$ as

$$\begin{aligned} H_{\mu\nu}(VV) &= F_0^v(q^2,\nu)[g_{\mu\nu} - \frac{P_\mu q_\nu + P_\nu q_\mu}{P\cdot q} + q^2\frac{P_\mu P_\nu}{(P\cdot q)^2}] \\ &+ F_1^v(q^2,\nu)[q_\mu q_\nu - q^2\frac{P_\mu q_\nu + P_\nu q_\mu}{P\cdot q} + q^4\frac{P_\mu P_\nu}{(P\cdot q)^2}], \end{aligned} \tag{2.12}$$

where F_0^v, F_1^v are scalar functions of q^2 and ν. In electromagnetic scattering, the terms proportional to q_μ give no contribution, because of conservation of the electromagnetic current and the massless photon. In weak vector scattering, the terms proportional to q_μ will give small contributions to the cross section that are of the order m_μ^2/m_V^2, where m_V is the mass of the vector meson. With this assumption, the resulting cross-section for the vector current is similar to electromagnetism:

$$\frac{d^2\sigma^v}{dq^2 d\nu} = \frac{G^2}{4\pi^2 E^2}[F_0^v q^2 + (F_0^v + q^2 F_1^v)\frac{q^2}{2\nu^2}(4E_\nu E_\mu - q^2)]. \tag{2.13}$$

Using the VDM, we insert the ρ dominance of the vector current:

$$V_\mu = \frac{f_\rho}{q^2+m_\rho^2}[g_{\mu\lambda} + \frac{q_\mu q_\lambda}{m_\rho^2}]\epsilon_\lambda^i T_\lambda^{(\rho\to f)}, \tag{2.14}$$

where f_ρ is the lepton-ρ coupling and $\epsilon_\lambda^i T_\lambda^{(\rho\to f)}$ describes the production amplitude of the final state from a ρ with polarization i. Using the CVC hypothesis $q_\lambda T_\lambda = 0$ gives

$$H_{\mu\nu}(VV) = \frac{f_\rho^2}{(q^2+m_\rho^2)^2}T_{\mu\nu}, \tag{2.15}$$

where $T_{\mu\nu}$ is defined as

$$T_{\mu\nu} = \overline{\sum_i}\sum_f T_\mu^{\rho*}T_\nu^\rho. \tag{2.16}$$

Defining the polarized cross section for transverse and longitudinal currents:

$$\sigma_T = \frac{1}{|\vec{q}|}T_{\mu\nu}\epsilon_\mu^{T*}\epsilon_\nu^T, \qquad \sigma_L = \frac{1}{|\vec{q}|}T_{\mu\nu}\epsilon_\mu^{L*}\epsilon_\nu^L, \tag{2.17}$$

where $|\vec{q}|$ is a flux factor, and the polarization vectors being:

$$\epsilon_T = (\vec{\epsilon}_T, \epsilon_T^0), \quad \vec{\epsilon}_T \cdot \vec{q} = 0, \quad \epsilon_T^0 = 0, \quad \epsilon_T^2 = \pm 1, \tag{2.18}$$

$$\epsilon_L = (\vec{\epsilon}_L, \epsilon_L^0) = \frac{1}{\sqrt{|q^2|}}(q_0\hat{q}, |\vec{q}|), \quad \epsilon_L^2 = \pm 1. \tag{2.19}$$

The differential cross section then becomes

$$\frac{d^2\sigma^\rho}{dq^2 d\nu} = \frac{G^2}{4\pi^2 E^2}\frac{f_\rho^2 q^2}{(q^2+m_\rho^2)^2}|\vec{q}|[\sigma_T^\rho + \frac{\sigma_T^\rho + \sigma_L^\rho}{2|\vec{q}|^2}(4E_\nu E_\mu - q^2)]. \tag{2.20}$$

2.2.2 Axial-Axial Term

As in the vector-vector case, the most general form for a Tensor $H_{\mu\nu}(AA)$ is

$$H_{\mu\nu}(AA) = F_0^a g_{\mu\nu} + F_1^a P_\mu P_\nu + F_2^a(P_\mu q_\nu + P_\nu q_\mu) + F_3^a q_\mu q_\nu. \tag{2.21}$$

Like in the previous case, negligible terms arise that are proportional to the square of the lepton mass. A difference that arises in the axial case comes from the PCAC hypothesis: $\partial A_\mu = f_\pi \Phi$ with Φ representing the π field. Unlike the vector case, the axial current is only partially conserved, and this gives rise to terms from pion exchange. Fortunately, the pion propagator becomes negligible when q^2 is larger than m_π^2, which is the case for most of our data. Thus neglecting the small contributions, the expression for the axial cross section is similar to the vector case:

$$\frac{d^2\sigma^a}{dq^2 d\nu} = \frac{G^2}{4\pi^2 E^2}[F_0^a q^2 + \frac{1}{2}F_1^a M^2(4E_\nu E_\mu - q^2)]. \tag{2.22}$$

Within the framework of the VDM, the axial current is dominated by the a_1 and the π:

$$A_\mu = \frac{f_a}{q^2+m_a^2}[g_{\lambda\mu} + \frac{q_\lambda q_\mu}{m_a^2}]\epsilon_\lambda^i T_\lambda^{(a\to f)} + \frac{f_\pi q_\mu}{q^2+m_\pi^2}T^{(\pi\to f)}. \tag{2.23}$$

The interference term between the π and a_1 and the diagonal π term, give contributions of the order of previously neglected terms, so will not be considered further. The diagonal a_1 term gives a contribution similar to the ρ term:

$$\frac{d^2\sigma^a}{dq^2 d\nu} = \frac{G^2}{4\pi^2 E^2} \frac{f_{la}^2 q^2}{(q^2+m_a^2)^2} |\vec{q}| [\sigma_T^a + \frac{\sigma_T^a + \sigma_L^a}{2|\vec{q}|^2}(4E_\nu E_\mu - q^2)]. \tag{2.24}$$

2.2.3 Vector-Axial Term

From Lorentz invariance and the negative parity of the VA contribution the only contributing term is

$$H_{\mu\nu}(VA) = \overline{\sum_i} \sum_f A_\mu^* V_\nu = \frac{G_1(q^2,\nu)}{M^2} \epsilon_{\mu\nu\alpha\beta} P_\alpha q_\beta, \tag{2.25}$$

giving for the cross section for the ν and $\bar{\nu}$:

$$\frac{d^2\sigma^{va}}{dq^2 d\nu} = \pm \frac{G^2}{2\pi^2 M E_\nu} G_1 q^2. \tag{2.26}$$

Using VDM, while neglecting the π and longitudinal a_1 contributions, the form factor G_1 is

$$G_1 = \frac{M}{|\vec{q}|} \frac{f_a}{q^2+m_a^2} \frac{f_\rho}{q^2+m_\rho^2} \left[\overline{\sum_i} \sum_f T_\nu^{a*} \cdot \epsilon_\nu^{T*}(a) T_\mu^\rho \cdot \epsilon_\mu^T(\rho) \right]. \tag{2.27}$$

The generalized Schwartz inequality can be used to find an upper limit on this contribution to the cross section. Writing the expression in square brackets above as a scalar product of two generalized vectors in Dirac notation, the inequality can be used:

$$\sum_f \langle \mathcal{N} | A_\nu^* \cdot \epsilon_\nu^{T*} | f \rangle \langle f | V_\mu \cdot \epsilon_\mu^T | \mathcal{N} \rangle \leq \sqrt{\sum_f |\langle f | A_\nu \cdot \epsilon_\nu^T | n \rangle|^2 \sum_f |\langle f | V_\mu \cdot \epsilon_\mu^T | n \rangle|^2}. \tag{2.28}$$

In terms of previously defined form factors:

$$|G_1(q^2,\nu)| \frac{M}{|\vec{q}|} \leq \sqrt{F_0^v(q^2,\nu) F_0^a(q^2,\nu)}, \tag{2.29}$$

which provides an upper limit allowing us to neglect the VA interference cross section:

$$\frac{d^2\sigma^{va}}{dq^2 d\nu} \leq \frac{G^2}{\pi^2 E_\nu} \frac{f_a f_\rho}{(q^2+m_a^2)(q^2+m_\rho^2)} q^2 \sqrt{\sigma_T^\rho \sigma_T^a}. \tag{2.30}$$

2.2.4 The Diffractive Cross Section

Slight changes are made to the previously derived cross section to bring it to a more convenient form. Since the coherent cross section is strongly dependent on t, the four momentum transfer to the nucleus, the t dependence is inserted into the transverse and longitudinal cross section. For convenience, the following definitions are used:

$$R = \frac{d\sigma_L/dt}{d\sigma_T/dt} \tag{2.31}$$

$$\alpha = \frac{4E_\nu E_\mu - q^2}{2|\vec{q}|^2} = \frac{4E_\nu(E_\nu - \nu) - Q^2}{2(Q^2 + \nu^2)} \tag{2.32}$$

$$\epsilon = \frac{\alpha}{1+\alpha} = \frac{4E_\nu(E_\nu - \nu) - Q^2}{4E_\nu(E_\nu - \nu) + Q^2 + 2\nu^2}, \tag{2.33}$$

where R is the ratio of the longitudinal to transverse cross section, and ϵ is the polarization of the intermediate vector boson. Using these in the previously defined expressions, gives

$$\frac{d^3\sigma}{dt dQ^2 d\nu} = \frac{G^2 f_v^2}{4\pi^2 E_\nu^2}\left(\frac{1}{Q^2 + m_v^2}\right)^2 \frac{Q^2\nu(1+\epsilon R)}{1-\epsilon}\frac{d\sigma_T}{dt}, \tag{2.34}$$

where a flux factor of $|\vec{q}| = \nu$ is used. The cross section is correct for vector and axial vector mesons with $q^2 > m_\pi^2$.

2.3 Decay Angular Distributions of Vector Mesons

The derivation of the decay angular distributions for vector mesons is presented in parallel for three different cases: photoproduction, leptoproduction, and neutrino interactions. The photoproduction case is presented as a derivation to complement the Appendix, and as a simple case from which to derive the more complex distributions in leptoproduction and neutrino interactions. The derivation follows the papers of Schilling, Seyboth and Wolf [10,11].

2.3.1 The Coordinate System

The production of the vector meson is defined in the center of mass system. The z-axis is defined as the direction of the interacting particle, $\vec{q}$, which can be a photon or the intermediate vector boson. This, and the direction of the vector meson, $\vec{v}$, define the production plane. Using these to define a right handed coordinate system:

$$\hat{z} = \frac{\vec{q}}{|\vec{q}|}, \quad \hat{y} = \frac{\vec{q} \times \vec{v}}{|\vec{q} \times \vec{v}|}, \quad \hat{x} = \hat{y} \times \hat{z}, \tag{2.35}$$

where the hat indicates a unit vector. A detailed view of the coordinate system for photoproduction is presented in Fig. 2.2

The decay of the vector meson is defined in its rest frame (the helicity system). The z-axis of this frame is chosen opposite to the direction of the outgoing hadrons (or along the direction of motion of the meson in the center mass system). The y-axis is picked to be the same as before, and the x-axis follows:

$$\hat{z}' = \frac{\vec{v}}{|\vec{v}|}, \quad \hat{y}' = \hat{y}, \quad \hat{x}' = \hat{y}' \times \hat{z}'. \tag{2.36}$$

The decay angles θ, ϕ are defined as the polar and azimuthal angles of the decay vector $\hat{\pi}$, which describes the decay of the vector meson. For a two-particle decay, $\hat{\pi}$ is the direction of one of the decay products. For a three-particle decay, the analyzing vector is taken as the normal to the decay plane. The definitions for θ, ϕ are

$$\cos\theta = \hat{\pi} \cdot \hat{z}', \quad \cos\phi = \frac{\hat{y}' \cdot (\hat{z}' \times \hat{\pi})}{|\hat{z}' \times \hat{\pi}|}, \quad \sin\phi = -\frac{\hat{x}' \cdot (\hat{z}' \times \hat{\pi})}{|\hat{z}' \times \hat{\pi}|}. \tag{2.37}$$

2.3.2 The Photon Density Matrix - Real Photons

The photon density matrix is constructed in terms of the photon wave function $|\gamma\rangle$ in the helicity basis:

$$|\gamma\rangle = a_+ \,|+1\rangle + a_- \,|-1\rangle\,, \tag{2.38}$$

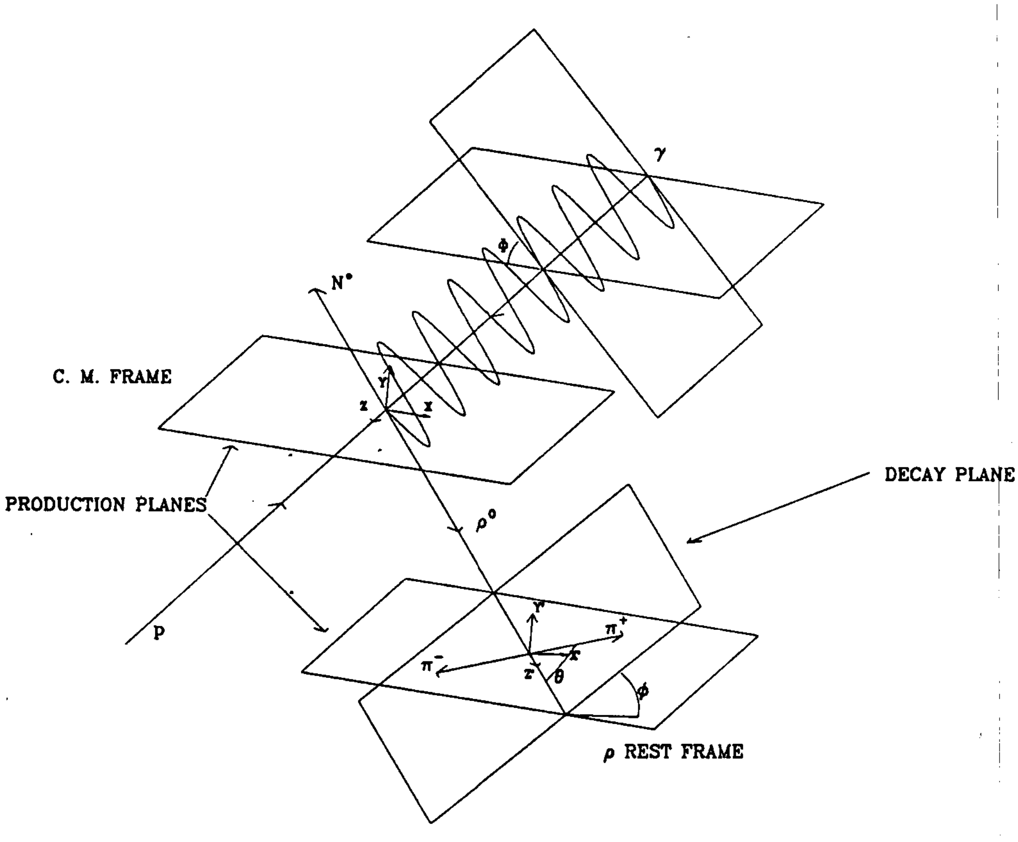

Figure 2.2: The definition of the coordinate system for photoproduction of vector mesons with an example of a two body decay.

where ± 1 denote the photon helicity:

$$||\pm 1\rangle|^2 = 1 \;, \quad |a_+|^2 + |a_-|^2 = 1, \tag{2.39}$$

which gives

$$\rho(\gamma) = |\gamma\rangle\langle\gamma| = \begin{pmatrix} |a_+|^2 & a_+a_-^* \\ a_-a_+^* & |a_-|^2 \end{pmatrix}. \tag{2.40}$$

For linearly polarized photons, the photon wave function takes the form

$$|\gamma\rangle = -\frac{1}{\sqrt{2}}(e^{-i\Phi}|+1\rangle - e^{i\Phi}|-1\rangle), \tag{2.41}$$

where Φ is the angle between $\epsilon = (\cos\Phi, \sin\Phi, 0)$, the polarization vector of the photon, and the production plane (see Fig. 2.2). This leads to a photon density matrix of the form

$$\rho(\gamma) = \frac{1}{2}\begin{pmatrix} 1 & -e^{-2i\Phi} \\ -e^{2i\Phi} & 1 \end{pmatrix} = \frac{1}{2}I + \frac{1}{2}\vec{P}_\gamma \cdot \vec{\sigma} \tag{2.42}$$

where in the second form the density matrix is decomposed in terms of the Pauli and Unit matrices and P_γ is

$$\vec{P}_\gamma = P_\gamma(-\cos 2\Phi, -\sin 2\Phi, 0) \tag{2.43}$$

The length of P_γ is set equal to the degree of polarization, and is between zero and one. Note, that for real photons with only two helicity states, the density matrix can be a two-by-two matrix; this will not be true in the next section.

2.3.3 The Leptonic Density Matrix - Virtual Particles

A virtual photon, or intermediate vector boson, can have transverse components, which complicate the calculation considerably and lead to a different definition of the polarization angle Φ. The angle Φ is defined as the angle between the normal to the lepton plane in the center of mass:

$$\hat{n}_l = \frac{\vec{l} \times \vec{l'}}{|\vec{l} \times \vec{l'}|}, \tag{2.44}$$

and the normal to the hadron production plane $\hat{y}$:

$$\cos\Phi = \hat{n}_l \cdot \hat{y}, \quad \sin\Phi = \frac{((\hat{y}\times\hat{n}_l)\times\hat{y})\cdot\hat{n}_l}{|(\hat{y}\times\hat{n}_l)\times\hat{y})|}. \tag{2.45}$$

The coordinate system for neutrino interactions is presented in Fig. 2.3 with an example of a three body decay.

The leptonic tensor presented earlier (up to leading constants)

$$L_{\mu\nu} = [l_\mu l'_\nu + l_\nu l'_\mu - (l\cdot l')g_{\mu\nu} \mp \epsilon_{\mu\nu\alpha\beta} l^\alpha l'^\beta], \tag{2.46}$$

describes the spin state of the leptonic vertex, and can be interpreted as the spin density matrix up to a flux normalization constant. To simplify the leptonic tensor calculation, we use a coordinate system in which $\vec{q}$ points along the z-axis and the leptonic plane is rotated to lie in the x,z plane. The transverse components of the leptonic tensor do not change under a Lorentz boost in the direction of $\vec{q}$. The longitudinal and scalar components transform into one another, so the scalar component can be eliminated by using current conservation:

$$q_\mu j^\mu = q_3 j^3 - q_0 j^0 = 0 \rightarrow j^0 = \frac{q_3}{q_0} j^3 \tag{2.47}$$

with a similar result for the hadronic current $q_\mu J^\mu = 0$. This gives for example:

$$\begin{aligned} j_\mu J^\mu &= j_1 J^1 + j_2 J^2 + j_3 J^3 - j_0 J^0 \\ &= j_1 J^1 + j_2 J^2 + j_3 J^3 (1 - \frac{q_3^2}{q_0^2}) \\ &= j_1 J^1 + j_2 J^2 - \frac{Q^2}{q_0^2} j_3 J^3. \end{aligned} \tag{2.48}$$

This example demonstrates that using the substitution

$$j_\mu = (j_1, j_2, j_3, j_0) \rightarrow j'_\mu = (j_1, j_2, -\frac{Q}{q_0} j_3, 0), \tag{2.49}$$

$$J_\mu = (J_1, J_2, J_3, J_0) \rightarrow J'_\mu = (J_1, J_2, +\frac{Q}{q_0} J_3, 0), \tag{2.50}$$

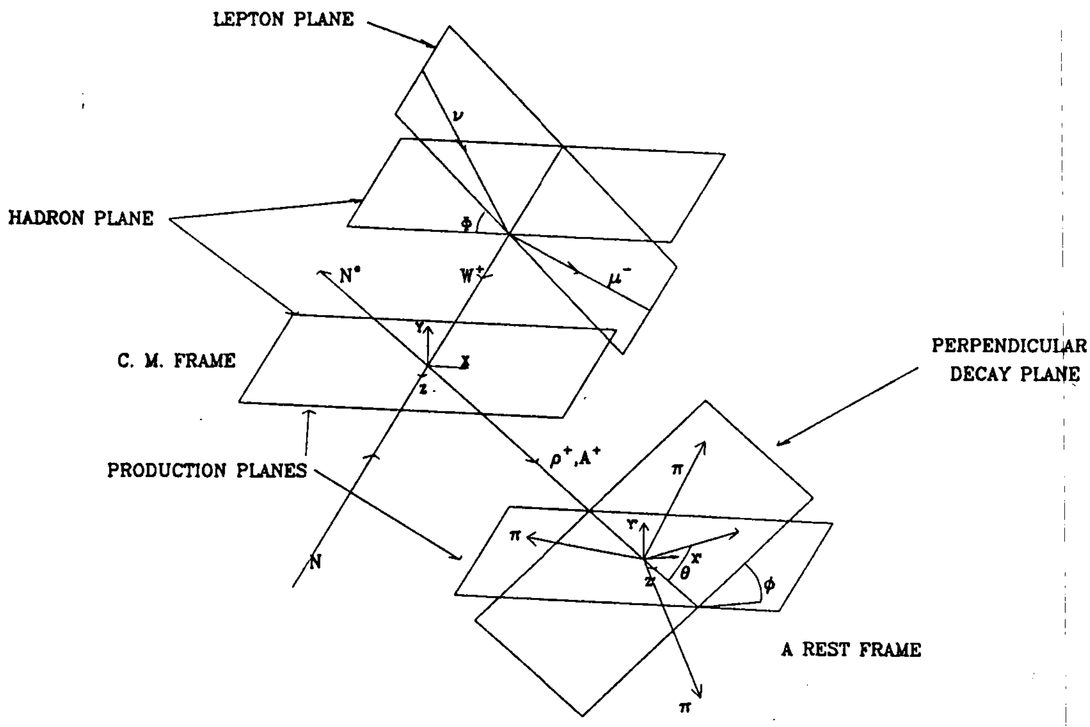

Figure 2.3: The definition of the coordinate system for neutrino production of vector meson with an example of a three body decay

will not change any of the final results. The new tensor will become

$$L_{\mu\nu} \rightarrow L_{\mu\nu} \times \begin{cases} 1 & \mu \text{ and } \nu \neq 3 \\ -Q/q_0 & \mu \text{ or } \nu = 3 \\ (Q/q_0)^2 & \mu \text{ and } \nu = 3 \end{cases} \tag{2.51}$$

$$H_{\mu\nu} \rightarrow H_{\mu\nu} \times \begin{cases} 1 & \mu \text{ and } \nu \neq 3 \\ +Q/q_0 & \mu \text{ or } \nu = 3 \\ (Q/q_0)^2 & \mu \text{ and } \nu = 3 \end{cases} \tag{2.52}$$

The polarization of a physical spin 1 particle is invariant under a Lorentz boost. This is also the case with the spin density matrix [11]. This enables us to transform to the Breit frame, which is a convenient frame to evaluate the matrix. In the Breit frame the energy components of the leptons are equal: $l = (l_x, 0, l_z, l_0)$, $l' = (l_x, 0, -l_z, l_0)$, $q = (0, 0, 2l_z = q, 0)$. The leptonic tensor has a symmetric and an antisymmetric part; the antisymmetric contribution comes from the completely polarized neutrinos (or polarized leptoproduction), and will be dealt with later. The symmetric leptonic tensor evaluated in this frame is [11]

$$L^s_{\mu\nu} = 2\begin{pmatrix} l_x^2 + \frac{1}{4}Q^2 & 0 & -l_x\sqrt{l_x^2 + m^2 + \frac{1}{4}Q^2} \\ & \frac{1}{4}Q^2 & 0 \\ & & l_x^2 + m^2 \end{pmatrix} \tag{2.53}$$

$$= \frac{Q^2}{1-\epsilon}\begin{pmatrix} \frac{1}{2}(1+\epsilon) & 0 & \sqrt{\frac{1}{2}\epsilon(1+\epsilon+2\delta)} \\ & \frac{1}{2}(1-\epsilon) & 0 \\ & & \epsilon+\delta \end{pmatrix}, \tag{2.54}$$

where ϵ is the polarization parameter defined by

$$\frac{L_{11}}{L_{12}} = \frac{1+\epsilon}{1-\epsilon} \rightarrow \epsilon = \frac{2l_x^2}{2l_x^2 + Q^2}, \tag{2.55}$$

and δ is a lepton mass term $\delta = 2m_\mu^2/Q^2(1-\epsilon)$, which will be neglected, since for our experiment $Q^2 \gg m_\mu^2$. Evaluating ϵ in terms of lab frame variables give the result quoted earlier in Eq. 2.33.

Since $L^s_{\mu\nu}$ is invariant under a Lorentz boost, this expression is true in the center of mass frame. Finally, to reach the helicity frame, we convert into spherical coordinates and rotate around the z-axis by the angle Φ:

$$L_{\lambda\lambda'} = U_{\lambda\mu} L_{\mu\lambda} U^{-1}_{\nu\lambda'}, \tag{2.56}$$

where λ, λ' denote the photon helicity and U is the rotation matrix:

$$U_{\lambda\mu} = \frac{1}{\sqrt{2}} \begin{pmatrix} -e^{-i\Phi} & -ie^{-i\Phi} & 0 \\ 0 & 0 & \sqrt{2} \\ e^{-i\Phi} & -ie^{-i\Phi} & 0 \end{pmatrix}, \quad U^{-1}_{\mu\lambda} = U^{\dagger}_{\mu\lambda}. \tag{2.57}$$

The final form for the hermitian photon spin density matrix is

$$L^s_{\lambda\lambda'} = \frac{Q^2}{2(1-\epsilon)} \begin{pmatrix} 1 & \sqrt{\epsilon(1+\epsilon+2\delta)}e^{-i\Phi} & -\epsilon e^{-2i\Phi} \\ & 2(\epsilon+\delta) & -\sqrt{\epsilon(1+\epsilon+2\delta)}e^{-i\Phi} \\ & & 1 \end{pmatrix}. \tag{2.58}$$

2.3.4 The Leptonic Density Matrix - Polarized Part

As mentioned earlier, the polarization of the beam leads to an antisymmetric part of the density matrix. The neutrino results will be quoted in this section as a special case of the more general treatment for a polarized lepton. The lepton polarization vector in the lepton rest frame can be expressed as

$$P^{rest}_{\mu} = P(\ \sin\theta_p \cos\phi_p,\ \sin\theta_p \sin\phi_p,\ \cos\theta_p,\ 0) \tag{2.59}$$

where θ_p, ϕ_p are the polar and azimuthal angles of the polarization vector ($\theta_p = 0, \pi$ longitudinal and $\theta_p = \pi/2$ transverse polarization), and P measures the degree of polarization. The density matrix of a polarized lepton beam is [11]

$$\rho(l) = \frac{1}{2}(1 + \gamma_5 P_\mu \gamma^\mu). \tag{2.60}$$

The cross section now is calculated by taking the initial polarization and averaging over the final state polarizations. The leptonic tensor has an added term from the polarization:

$$L_{\mu\nu} = \frac{1}{4} Tr\{(l'_\sigma \gamma^\sigma + m)\gamma_\mu (l_\sigma \gamma^\sigma + m)(1 + \gamma_5 P_\sigma \gamma^\sigma)\gamma_\nu\} = L^s_{\mu\nu} + L^{as}_{\mu\nu} \tag{2.61}$$

where the polarization dependent term is

$$L^{as}_{\mu\nu} = im\epsilon_{\mu\nu\rho\sigma} q^\rho P^\sigma. \tag{2.62}$$

Following the same steps as in the previous section, evaluating $L^{as}_{\mu\nu}$ in the Breit system gives an antisymmetric matrix:

$$L^{as}_{\mu\nu} = imQ \begin{pmatrix} 0 & P_0 & -P_2 \\ & 0 & P_1 \\ & & 0 \end{pmatrix}, \tag{2.63}$$

and transforming into the helicity basis one obtains the hermitian matrix:

$$L^{as}_{\lambda\lambda'} = mQ \begin{pmatrix} P_0 & \frac{1}{\sqrt{2}}(P_1 + iP_2)e^{-i\Phi} & 0 \\ & 0 & \frac{1}{\sqrt{2}}(P_1 + iP_2)e^{-i\Phi} \\ & & -P_0 \end{pmatrix}. \tag{2.64}$$

The polarization vector initially defined in the lepton rest system must be Lorentz shifted into the Breit frame. The z-axis must also be rotated from pointing in the direction of lepton motion to the direction of $\vec{q}$ giving:

$$\begin{aligned} P^{Breit}_\mu = \; & P\{\sqrt{\frac{1-\epsilon}{1+\epsilon}}\cos\phi_p \sin\theta_p + \frac{Q}{2m}\sqrt{\frac{2\epsilon(1+\epsilon+2\delta)}{1-\epsilon^2}}\cos\theta_p, \\ & \sin\phi_p \sin\theta_p, \\ & \sqrt{\frac{2\epsilon}{1+\epsilon}}\cos\phi_p \sin\theta_p + \frac{Q}{2m}\sqrt{\frac{(1+\epsilon+2\delta)}{1+\epsilon^2}}\cos\theta_p, \\ & \frac{Q}{2m}\sqrt{\frac{1+\epsilon}{1-\epsilon}}\cos\theta_p\}. \end{aligned} \tag{2.65}$$

In the approximation $Q^2 \gg m^2$, the polarization vector simplifies to

$$P_\mu^{Breit} = \frac{Q}{2m} P \left(\sqrt{\frac{2\epsilon}{1-\epsilon}} \cos\theta_p,\ 0,\ \cos\theta_p,\ \sqrt{\frac{1-\epsilon}{1+\epsilon}} \cos\theta_p \right). \tag{2.66}$$

It is apparent that transversely polarized leptons give very small polarization effects in this approximation. Inserting the polarization vector into $L^{as}_{\lambda\lambda'}$ gives a hermitian matrix in the Breit frame:

$$L^{as}_{\lambda\lambda'} = \frac{Q^2}{2(1-\epsilon)} P \cos\theta_p \begin{pmatrix} \sqrt{1-\epsilon^2} & \sqrt{\epsilon(1+\epsilon)}e^{-i\Phi} & 0 \\ & 0 & \sqrt{\epsilon(1+\epsilon)}e^{-i\Phi} \\ & & -\sqrt{1-\epsilon^2} \end{pmatrix}. \tag{2.67}$$

2.3.5 Decomposition of the Density Matrix

The photon density matrix, normalized to unit flux of transverse photons is

$$\rho(\gamma)_{\lambda\lambda'} = \frac{1-\epsilon}{Q^2}\{L^s_{\lambda\lambda'} + L^{as}_{\lambda\lambda'}\}. \tag{2.68}$$

The two parts of the density matrix have opposite symmetry around the anti-diagonal:

$$L^s_{-\lambda-\lambda'} = (-1)^{\lambda-\lambda'} L^s_{\lambda\lambda'} \tag{2.69}$$

$$L^{as}_{-\lambda-\lambda'} = -(-1)^{\lambda-\lambda'} L^{as}_{\lambda\lambda'}. \tag{2.70}$$

As in the photon case, decomposing $\rho(\gamma)$ into an orthogonal set of hermitian matrices simplifies the calculations that follow:

$$\rho(\gamma) = \frac{1}{2}\sum_{\alpha=0}^{8} \Pi_\alpha \Sigma^\alpha; \tag{2.71}$$

$$\Sigma^0 = \begin{pmatrix} 1 & 0 & 0 \\ 0 & 0 & 0 \\ 0 & 0 & 1 \end{pmatrix}; \Sigma^1 = \begin{pmatrix} 0 & 0 & 1 \\ 0 & 0 & 0 \\ 1 & 0 & 0 \end{pmatrix}; \Sigma^2 = \begin{pmatrix} 0 & 0 & -i \\ 0 & 0 & 0 \\ i & 0 & 0 \end{pmatrix}; \tag{2.72}$$

$$\Sigma^3 = \begin{pmatrix} 1 & 0 & 0 \\ 0 & 0 & 0 \\ 0 & 0 & -1 \end{pmatrix}; \Sigma^4 = \begin{pmatrix} 0 & 0 & 0 \\ 0 & 2 & 0 \\ 0 & 0 & 0 \end{pmatrix}; \Sigma^5 = \frac{1}{\sqrt{2}} \begin{pmatrix} 0 & 1 & 0 \\ 1 & 0 & -1 \\ 0 & -1 & 0 \end{pmatrix};$$

$$\Sigma^6 = \frac{1}{\sqrt{2}} \begin{pmatrix} 0 & -i & 0 \\ i & 0 & i \\ 0 & -i & 0 \end{pmatrix}; \Sigma^7 = \frac{1}{\sqrt{2}} \begin{pmatrix} 0 & 1 & 0 \\ 1 & 0 & 1 \\ 0 & 1 & 0 \end{pmatrix}; \Sigma^8 = \frac{1}{\sqrt{2}} \begin{pmatrix} 0 & -i & 0 \\ i & 0 & -i \\ 0 & i & 0 \end{pmatrix}.$$

The Π_α vector then has the following components:

$$\begin{aligned} \Pi = \{ & 1, \quad -\epsilon\cos 2\Phi, \quad -\epsilon\sin 2\Phi, \quad \frac{2m}{Q}(1-\epsilon)P_0, \\ & \epsilon+\delta, \quad \sqrt{2\epsilon(1+\epsilon+2\delta)}\cos\Phi, \quad \sqrt{2\epsilon(1+\epsilon+2\delta)}\sin\Phi, \\ & \frac{2m}{Q}(1-\epsilon)(P_1\cos\Phi + P_2\sin\Phi), \quad \frac{2m}{Q}(1-\epsilon)(P_1\sin\Phi - P_2\cos\Phi)\}. \end{aligned} \tag{2.73}$$

The matrices zero to three, are similar to the ones used earlier, and describe transverse photons. Matrix four describes the longitudinal photons, and five to eight are the interference terms between the two. Note also that matrices 2,3,6,7 obey the symmetry in Eq. 2.69, and the remainder obey Eq. 2.70.

2.3.6 The Vector Meson Density Matrix

From the lepton vertex, we now turn to the hadron vertex, which describes the virtual process $\gamma N \to VN'$. γ will indicate a real photon, virtual photon or intermediate vector boson. The matrix element will be expressed in terms of the production amplitudes of Jacob and Wick [12]:

$$T_{\lambda_V \lambda_{N'} \lambda_\gamma \lambda_N} = \langle \lambda_V \lambda_{N'} | j_{\lambda_\gamma} | \lambda_N \rangle, \tag{2.74}$$

where the λ's are the helicities of the particles. This will give an explicit dependence of the cross section on the polarization angle Φ:

$$\frac{d\sigma_{\gamma N \to VN'}}{dt d\Phi} \propto \frac{1}{4}\sum |M|^2 = \frac{1}{2} Tr\{T\rho(\gamma)T^\dagger\}. \tag{2.75}$$

After integrating over Φ one gets:

$$\frac{d\sigma_{\gamma N\to VN'}}{dt}=\frac{d\sigma_T}{dt}+(\epsilon+\delta)\frac{d\sigma_L}{dt}=\frac{d\sigma_T}{dt}\{1+(\epsilon+\delta)R\}, \tag{2.76}$$

where R is the ratio of the two cross sections presented in Eq. 2.31. The vector meson density matrix can be found from the von-Neuman formula:

$$\tilde{\rho}(V)=\frac{1}{2}T\rho(\gamma)T^{\dagger}. \tag{2.77}$$

For convenience, we normalize the matrix with one averaged over Φ:

$$\rho(V)=\tilde{\rho}(V)/\int\frac{d\Phi}{2\pi}Tr\{\tilde{\rho}(V)\} \tag{2.78}$$

In analogy to the previous case, $\rho(V)$ can be decomposed according to the decomposition of $\rho(\gamma)$:

$$\rho(V)=\sum_{\alpha=0}^{8}\Pi_\alpha\rho^\alpha, \tag{2.79}$$

with

$$\rho(V)^\alpha_{ii'}=\frac{1}{2N_\alpha}\sum_{jj'nn'}T_{in'jn}\Sigma^\alpha_{jj'}T^*_{i'n'j'n}, \tag{2.80}$$

where n,n' denote the helicities of the nucleon system before and after the interaction, and i,j are the helicities of the vector meson and photon. N_α are the normalization constants:

$$\begin{aligned}
N_\alpha &= N_T=\frac{1}{2}\sum_{in'nj=\pm1}|T_{in'jn}|^2;\quad \alpha=0,1,2,3\\
N_\alpha &= N_L=\sum_{in'nj=0}|T_{in'jn}|^2;\quad \alpha=4\\
N_\alpha &= (N_TN_L)^{\frac{1}{2}};\quad \alpha=5,6,7,8.
\end{aligned} \tag{2.81}$$

Note that this normalization implies $Tr\rho^0=Tr\rho^4=1$. Photoproduction is a special case of the above decomposition, with the elements zero through four acting as Pauli matrices.

Since the ρ^α were normalized differently from one another, this changes the vector Π_α from the form given in Eq. 2.74 (the decomposition of $\rho(\gamma)$):

$$\begin{aligned}\Pi &= \frac{1}{1+\epsilon R}\{1, \ -\epsilon\cos 2\Phi, \ -\epsilon \sin 2\Phi, \ \frac{2m}{Q}(1-\epsilon)P_0, \\ &\epsilon R, \ \sqrt{2\epsilon R(1+\epsilon)}\cos\Phi, \ \sqrt{2\epsilon R(1+\epsilon)}\sin\Phi, \\ &\frac{2m}{Q}(1-\epsilon)\sqrt{R}(P_1\cos\Phi + P_2\sin\Phi), \ \frac{2m}{Q}(1-\epsilon)\sqrt{R}(P_1\sin\Phi - P_2\cos\Phi)\}.\end{aligned} \tag{2.82}$$

Parity conservation places a symmetry requirement on the production amplitudes:

$$T_{-i-n',-j-n} = (-1)^{(i-n')-(j-n)}T_{in',jn}. \tag{2.83}$$

Using this and the symmetry properties of the Σ_α presented earlier give the following symmetry relation for the density matrix, which reduces the number of independent elements:

$$\rho^\alpha_{ii'} = \pm(-1)^{i-i'}\rho^\alpha_{-i-i'} \ , \tag{2.84}$$

where the plus sign is for $\alpha = 0, 1, 4, 5, 8$, and the minus for $\alpha = 2, 3, 6, 7$. Using the above information, we can write the ρ^α in matrix form:

$$\begin{aligned}\rho^\alpha &= \begin{pmatrix} \rho^\alpha_{11} & Re\rho^\alpha_{10} + iIm\rho^\alpha_{1-1} & Re\rho^\alpha_{1-1} \\ & \rho^\alpha_{00} & -Re\rho^\alpha_{10} - iIm\rho^\alpha_{10} \\ & & \rho^\alpha_{11}\end{pmatrix} \quad \alpha = 0,1,4,5,8 \\ \rho^\alpha &= \begin{pmatrix} \rho^\alpha_{11} & Re\rho^\alpha_{10} + iIm\rho^\alpha_{1-1} & iIm\rho^\alpha_{1-1} \\ & 0 & Re\rho^\alpha_{10} + iIm\rho^\alpha_{10} \\ & & -\rho^\alpha_{11}\end{pmatrix} \quad \alpha = 2,3,6,7.\end{aligned} \tag{2.85}$$

The normalization condition $(Tr\{\rho^0\} = Tr\{\rho^4\} = 1)$ can be used to eliminate an extra term in ρ^0, ρ^4.

2.3.7 Vector Meson Decay

The angular distribution of the decay is expressed as

$$\frac{dN}{d\Omega} = W(\cos\theta,\phi) = \frac{3}{4\pi}\sum_{ii'} D^1_{i0}(\phi,\theta,-\phi)^*\rho(V)_{ii'}D^1_{i'0}(\phi,\theta,-\phi), \tag{2.86}$$

where the D's are the spin-one Wigner rotation functions defined as

$$\begin{aligned} D^1_{10} &= -\frac{1}{\sqrt{2}}\sin\theta e^{-i\phi} \\ D^1_{00} &= \cos\theta \\ D^1_{-10} &= \frac{1}{\sqrt{2}}\sin\theta e^{i\phi}. \end{aligned} \tag{2.87}$$

Using this to calculate the two-body decay of a vector meson such as the ρ_0 (with ρ^v expressing the density matrix elements of the vector meson), results in:

$$\begin{aligned} W(\cos\theta,\phi) &= \frac{3}{4\pi}\{\frac{1}{2}(\rho^v_{11}+\rho^v_{-1-1})\sin^2\theta + \rho^v_{00}\cos^2\theta \\ &+ \frac{\sin 2\theta}{\sqrt{2}}[(-Re\rho^v_{10}+Re\rho^v_{-10})\cos\phi + (Im\rho^v_{10}+Im\rho^v_{-10})\sin\phi] \\ &+ \sin^2\theta[-Re\rho^v_{1-1}\cos 2\phi + Im\rho^v_{1-1}\sin 2\phi\}. \end{aligned} \tag{2.88}$$

For a three-body decay of an axial vector, meson such as the a_1, the decay is more complicated, giving [13] (with ρ^a expressing the density matrix elements of the axial-vector meson)

$$\begin{aligned} W(\cos\theta,\phi) &= \frac{3}{8\pi}(\frac{1}{2}(\rho^a_{11}+\rho^a_{-1-1})(1+\cos^2\theta) + \rho^a_{00}\sin^2\theta \\ &+ \frac{\sin 2\theta}{\sqrt{2}}[(Re\rho^a_{10}-Re\rho^a_{-10})\cos\phi - (Im\rho^a_{10}+Im\rho^a_{-10})\sin\phi] \\ &+ \sin^2\theta[Re\rho^a_{1-1}\cos 2\phi - Im\rho^a_{1-1}\sin 2\phi\} \\ &+ \lambda\{(\rho_{11}-\rho_{1-1})\cos\theta \\ &+ \sqrt{2}\sin\theta[(Re\rho^a_{10}+Re\rho^a_{-10})\cos\phi - (Im\rho^a_{10}-Im\rho^a_{-10})\sin\phi]\}) \end{aligned} \tag{2.89}$$

where λ is a parameter related to the two possible couplings of the three particle decay. When two of the decaying particles are identical $\lambda = 0$ according to [13].

Substituting $\rho^\alpha(V)$ for $\rho(V)$ in Eq. 2.86 enables us to decompose the decay distribution:

$$W(\cos\theta,\phi) = \sum_{\alpha=0}^{8} \Pi_\alpha W^\alpha(\cos\theta,\phi). \tag{2.90}$$

giving

$$\begin{aligned}
W^\alpha &= \frac{3}{4\pi}\{\frac{1}{2}(1-\rho^\alpha_{00}) + \frac{1}{2}(3\rho^\alpha_{00}-1)\cos^2\theta \\
&- \sqrt{2}Re\rho^\alpha_{10}\sin 2\theta\cos\phi - \rho^\alpha_{1-1}\sin^2\theta\cos 2\phi\} \quad \alpha = 0,4 \\
W^\alpha &= \frac{3}{4\pi}\{\rho^\alpha_{11}\sin^2\theta + \rho^\alpha_{00}\cos^2\theta \\
&- \sqrt{2}Re\rho^\alpha_{10}\sin 2\theta\cos\phi - \rho^\alpha_{1-1}\sin^2\theta\cos 2\phi\} \quad \alpha = 0,1,4,5,8 \\
W^\alpha &= \frac{3}{4\pi}\{\sqrt{2}Im\rho^\alpha_{10}\sin 2\theta\sin\phi + Im\rho^\alpha_{1-1}\sin^2\theta\cos 2\phi\} \quad \alpha = 2,3,6,7,
\end{aligned} \tag{2.91}$$

where the trace condition was used in the first equation.

All the components are now available for the final answer. Substituting the polarization vector from Eq. 2.83 into Eq. 2.90 derived above, gives the final answer. For example, the photoproduction case gives

$$\begin{aligned}
&W(\cos\theta,\phi,\Phi) = W^0 - P_\gamma\cos 2\Phi W^1 - P_\gamma \sin 2\Phi W^2 \\
&= \frac{3}{4\pi}\{\frac{1}{2}(1-\rho^0_{00}) + \frac{1}{2}(3\rho^0_{00}-1)\cos^2\theta \\
&\quad -\sqrt{2}Re\rho^0_{10}\sin 2\theta\cos\phi - \rho^0_{1-1}\sin^2\theta\cos 2\phi \\
&\quad -P_\gamma\cos 2\Phi[\rho^1_{11}\sin^2\theta + \rho^1_{00}\cos^2\theta \\
&\qquad -\sqrt{2}Re\rho^1_{10}\sin 2\theta\cos\phi - \rho^1_{1-1}\sin^2\theta\cos 2\phi] \\
&\quad -P_\gamma\sin 2\Phi[\sqrt{2}Im\rho^2_{10}\sin 2\theta\sin\phi + Im\rho^2_{1-1}\sin^2\theta\sin 2\phi]\}.
\end{aligned} \tag{2.92}$$

2.3.8 Natural Parity and SCHC

The production amplitude T has an additional symmetry that enables separation of the contributions from natural ($P = (-1)^J$) and unnatural ($P = -(-1)^J$) parity exchange in the t-channel (top sign for natural parity):

$$T_{-in',-jn} = \pm(-1)^{i-j}T_{in',jn} = \mp(-1)^i T_{in',jn}, \tag{2.93}$$

using this, one can separate the two and write $T = T^N + T^U$ where

$$T^{(N,U)}_{in',jn} = \frac{1}{2}\{T_{in',jn} \pm (-1)^{i-j} T_{-in,-jn'}\} \tag{2.94}$$

We next define natural and unnatural density matrices:

$$\rho^{\alpha(N,U)}_{ii'} = \frac{1}{2N_\alpha} \sum_{jj'nn'} T^{(N,U)}_{in'jn} \Sigma^{\alpha}_{jj'} T^{*(N,U)}_{i'n'j'n}, \tag{2.95}$$

The main point of this separation is that it enables us to write: $\rho^\alpha = \rho^{\alpha(N)} + \rho^{\alpha(U)}$, that is, the cross terms vanish for unpolarized nucleons [11]. This allows us to express $\rho^{\alpha(N,U)}$ as

$$\rho^{\alpha(N,U)}_{\lambda\lambda'} = \frac{1}{2}[\rho^{\alpha}_{\lambda\lambda'} \pm d_\alpha (-1)^{\lambda'} \rho^{\beta}_{\lambda-\lambda'}], \tag{2.96}$$

where $\alpha,\ \beta,\ d_\alpha$ are

$$\begin{aligned} \alpha &= (\ 0,\ 1,\ 2,\ 3,\ 4,\ 5,\ 6,\ 7,\ 8\ ), \\ \beta &= (\ 1,\ 0,\ 3,\ 2,\ 4,\ 5,\ 7,\ 6,\ 8\ ), \\ d_\alpha &= (\ -1,\ -1,\ i,\ -i,\ 1,\ 1,\ i,\ -i,\ 1\ ). \end{aligned} \tag{2.97}$$

S-channel helicity conservation (SCHC) suggests that the helicities are conserved in the hadronic center of mass. This means that when the photon converts to a vector meson it passes on its helicity. Quantitativly

$$T_{in',jn} = T_{in',jn}\delta_{n'n}\delta_{ij} \tag{2.98}$$

Under this assumption, only three independent amplitudes remain. Assuming also natural parity exchange, leaves only two independent terms which reference [11] picks to be $T_{1\frac{1}{2}1\frac{1}{2}}$, $T_{0\frac{1}{2}0\frac{1}{2}}$, and define their relative phase to be δ. The vector meson density matrices presented earlier (Eq. 2.85) simplify considerably:

$$\rho^0 = \frac{1}{2}\begin{pmatrix} 1 & 0 & 0 \\ 0 & 0 & 0 \\ 0 & 0 & 1 \end{pmatrix}; \quad \rho^1 = \frac{1}{2}\begin{pmatrix} 0 & 0 & 1 \\ 0 & 0 & 0 \\ 1 & 0 & 0 \end{pmatrix}; \quad \rho^2 = \frac{1}{2}\begin{pmatrix} 0 & 0 & -i \\ 0 & 0 & 0 \\ i & 0 & 0 \end{pmatrix} \tag{2.99}$$

$$\rho^3 = \frac{1}{2}\begin{pmatrix} 1 & 0 & 0 \\ 0 & 0 & 0 \\ 0 & 0 & -1 \end{pmatrix}; \quad \rho^4 = \begin{pmatrix} 0 & 0 & 0 \\ 0 & 1 & 0 \\ 0 & 0 & 0 \end{pmatrix}; \tag{2.100}$$

$$\rho^5 = \frac{1}{\sqrt{8}}\begin{pmatrix} 0 & e^{i\delta} & 0 \\ e^{-i\delta} & 0 & -e^{-i\delta} \\ 0 & -e^{i\delta} & 0 \end{pmatrix}; \quad \rho^6 = \frac{1}{\sqrt{8}}\begin{pmatrix} 0 & -ie^{i\delta} & 0 \\ ie^{-i\delta} & 0 & ie^{-i\delta} \\ 0 & -ie^{i\delta} & 0 \end{pmatrix} \tag{2.101}$$

$$\rho^7 = \frac{1}{\sqrt{8}}\begin{pmatrix} 0 & e^{i\delta} & 0 \\ e^{-i\delta} & 0 & e^{-i\delta} \\ 0 & e^{i\delta} & 0 \end{pmatrix}; \quad \rho^8 = \frac{1}{\sqrt{8}}\begin{pmatrix} 0 & -ie^{i\delta} & 0 \\ ie^{-i\delta} & 0 & -ie^{-i\delta} \\ 0 & ie^{i\delta} & 0 \end{pmatrix}. \tag{2.102}$$

In photoproduction, we are left with only two non-zero matrix elements in the decay distribution:

$$\rho^1_{1-1} = \frac{1}{2}, \quad Im\rho^2_{1-1} = -\frac{1}{2}, \tag{2.103}$$

and a simplified angular distribution:

$$W(\cos\theta, \psi) = \frac{3}{8\pi}\sin^2\theta(1 + P_\gamma \cos 2\psi), \tag{2.104}$$

where $\psi = \phi - \Phi$ is a measure of the rotation of the polarization vector of the meson from the polarization of the photon that created it. This prediction is tested experimentally in the Appendix.

In longitudinally polarized vector meson production, leptoproduction, and neutrino production, the decay angular distribution is given by

$$W(\cos\theta, \psi) = \frac{1}{1 + \epsilon R}\frac{3}{8\pi}\{2\epsilon R\cos^2\theta + \sin^2\theta(1 + \epsilon\cos 2\psi) \tag{2.105}$$

$$- \sqrt{2\epsilon R(1+\epsilon)}\cos\delta\sin 2\theta\cos\psi \tag{2.106}$$

$$+ \sqrt{2\epsilon R(1-\epsilon)}\sin\delta\sin 2\theta\sin\psi\}. \tag{2.107}$$

Under an assumption made later in Ch. 6, $R \simeq 0$, and since $\epsilon \simeq 1$ in our sample, we get a distribution similar to photoproduction:

$$W(\cos\theta,\psi) = \frac{3}{8\pi}\sin^2\theta(1+\epsilon\cos 2\psi). \tag{2.108}$$

For the decay of an axial vector meson produced by neutrino interactions, the angular distribution is given by

$$\begin{aligned} W(\cos\theta,\psi) \quad = \quad & \frac{1}{1+\epsilon R}\frac{3}{8\pi}\{2-\sin^2\theta(1+\epsilon\cos 2\psi)+2\epsilon R\sin^2\theta \\ & -\sqrt{2\epsilon(1-\epsilon)R}\sin\delta\sin 2\theta\sin\psi \\ & +\sqrt{2\epsilon(1+\epsilon)R}\cos\delta\sin 2\theta\cos\psi\} \end{aligned} \tag{2.109}$$

Using the same values as before for R and ϵ, we obtain a different angular distribution:

$$W(\cos\theta,\psi) = \frac{3}{8\pi}[2-\sin^2\theta(1+\epsilon\cos 2\psi)]. \tag{2.110}$$

CHAPTER 3

THE EXPERIMENT

The E745 experiment was run from April, to August, 1985 and yielded approximately 200,000 frames of normal pictures, 64,000 frames of holographic pictures, and $\sim$ 100 magnetic tapes with the electronic data from the down stream detectors. Our final sample of neutrino candidate events consisted of 5959 events (8902 with the additional data from the 1988 run). The target for the neutrino beam and the main detector in the experiment was the Tohoku 1-meter bubble chamber. Scintillators surrounded the bubble chamber for use in the event trigger. Down stream of the bubble chamber, an array of drift chambers, Optical Spark Chambers, Limited Streamer Chambers, The dE/dx detector CRISIS, and a muon detector were arranged to provide identification, and improve the momentum measurement of the muon. The general layout of the experiment is presented in Fig. 3.1. The following sections describe the different portions of the experimental hardware and the preliminary steps of data processing.

3.1 The Neutrino Beam

The Fermilab neutrino beam line was used to produce the wide band neutrino beam used in this experiment. The main ring protons of 800 GeV were directed to a Beryllium Oxide target of roughly one interaction length ($4.5cm$). The accelerator delivered three pings (pulses) of protons at the end of each one minute cycle during the flattop period (the last portion of the accelerator cycle when the magnet currents are maximum and constant). The pings of $2msec$ width were separated by 10 seconds from one another, and each contained about 1.5×10^{12} protons.

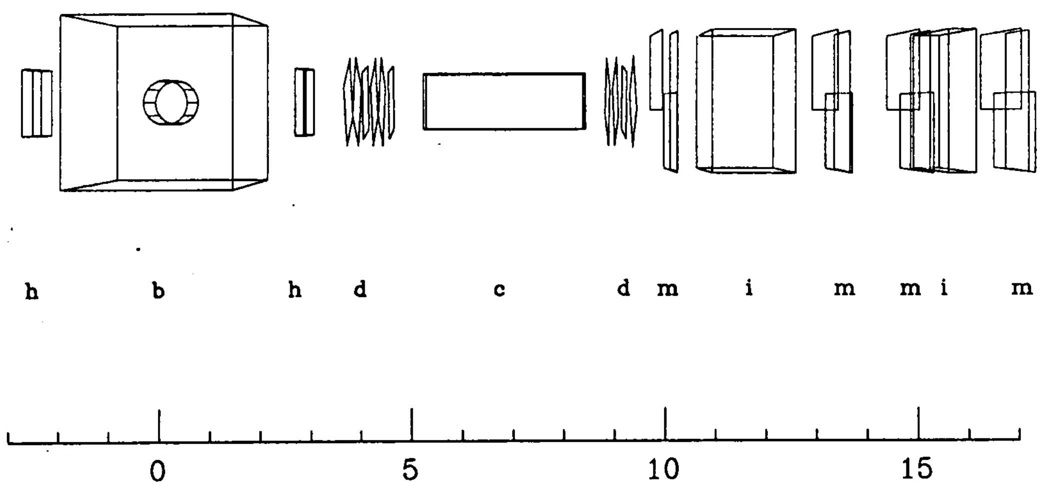

Figure 3.1: The E745 detector system. Scale is in meters. (b)bubble chamber; (h)hodoscope; (d)drift chamber; (c)crisis; (m)muon detector; (i)iron.

The secondary particles generated, entered the quadrupole triplet magnet system, which was set to preferentially select K^+ particles of 300 to 400 GeV. The selection in a wide band beam, however, is not overly restrictive, so that a high beam flux, consisting mostly of $K's$ and $\pi's$ of both charges, pass on through the system. The secondary particles then traverse a 500 meter decay pipe, where the neutrinos are produced through the following decay modes:

$$\begin{aligned} K^+ &\rightarrow \mu^+\nu_\mu \\ K^- &\rightarrow \mu^-\overline{\nu}_\mu \\ \pi^+ &\rightarrow \mu^+\nu_\mu \\ \pi^- &\rightarrow \mu^-\overline{\nu}_\mu \end{aligned}$$

To extract the neutrinos from the background, the beam is next passed through a kilometer of earth called the "berm", where muons and hadrons are absorbed without appreciably affecting the neutrino flux. On the average, two to three muons reach the bubble chamber in each beam pulse.

3.2 Trigger and Data Acquisition

Timing signals from the accelerator indicated the arrival of a ping, and were used to expand the bubble chamber and take a normal picture on every cycle. This was done in order to get the maximum amount of information in case of a bad trigger, and to check the efficiency of the trigger. A different trigger constructed from the accelerator signal, and a combination of the scintillator hodoscopes around the bubble chamber started the data aquisition on all other components of the experiment.

The main scintillator hodoscopes, which formed the trigger signal were split into four groups. The two smaller sets wrapped directly around the bubble chamber in the up and down stream positions. The other two, of larger area, consisted of 24 scintillator paddles, 120 by 10cm each, arranged in x and y planes [15]. These were placed up and down stream of the magnet yoke to give a more efficient directional veto. Other units were placed above and below the bubble chamber to veto cosmic ray background.

For a normal neutrino trigger, the hodoscope signal consisted of no signal in the upstream hodoscopes (the neutrino is neutral and is not detected), and a simultaneous signal in the downstream hodoscope (indicating some interaction and the passage of charged particles out of the bubble chamber). Between spills, a muon trigger (indicated by a simultaneous signal in both up and down stream hodoscopes) was generated and proved very useful in testing and surveying the counter system.

The main trigger [15], after differing amounts of delay, supplied the timing for the holographic flash and the begining of the data acquisition process. The trigger set the common stop signal on the CAMAC and FASTBUS TDC's (Time to Digital Converters), which read the drift chamber and muon detector data. After a slightly longer delay, the data acquisition software MULTI transferred the data to magnetic tape on a PDP-11 computer.

3.3 The Bubble Chamber

3.3.1 Bubble Chamber Hardware

The bubble chamber body is a cylinder of length $107cm$ and radius $41.5cm$, with two glass windows each of thickness $28cm$ at both ends of the cylinder, and an expansion system connected to its upper part. A 575 liter mixture of Freon R115 (C_2ClF_5)74% by weight and Freon R116 (C_2F_6)26% by weight filled the bubble chamber. The freon was maintained at a pressure of 20 Bar and a temperature of $\sim 26°C$. The expansion system consisted of a hydraulic piston that transmitted its motion via oil to the freon through a membrane of polyurethane. The superheated state of the fluid at minimum pressure of 8 Bar lasts for approximately 10 msec, covers the duration of the spill, and enables the fluid to start boiling and form bubbles. A superconducting magnet surrounding the bubble chamber body provided a magnetic field of 29 kilogauss for particle momentum measurement. A summary of the bubble chamber properties is presented in Table 3.1 [16].

Pictures were taken of events in the bubble chamber by three conventional stereo cameras and one holographic camera. The normal picture was taken after a delay of 2 to 3 msec, which ideally should give a track width of 200-500 μm. The actual track width varied between 500 to 1000 μm [17]. The purpose of the holographic system was to obtain a higher magnification of the interaction vertex. Since holography can provide high magnification over a large depth of field, it is ideally suited for a neutrino experiment where the beam is spread over a large volume. For the holographic system, an Nd-Yag 532nm laser beam pulse was split into one beam that passed through the bubble chamber, and a second reference beam that combined with the first on film to form an interference pattern. Another requirement to achieve high resolution in the bubble chamber is to take the picture early when the bubbles are small. The holographic picture was taken between 50 to 200 μsec after the main trigger. This ideally should give a track width of 50μm, but the actual track width varied between 100 and 300 μm. The holography during the run was inefficient because of problems with laser stability, turbulence, and polarization shifts, and was not used in this work.

3.3.2 Bubble Chamber Film

Each completed roll of film was developed in Lab F and scanned to help in improving operating conditions and correcting problems with the bubble chamber.

Table 3.1: Parameters of the Tohoku 1m bubble chamber

Parameter	Value
Expansion system	One hydraulic piston
Membrane	Polyurethane, $67 cm dia.$
Expansion Rate	One per 3 seconds
Diameter	83 cm
Length	107 cm
Visible Volume	$\sim 575 l$
Freon Mixture	R115 (C_2ClF_5)74% weight
	R116 (C_2F_6)26% weight
Density	$\sim 1.15 g/cm^3$
Index of Refraction	1.18
Radiation Length	$\sim 27 cm$
Interaction Length	$\sim 57 cm$
Visible Mass	$\sim 660 kg$
Temperature	$25 - 30°C$
Pressure	$20 \rightarrow 8 Bar$
Normal Cameras	3 views, $35 mm$ film
Holographic Camera	1 view, $70 mm$ film
Laser	Nd-Yag, $250 mJ, 532 nm$

A small amount of data estimated at 5.9% [18] was lost at this stage because of testing, mistiming of the trigger, and problems in film development. The film was then distributed to the three scanning and measuring centers at Tohoku University, University of Tennessee, and a joint center of Brown University, Fermilab and MIT. Tohoku University did the major part of the scanning and measuring by taking over two thirds of the film. Each roll was scanned two or more times, and the scanning efficiency was estimated to be 99.9% [17].

An event was considered a neutrino event if there was no incoming charged track, and at least two outgoing charged tracks. Among the leaving tracks, at least one had to have a momentum of 1 GeV/c or more, to eliminate background from low energy neutral hadrons. Another requirement was that no minimum ionizing particles be detected in the backward direction, in order to eliminate background from cosmic rays and charged particle interactions [15].

Every scanned event was measured at least twice. The first measurement concentrated on the tracks from the primary vertex. In the second pass, secondaries and tertiaries, such as neutral decays, e^+e^- pairs, neutral, and charged interactions were measured. Three photographs are taken of each event from different positions in space. Special calibration points are scratched on the bubble chamber glass (fiducial points), which help situate the track in three dimensions inside the bubble chamber. The measuring machine operators recored the position of roughly 10 points per track, and the position of the fiducial points in all three views.

Use of a heavy liquid, with short radiation length, caused measuring losses for some events due to a high multiplicity of secondary interactions and e^+e^- pairs that obscured the primary event. Additional losses were caused by poor bubble chamber operating conditions, which occasionally resulted in turbulence. The measurement efficiency was estimated at 90.8% [17].

3.3.3 Film Measurement Reconstruction

The measured data is run through a first processing stage program called PANAL, and the events are then reconstructed using the program TVGP (Three View Geometry Program) [19] modified for E745. The modifications to TVGP include the measuring machine error, bubble chamber optical parameters, liquid properties, and the magnetic field map.

TVGP starts the fitting procedure by creating circle fits for each view separately in two dimensions. In the next step, the views are combined two at a time, to create three circles in space. The final step combines three points from each of the three circles to create a more accurate curvature estimate. The momentum is finally calculated from knowledge of the curvature and the magnetic field in the bubble chamber. The momentum for stopping tracks is calculated using a range momentum table which gives more accurate results than curvature fitting.

The final step of linking the main vertex events with their secondary interactions is done by the program TPMVR (TVGP Multivertex Reconstruction), and the output is written in the form of a Data Summary Tape. Most of this work was done at Tohoku University, which provided a copy of the Data Summary Tape to all of the groups.

3.4 The Downstream System

3.4.1 The Drift Chambers

The purpose of the drift chambers was to track the particles immediately after their exit from the bubble chamber, especially the muon track. The drift chamber system consisted of ten independent planes, each consisting of 24 parallel cells or channels. A stiff aluminum frame, which pressed several layers of G-10 plastic together, held the cell wires at the correct tension. A thin sheet of grounded mylar around the cells, allowed most particles to get through, and sealed the gas in the drift chambers. Six of the planes organized in two triplets, followed the bubble chamber, the other four organized in a triplet, and a spare were placed farther downstream after the CRISIS detector.

Each cell had a central $20\mu m$ sense wire, which carried a high positive voltage of about $1200V$ to collect the drifting electrons. Around the perimeter of the cell were sixteen $100\mu m$, wires which carried a high negative voltage to shape the electric field in the cell and make it as uniform as possible (see Fig. 3.2(a)). The gas composition was 1% Methane, 9% Carbon-Dioxide, and 90% Argon which gave a drift velocity of around $4.8cm/\mu sec$.

Each cell was 2 inches wide, to provide a drift distance of an inch on each side. The hardware, which was unable to distinguish from which side the signal drifted into the wire, gave a real, as well as a ghost, signal. The chambers were square, each covering an area of approximately 122 by 122 cm. Within a triplet, the chambers were set with an angle of 120° between one another with the first drift chamber set with its wires parallel to the y-axis. The spatial resolution achieved with the drift chambers was $180\mu m$. The determination of the drift chamber parameters is described in Chapter 4.

3.4.2 Muon Detector

The muon detector was a large drift chamber system, with thick slabs of iron placed between its planes, to stop all hadrons and only allow the muon to pass. The muon detector consisted of 12 planes organized in four groups of three. The first plane of each triplet gave a direction measurement in the y-axis, and the other two in the z-axis. The redundancy in the z-axis measurement was intended for a different experiment, with a high expected background of muons coming into the lab from above and below the bubble chamber. The double construction would

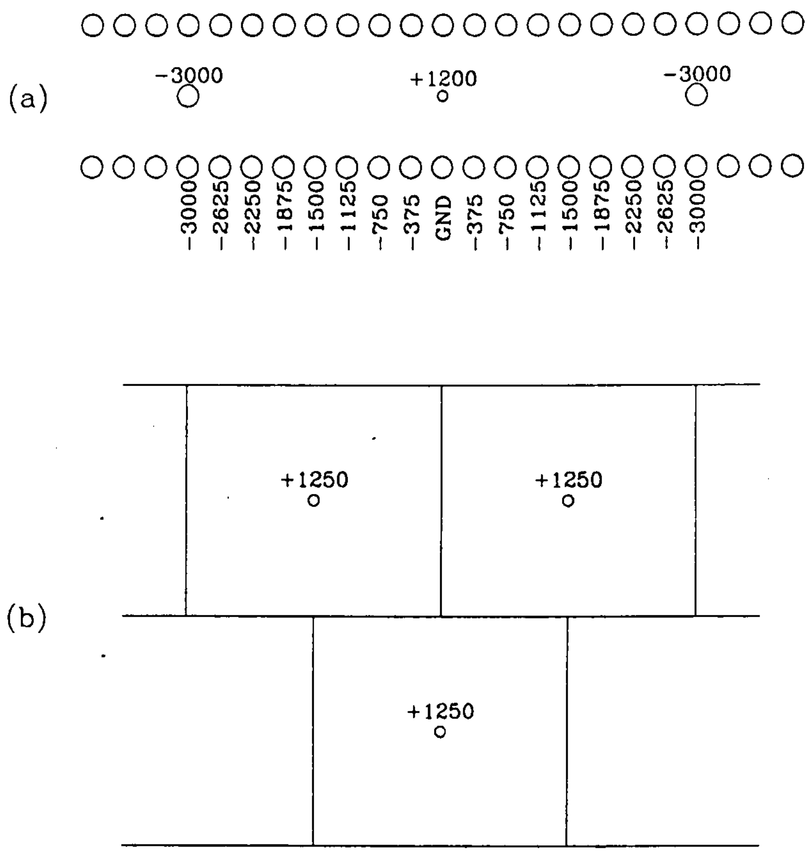

Figure 3.2: (a) A single drift chamber cell. (b) Three cells from the muon detector.

enable an adjustment of the detector to minimize background and maximize the signal. Each plane was made from 13 individual modules, each having 15 cells, for a total of 195 channels per plane. The first triplet placed before the first iron absorber gave a spatial resolution of $200\mu m$, almost as accurate as the drift chambers in front of it. The next two were between the two absorbers, and the fourth was located behind the last absorber. The triplets behind the iron gave poorer track resolution because of the multiple Coulomb scattering in the metal.

Each cell was made of a stiff tube of aluminum, square in cross section, with a sense wire running down the middle. The muon detector did not have the ghost hit problem of the drift chambers, because of its special construction (see Fig. 3.2(b)). Each plane was built as a double plane of cells, with the back plane shifted by half a cell with respect to the front plane. The cell width was an inch, so that each plane covered roughly an area of 249 by 125 cm. The gas used was a 10% Methane and 90% Argon mixture, with a drift velocity of about $3.0cm/\mu sec$. The muon detector parameters were also determined accurately, using the same surveying procedure used on the drift chambers. The drift chambers and muon detectors together, defined the downstream coordinate system.

3.4.3 Electronic Data Aquisition

The on-line system used during the run, was the MULTI shell program provided by Fermilab [20] running on a PDP-11, with the RT-11 operating system. The program was modified to read the special detectors of E745 and to display histograms during the run itself, to allow constant monitoring of the equipment. Each tape, after being filled, was copied with the original, going to the Lab archives. A more extensive checking program was run from each new tape to discover any problems which may have been missed by the on-line system. Copies of all the tapes were distributed to all participants in the experiment for eventual incorporation with the bubble chamber data in the process called hybridization. Hybridization was used to help identify and improve the momentum measurement on the muon. This process will be covered in detail in the next chapter.

CHAPTER 4

DATA HYBRIDIZATION

Data Hybridization is the process of matching and fitting the tracks from the bubble chamber to the data collected downstream in the drift chamber and muon detector. This chapter will cover the steps involved in this process which are:

1. Find a single track, given an initial survey of the drift chamber coordinates and given a few hits in the chambers.

2. Find the precise location of the drift chambers, using the above particle tracks. This step is important since the drift chambers can only be placed along the beam line in an approximate manner. Steps 1 and 2 are iterated until the drift chamber coordinates converge to their optimum values, according to a χ^2 fit.

3. Disentangle tracks from actual events with multiple hits and ghost hits.

4. Align the drift chamber coordinate system with the bubble chamber coordinate system. This is done using tracks measured in the bubble chamber to find the rotation and translation parameters.

5. Connect tracks measured in the two systems to optimize the momentum and angle measurements.

4.1 Line Fitting

The first step in fitting a track is to define a drift chamber coordinate system:

1. The origin is set in the middle of the first drift chamber plane.
2. The x-axis points in the beam direction downstream.
3. The y-axis points vertically downward.
4. The z-axis forms a right handed system and points toward the bubble chamber cameras.

Each drift chamber plane measures distance in a direction perpendicular to its wires. We define a ρ axis for each plane along its direction of measurement. This axis originates from the point where the x-axis passes through the plane. The geometrical parameters used in the drift chamber calculations are:

1. ρ_0 is the distance of the center of the drift chamber from the x-axis along the ρ axis.
2. θ is the angle at which the ρ axis was placed relative to the y-axis of the experiment.
3. x is the position of the drift chamber along the x-axis.
4. v is the drift velocity of the electrons in the drift chamber gas.
5. t_0 is the zero time point for the electronic time measuring system.
6. w_{ch} is the width of a drift cell.

Fitting a track means finding its line equation in the drift chamber coordinate system in the form:

$$\begin{aligned} y &= a_y x + b_y \\ z &= a_z x + b_z \ , \end{aligned} \tag{4.1}$$

where the line equation parameters needed are: y-slope (a_y), y-intercept (b_y), z-slope (a_z), and z-intercept (b_z). Given these, the distance along the ρ axis of each chamber can be calculated:

$$\begin{aligned}
\rho_{fit} &= y\cos\theta + z\sin\theta \\
&= (a_y x + b_y)\cos\theta + (a_z x + b_z)\sin\theta \\
&= (a_y\cos\theta + a_z\sin\theta)x + (b_y\cos\theta + b_z\sin\theta) \\
&= a_\rho x + b_\rho.
\end{aligned} \tag{4.2}$$

The ρ for each chamber can be calculated independently from the experimental hits registered in that drift chamber. The information given from each hit is the channel number (n_{ch}), and the drift time (t). Together with the drift chamber parameters, this gives for ρ:

$$\begin{aligned}
\rho_{hit} &= \rho_0 + \rho_{channel} \pm \rho_{drift} \\
&= \rho_0 + n_{ch}w_{ch} \pm v(t - t_0),
\end{aligned} \tag{4.3}$$

where $\rho_{channel}$ is the rough distance equal to the channel number, times the channel width, and ρ_{drift} is the drift distance equal to the drift velocity, times drift time. The $\pm$ indicates the uncertainty in the direction from which the hit drifted to the wire (the ghost hit). Both methods of finding ρ are independent of one another and use different parameters. By minimizing the differences between these sets of $\rho's$ for all chambers, we can find the best fit parameters for a given line. The following equations show the χ^2 method for finding a_y, b_y, a_z and b_z. The sum here is over all points that belong to a single line, or equivalently over all drift chambers with a hit in them. The χ^2 sum is:

$$\chi^2 = \frac{1}{\sigma_\rho^2}\sum_{i=1}^{n}(\rho_i^{hit} - \rho_i^{fit})^2, \tag{4.4}$$

where σ_ρ, the error in ρ is assumed the same for all chambers, and drops out of the calculation. Differentiating χ^2 with respect to a_y, b_y, a_z and b_z, and setting the derivatives to zero, gives four equations with four unknowns. In symmetric matrix notation:

$$\sum_{i=1}^{n}\begin{pmatrix}\rho_i^h x_i\cos\theta_i\\ \rho_i^h\cos\theta_i\\ \rho_i^h x_i\sin\theta_i\\ \rho_i^h\sin\theta_i\end{pmatrix} = \tag{4.5}$$

$$\underbrace{\sum_{i=1}^{n}\begin{pmatrix}x_i^2\cos^2\theta_i & x_i\cos^2\theta_i & x_i^2\cos\theta_i\sin\theta_i & x_i\cos\theta_i\sin\theta_i\\ & \cos^2\theta_i & x_i\cos\theta_i\sin\theta_i & \sin\theta_i\cos\theta_i\\ & & x_i^2\sin^2\theta_i & x_i\sin^2\theta_i\\ & & & \sin^2\theta_i\end{pmatrix}}_{=M}\begin{pmatrix}a_y\\ b_y\\ a_z\\ b_z\end{pmatrix}.$$

Solving this equation with the standard linear algebra technique of gaussian elimination, gives the required line parameters. To find the errors in the line parameters, one first determines the error in ρ:

$$\sigma_\rho^2 = \frac{1}{n-4}\sum_{i=1}^{n}(\rho_i^h it - \rho_i^f it)^2. \tag{4.6}$$

From this, the errors in the line parameters follows; for example the error in a_y:

$$\sigma_{a_y}^2 = \sigma_\rho^2\sum_{i=1}^{n}\left(\frac{\partial a_y}{\partial \rho_i}\right)^2. \tag{4.7}$$

To find $\partial a_y/\partial\rho_i$, one can differentiate the above matrix equation with respect to each ρ_i (the main matrix designated by M is independent of ρ_i and will not change):

$$\begin{pmatrix}x_i\cos\theta_i\\ \cos\theta_i\\ x_i\sin\theta_i\\ \sin\theta_i\end{pmatrix} = M\begin{pmatrix}\partial a_y/\partial\rho_i\\ \partial b_y/\partial\rho_i\\ \partial a_z/\partial\rho_i\\ \partial b_z/\partial\rho_i\end{pmatrix}. \tag{4.8}$$

Solving the error equation takes very little extra computer time, since M must be diagonalized in the solution to Eq. 4.5.

4.2 Surveying

To find tracks in the drift chambers, accurate values for the geometrical parameters mentioned above are necessary. The initial determination of most of these quantities was approximated using tape measure, theodolite, and estimates about the gas and electronics. Estimates were readily available for all parameters except ρ_0. The initial step, therefore, was to get a first approximation for ρ_0. This was done by looking at a very special type of events — muon events, with only a single muon track that passed through all chambers.

To define our coordinate system, an assumption was made that four of the chambers have $\rho_0 = 0$. Four was chosen since that is the minimum number of hits needed to define a track. To give a long lever arm for the line calculations, the four drift chambers chosen were numbers 1, 2, 7 and 8. For each track, the track parameters were determined using only the four calibration chambers for which the ρ_0 is known by definition. In an ideal experiment with no errors, the difference $\rho_0 = \rho_{hit} - \rho_{fit}$ of the other chambers would give a single value - the shift of the drift chamber from the x-axis. For a real experiment, we expect a gaussian- like distribution centered at the desired ρ_0. The observed distribution, for the muon detector, followed this closely, since it does not have the problem of ghost hits. The plots for the drift chamber showed a larger background, but the peaks for the real ρ_0 were clearly discernable. The estimated amount of signal to background was 1 to 32, since the four coordinate chambers each have a ghost hit giving 16 possible lines, only one of which is correct, and the tested chamber itself has a ghost hit for another factor of two.

After getting a first estimate for all the needed quantities, it is possible to determine the drift chamber parameters more accurately. Using single muon events, as before, it is possible to form a fit of the difference between the ρ_{hit} and the ρ_{fit}. Solving the χ^2 equation, a correction to the drift chamber parameters is obtained. The calculation is then repeated in an iterative fashion until the parameter values converge. To linearize the equations we assume that the changes in each step are small and insert only changes in the fitted quantities. It is convenient to use a slightly different set of parameters for the iteration:

$$\rho_{hit} = \rho_c + \rho_\pm \pm tv \tag{4.9}$$

$$\rho_\pm = \rho_0 \mp t_0 v, \tag{4.10}$$

where ρ_c is short for $\rho_{channel} = n_{ch} w_{ch}$, from before. Since ρ_{fit} includes trigonometric functions, it was linearized in the following manner:

$$\rho'_{fit} = \rho_f + (\frac{\partial \rho_f}{\partial \theta})d\theta + (\frac{\partial \rho_f}{\partial x})dx \tag{4.11}$$

$$\rho_\theta = \frac{\partial \rho_f}{\partial \theta} = z\cos\theta - y\sin\theta \tag{4.12}$$

$$\rho_x = \frac{\partial \rho_f}{\partial x} = a_y\cos\theta + a_z\sin\theta, \tag{4.13}$$

where ρ_f is the old value for ρ_{fit}, and ρ'_{fit} is the new value. The sum must be done separately over the plus and minus drift times, since the formula is slightly different for the two cases. Forming the χ^2, one gets:

$$\begin{aligned}\chi^2 &= \frac{1}{\sigma_\rho^2}\sum_\pm(\rho'_{fit} - \rho'_{hit})^2 \\ &= \frac{1}{\sigma_\rho^2}[\sum_+(\rho_f + \rho_\theta\Delta\theta + \rho_x\Delta x - \rho_c - \rho_+ - tv)^2 \\ &\quad + \sum_-(\rho_f + \rho_\theta\Delta\theta + \rho_x\Delta x - \rho_c - \rho_- + tv)^2],\end{aligned} \tag{4.14}$$

where the plus sign indicates a sum over all tracks with a positive drift distance, and the minus sign indicates a negative drift distance. Differentiating χ^2 with respect to the new parameters $\rho_+, \rho_-, v, \theta$ and x, and setting them equal to zero, gives us a matrix equation for the improved drift chamber coordinates:

$$\begin{pmatrix} \sum_+(\rho_c - \rho_f) \\ \sum_-(\rho_c - \rho_f) \\ \sum_\pm(\rho_c - \rho_f)(\mp t) \\ \sum_\pm(\rho_c - \rho_f)\rho_\theta \\ \sum_\pm(\rho_c - \rho_f)\rho_x \end{pmatrix} = \tag{4.15}$$

$$\begin{pmatrix} \sum_+(-1) & 0 & \sum_+(-t) & \sum_+\rho_\theta & \sum_+\rho_x \\ & \sum_-(-1) & \sum_- t & \sum_-\rho_\theta & \sum_-\rho_x \\ & & \sum_\pm t^2 & \sum_\pm \mp t\rho_\theta & \sum_\pm \mp t\rho_x \\ & & & \sum_\pm \rho_\theta^2 & \sum_\pm \rho_\theta\rho_x \\ & & & & \sum_\pm \rho_x^2 \end{pmatrix} \begin{pmatrix} \rho_+ \\ \rho_- \\ v \\ \Delta\theta \\ \Delta x \end{pmatrix}.$$

The errors are calculated in the same way as was done in the last section, starting with the error on ρ:

$$\sigma_\rho^2 = \frac{1}{n-5}\sum_\pm(\rho_{hit} - \rho_{fit})^2. \tag{4.16}$$

The error on v for example is

$$\sigma_v^2 = \sum_\pm \sigma_\rho^2 \left(\frac{\partial v}{\partial(\rho_c - \rho_f)}\right)^2. \tag{4.17}$$

The partial derivatives are determined as before by taking the derivative of the above matrix equation.

The spatial resolution obtained by this procedure was about $180\mu m$ (see Fig. 4.1), which is less than a factor of two from the minimum possible count on our TDC of $100\mu m$. The resolution of the muon detector planes placed before the iron absorber was almost as good. The resolution was poorer for the planes placed behind the absorber (see Fig. 4.2). This procedure is sufficiently accurate to observe the shifts that occurred in the drift chambers during the run. From examination of the log book, it is possible to correlate big shifts with major repairs

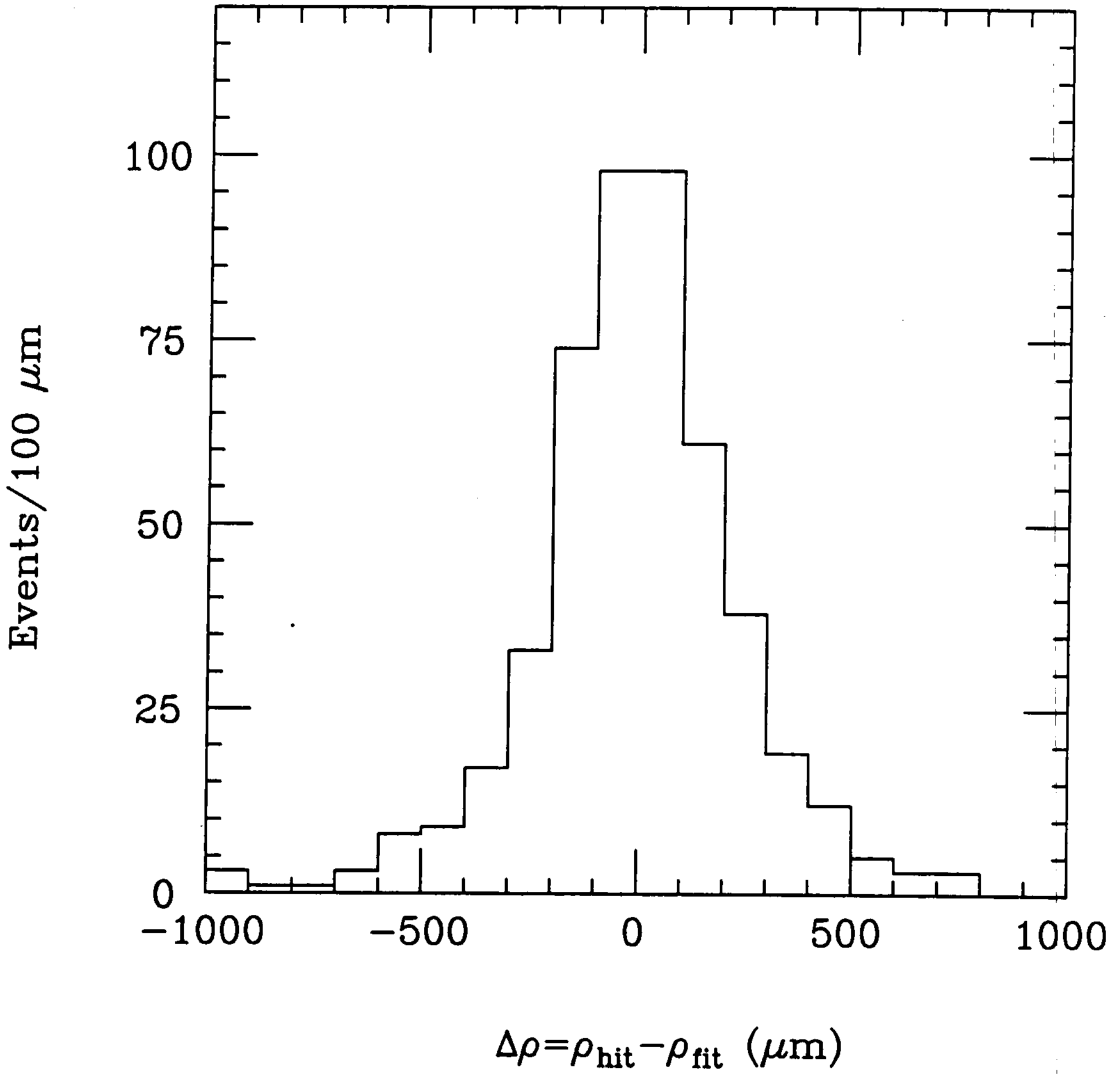

Figure 4.1: The errors in drift chamber measurement of muon tracks. The width of the curve gives the drift chamber spatial resolution.

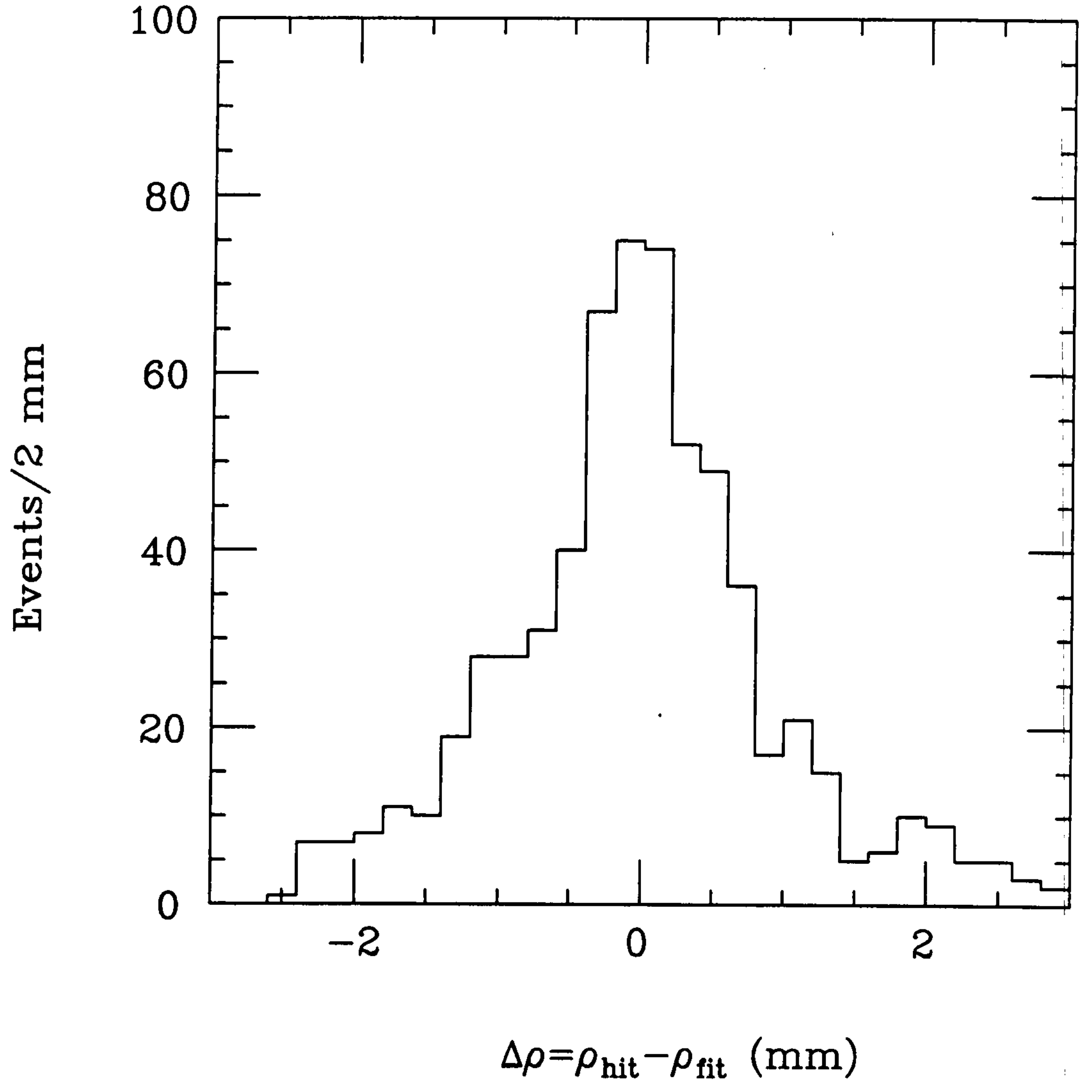

Figure 4.2: The errors in muon detector measurement of muon tracks. The width of the curve gives the muon detector spatial resolution.

required by the system. As an example of this we show the change in ρ_0 and θ in chamber 1 as a function a function of tape number during the run (Fig. 4.3).

4.3 Tracking Complicated Events

In the survey procedure described above, it is possible to try all combinations of ghost hits to fit a track, since the events are simple one-track events. This procedure will not work with events that have high multiplicity. The number of combinations needed escalates rapidly with the number of hits, which would quickly overwhelm the available computer resources. By eliminating spurious combinations in different parts of the processing, the following algorithm was able to trace tracks in complicated events.

Initially, four chambers out of the ten are picked, and all combinations over the hits in these chambers determine an initial set of preliminary track equations. Around each of these tracks we construct an imaginary cylinder. The radius of the cylinder determines how strict the fit will be, and is varied at different stages of the calculation. Points from other chambers that fit in the cylinder are stored as possibly belonging to the track. This reduces the number of combinations by eliminating points that are far from the track line. The initial requirement on the candidate tracks is that at least two extra points fit in the cylinder. This cut reduces the probability of finding fake tracks created by an accidental hit falling within the cylinder.

After this first elimination, the program will loop over all combinations, and create realistic tracks made of six or more points. A least square fit is made for each track to see how well the chosen points fit together, and tracks that do not make a minimum cut are discarded, further reducing the sample. This procedure is repeated several times with differing initial chambers and differing degrees of strictness in the cutting parameters to ensure that no tracks are lost because of

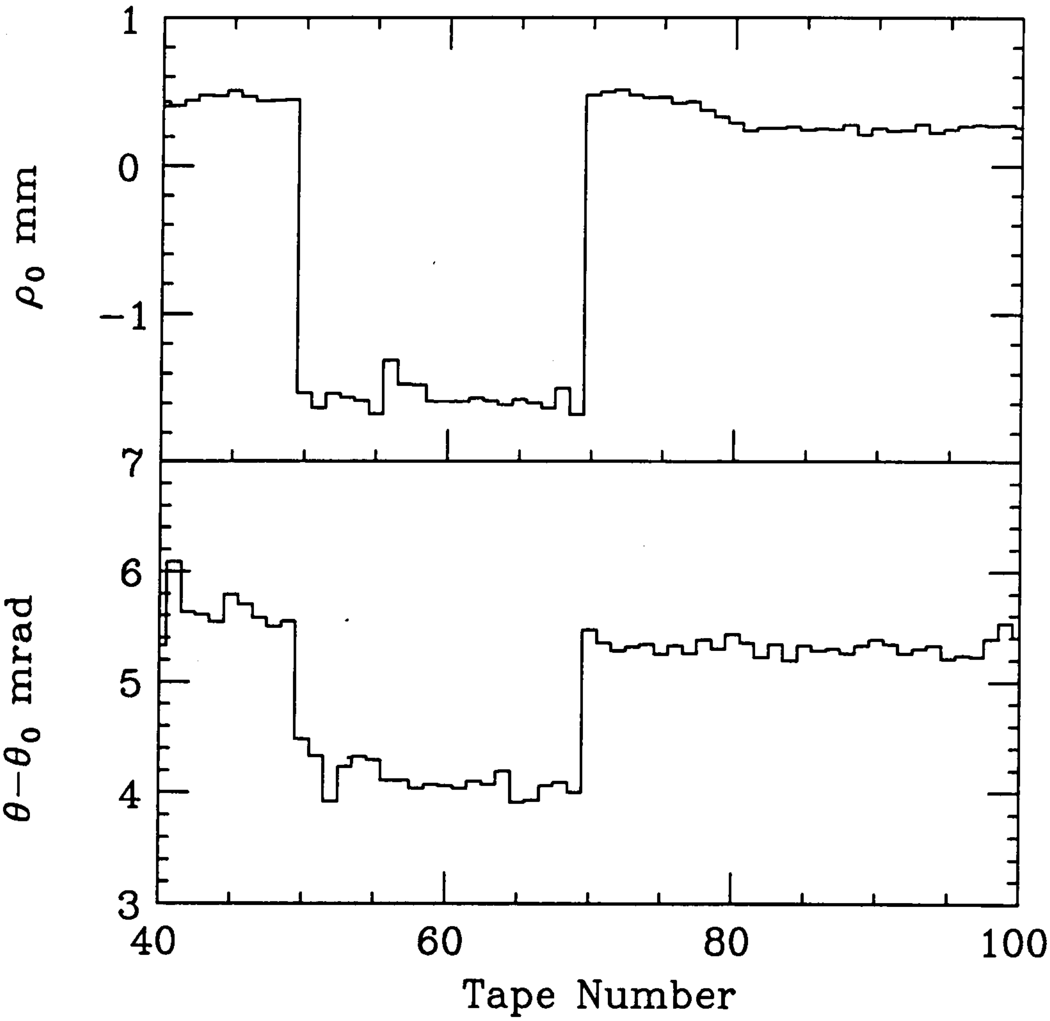

Figure 4.3: Variation of drift chamber parameters in chamber 1 vs. roll number. The changes in rolls 50 and 70 correspond to the removal of chamber 4 for maintenance.

inefficiencies in the drift chambers. All tracks that pass are stored in an array waiting for the final selection process. In the final step all tracks are tested and the ones with the largest number of points and with the best fit value are selected. In the final selection no point is allowed to appear in more than one track.

4.4 Linking to the Bubble Chamber

The measurements and calculations described up to now are totally independent of the bubble chamber measurements. They are all done using the electronic data written on computer tape. The bubble chamber data consists of photographs which are scanned and measured by a separate team of scanners and measurers. The measured visual data is subsequently processed on computer, but the electronic data and visual data are totally independent and define two different sets of coordinate systems. The events of choice to link these coordinate systems are the single muon events that have a bubble chamber picture with the magnetic field turned off, since they present the simplest situation.

In the general case, connecting two coordinate systems requires a translation and a rotation in three-dimensional space, each of which requires three parameters. The x-axis translation was taken at its measured value of $\Delta x = 331.6cm$. The y and z-axis translations were obtained from a simple average over the differences between the y and z intercepts of the bubble chamber track and the drift chamber track.

In the rotation matrix an assumption was made (and later verified) that the rotation angles (θ_x, θ_y, and θ_z) are small, so that the transformation matrix between the direction cosines (α, β, γ) of the drift chamber muons and the bubble chamber muons is:

$$\begin{pmatrix} \alpha_b \\ \beta_b \\ \gamma_b \end{pmatrix} = \begin{pmatrix} 1 & \theta_z & -\theta_y \\ -\theta_z & 1 & \theta_x \\ \theta_y & -\theta_x & 1 \end{pmatrix} \begin{pmatrix} \alpha_d \\ \beta_d \\ \gamma_d \end{pmatrix}. \tag{4.18}$$

The χ^2 technique is again used forming the sum of differences between the rotated drift chamber direction cosines and the bubble chamber ones:

$$\begin{aligned} \chi^2 \; = \; & \frac{1}{\sigma^2}\{\sum(\alpha_b - \alpha_d - \beta_d\theta_z + \gamma_d\theta_y)^2 + \\ & \sum(\beta_b - \beta_d + \alpha_d\theta_z - \gamma_d\theta_x)^2 + \\ & \sum(\gamma_b - \gamma_d - \alpha_d\theta_y + \beta_d\theta_x)^2\}. \end{aligned} \tag{4.19}$$

By differentiating with respect to the rotation angles, we get the matrix equation:

$$\begin{aligned} & \sum \begin{pmatrix} (\beta_b - \beta_d)(-\gamma_d) + (\gamma_b - \gamma_d)(\beta_d) \\ (\gamma_b - \gamma_d)(-\alpha_d) + (\alpha_b - \alpha_d)(\gamma_d) \\ (\alpha_b - \alpha_d)(-\beta_d) + (\beta_b - \beta_d)(\alpha_d) \end{pmatrix} = \\ & \sum \begin{pmatrix} -\beta_d^2 - \gamma_d^2 & \alpha_d\beta_d & \alpha_d\gamma_d \\ & -\gamma_d^2 - \alpha_d^2 & \beta_d\gamma_d \\ & & -\alpha_d^2 - \beta_d^2 \end{pmatrix} \begin{pmatrix} \theta_x \\ \theta_y \\ \theta_z \end{pmatrix}. \end{aligned} \tag{4.20}$$

The errors in the angles can be calculated in an analogous way to the method used in the previous sections.

4.5 Hybridization

The drift chambers alone usually identify several tracks in each event. Since the muon detector system with its metal shielding allows only the muon track to pass through, tracking with the combined system yielded only one muon track per event. The muon was then rotated, translated into the bubble chamber reference frame, and followed back through the magnetic field of the bubble chamber. A comparison was made between the muon track and all possible bubble chamber tracks of the event. The comparison was a χ^2 fit of the four line parameters a_y, b_y, a_z and b_z at two points — the beginning and end of the bubble chamber track. The χ^2 was of the form:

$$\chi^2 = \sum_{i=y,z;} \sum_{j=beg,end} \left[\frac{(a_{ij}^{bc} - a_{ij}^{dc})^2}{(\sigma_{a,ij}^{bc})^2 + (\sigma_{a,ij}^{dc})^2} + \frac{(b_{ij}^{bc} - b_{ij}^{dc})^2}{(\sigma_{b,ij}^{bc})^2 + (\sigma_{b,ij}^{dc})^2} \right]. \qquad (4.21)$$

The bubble chamber track information is given in the form of the x, y, and z coordinates of the beginning and end of each track, and the azimuth, dip, and inverse momentum for each track. The azimuth (φ) is the same as the spherical coordinate angle around the z-axis. The dip is given in terms of the dip angle as $s = \tan\lambda$. The inverse momentum is given as $k = 1/p\cos\lambda$. To convert to the direction cosines of the cartesian coordinate system, the following relations are employed:

$$\begin{aligned} \alpha &= \cos\lambda\cos\varphi \\ \beta &= \cos\lambda\sin\varphi \\ \gamma &= \sin\lambda. \end{aligned} \qquad (4.22)$$

The relation of the bubble chamber angles to a normal spherical coordinate system is that the azimuthal angles are equal ($\phi = \varphi$), and the polar angle is related to the dip angle by $\theta = \pi/2 - \lambda$. From the above, the values for the line parameters follow:

$$\begin{aligned} a_y &= \tan\varphi \\ a_z &= \frac{\tan\lambda}{\cos\phi}, \end{aligned} \qquad (4.23)$$

b_y and b_z follow directly from the beginning and end points of the track.

The bubble chamber errors on the above quantities are determined from the full error matrix using the standard error propagation equation. For example, the error on a_y is:

$$\sigma^2_{a_y} = \sigma^2_{\varphi\varphi}(\frac{\partial a_y}{\partial \varphi})^2 + \sigma^2_{ss}(\frac{\partial a_y}{\partial s})^2 + \sigma^2_{kk}(\frac{\partial a_y}{\partial k})^2 + \\ 2\sigma^2_{\varphi s}(\frac{\partial a_y}{\partial \varphi})(\frac{\partial a_y}{\partial s}) + 2\sigma^2_{\varphi k}(\frac{\partial a_y}{\partial \varphi})(\frac{\partial a_y}{\partial k}) + 2\sigma^2_{sk}(\frac{\partial a_y}{\partial s})(\frac{\partial a_y}{\partial k}). \tag{4.24}$$

The errors on b_y and b_z were obtained by averaging the values for the main vertex from all tracks in an event, and calculating the standard deviation of the measurements. The values used were $\sigma_y = 0.053cm$ and $\sigma_z = 0.188cm$.

If the χ^2 is large, suggesting no fit, the track is discarded. If the χ^2 is small, the momentum of the track is varied to further minimize the χ^2, and to obtain a new value of momentum p_{hyb}. The error on the hybrid momentum is determined from the maximum likelihood method:

$$\sigma^2_k = [-\frac{d^2}{dk^2}\ln L(k)]^{-1} = [\frac{1}{2}\frac{d^2}{dk^2}\chi^2(k)]^{-1}. \tag{4.25}$$

It is useful to define another quality factor for the momentum fit besides the χ^2. This will show by how many standard deviations the bubble chamber momentum varies from the hybrid fit: $\Delta p = |p_{bc} - p_{hyb}|/\sigma_p$. All this information is written to a data file for later use.

The hybrid information was not available for all events. The efficiency of an individual cell in the downstream system was of the order of 95%, but the overall efficiency of the system as a whole, was lower. Geometric acceptance, problems with false triggers, and tracking difficulties lowered the efficiency to 35%. For events with no hybrid information, a kinematic method for finding the muon was used which will be described in chapter 5.

When an event has hybrid information associated with it, a decision has to be made whether to use this extra information. The first check is the difference between the lowest χ^2 fit and the next to lowest. If the two differ by less than a factor of two, the hybrid data is inconclusive and is abandoned. The next check is if $\chi^2 < 50.0$ and $\chi^2 \Delta p < 200.0$. If these conditions are not met, the fit is poor and again is not used. After these cuts, the hybrid data is used to identify the muon but not to assign a momentum. To use the hybrid momentum fit, tighter conditions are required: $\chi^2 < 20.0$, $\chi^2 \Delta p < 80.0$ and length of the track $> 15.0cm$. The hybrid momentum was used in 78% of the events in which the hybrid data determined the muon.

CHAPTER 5

DATA PROCESSING AND ANALYSIS

Much preparatory work is needed in order to bring the data into a form that can be analyzed conveniently. This chapter covers the preliminary steps of data processing and analysis used to prepare the final results presented in the next chapters. The modification added to the Lund Monte- Carlo program will be presented. The Monte-Carlo proved invaluable in calculating efficiencies and background presented in this chapter, and in picking out the signal from the background in the final results. The remaining sections are devoted to explanation of the cuts needed to clean the charged current sample, picking out the muon, and calculating the neutrino energy.

5.1 Energy Simulation

The first step in simulating the events in the experiment was to get the neutrino energy distribution. This was done using the Fermilab simulation program called NUADA [21]. NUADA uses experimental data to predict the production of $\pi's$ and $K's$ from protons in the Fermilab beam line. The trajectory of the particles passing through the quadrupole triplet magnets into the decay region is then calculated. The total flux of neutrinos reaching the target is estimated as a function of energy and solid angle. The program also predicts an interaction rate for our detector, since the cross section is proportional to the neutrino energy. The predicted curves for the E745 bubble chamber is shown in Fig. 5.1. The large peak comes from the more numerous $\pi's$, and the smaller peak at higher energies derives from $K's$.

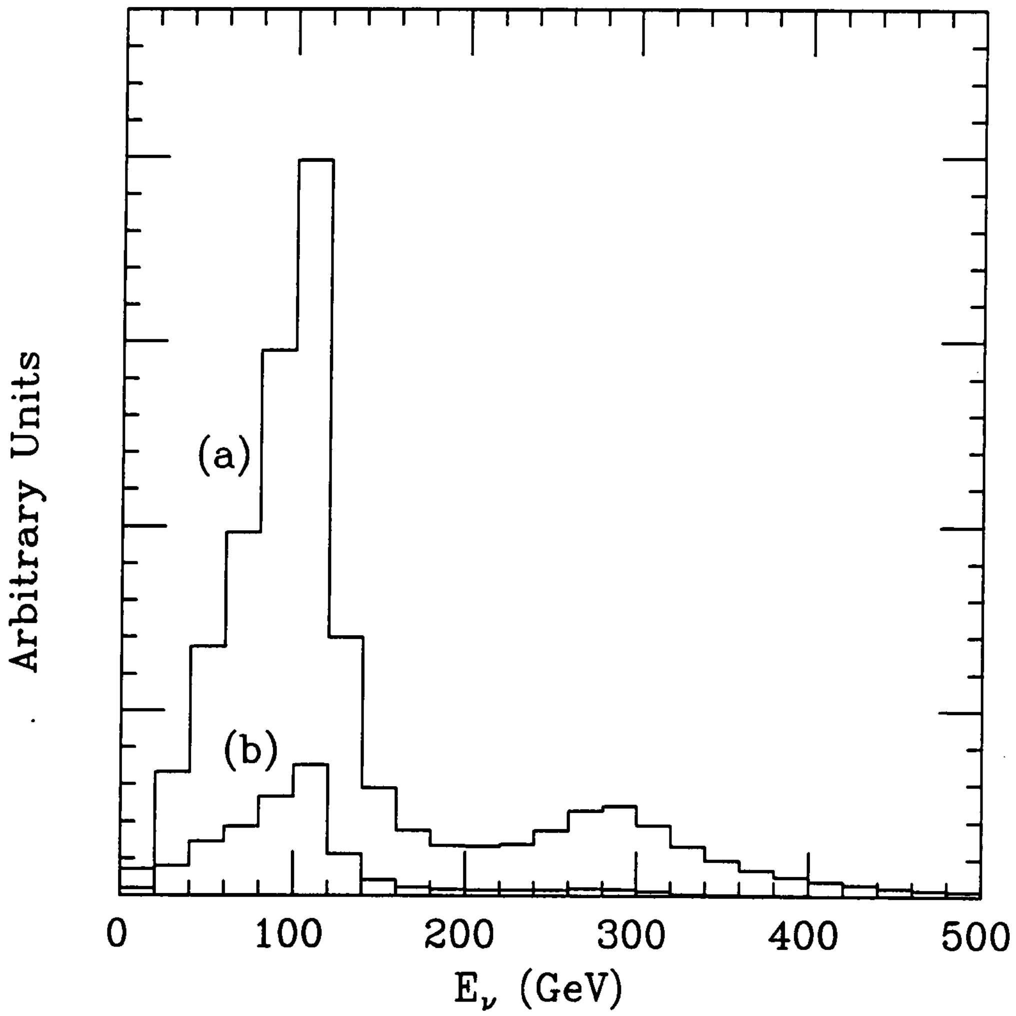

Figure 5.1: (a) Neutrino energy distribution of events in the bubble chamber from the NUADA simulation; (b) Anti-neutrino energy.

5.2 The Lund Monte-Carlo

5.2.1 Introduction

The Lund Monte-Carlo [22] was used to simulate the events in E745. The Lund program simulates high energy interactions by creating complete events from parametrizations of theoretical and experimental results. The version used was specifically created for deep inelastic lepton-nucleon scattering, and creates the events in two distinct steps. The first is the scattering of the lepton from a quark in the nucleon, and the second is the fragmentation or conversion of the quark fragments into hadrons.

The program LEPTO 4.4 simulates the deep inelastic lepton-quark interaction. The type of interaction wanted, neutrino or anti-neutrino, charged current or neutral current, is supplied before the call to LEPTO. The fraction of neutrino events is estimated at 75% from the data, with the remainder being anti-neutrino events. The ratio of neutral current to charged current, is taken as 0.30 from Ref. [24]. The (anti-)neutrino energy is generated from the Nuada information presented earlier in Fig. 5.1. An additional input which is required is the target composition given for Freon as $A = 18.7$ and $Z = 8.9$. LEPTO uses the known lepton-quark cross sections to pick a target quark and assign a momentum transfer. The struck quark and the spectator di-quark form the output of LEPTO and the input to the fragmentation step.

The fragmentation step is based on the theoretical Lund model and is implemented in the program JETSET 6.2. The analog to the strong force field lines between the quarks are described in the model as flexible strings. The strong force potential energy is assumed to rise linearly with separation, and this is represented as a stretching of the string. In a QCD picture, $q\bar{q}$ pairs are created from the energy of the field. The analog in the model is when the potential energy stored in the string is big enough, the string breaks, creating $q\bar{q}$ pairs connected to the broken edges and conserving momentum, energy and all relevant quantum numbers. This process of breaking strings continues as long as a string has a minimum amount of energy. When the fragmentation ceases the quarks are combined into hadrons.

The Lund model also contains the branching ratios for the unstable particles, and it proceeds to model the decays, so that the final output is a collection of particles as would actually be seen in an ideal experiment with no errors and perfect acceptance. To be able to compare the model to our experiment, the effects due to the imperfection of the detector system must be added to the idealized output. This process is described in the next section.

5.2.2 Acceptance Corrections

The only acceptance correction applied was to neutral particles that had a chance of converting into visible particles in the bubble chamber volume. The following corrections were applied:

1. Neutral strange particles (K^0_S, Λ^0) will be seen in the bubble chamber if their decay distance is less than the distance of the interaction vertex to the bubble chamber wall d_{max}, provided they decay through a mode that can be seen in the bubble chamber. The probability that they will decay within a distance d less than d_{max} is:

$$P_{decay}(d < d_{max}) = \exp(-\frac{d_{max}}{\lambda_{dis}}) \tag{5.1}$$

$$\lambda_{dis} = \gamma\beta c\tau = p/mc\tau, \tag{5.2}$$

where λ_{dis} is the mean flight path of a particle with momentum p and mass m. The values for $c\tau$ are [23] 2.675 cm for the K^0_S and 7.89 cm for the Λ. The visible decay modes are:

$$K^0_S \rightarrow \pi^+\pi^- \quad (68.6\%) \tag{5.3}$$

$$\Lambda \rightarrow p\pi^- \quad (64.2\%), \tag{5.4}$$

In addition if the decay distance is shorter than 1 cm the vee itself is assumed not to be seen [15] and the decay products are treated as if they emanated from the primary vertex. K_L^0's are assumed not to be detected.

2. Photons can only be seen in the bubble chamber if they convert into e^+e^- pairs. The probability that a photon with energy above 1 GeV convert in the distance d_{max} is given by:

$$P_{\gamma\rightarrow e^+e^-}(d < d_{max}) = \exp(-\frac{d_{max}}{\lambda_{rad}}), \tag{5.5}$$

   where $\lambda_{rad} = 27cm$ is the radiation length for the liquid in the bubble chamber [16].

3. Neutrons can be detected if they interact and form a visible neutron star. The probability that a neutron interacts within the distance d_{max} is given by:

$$P_{interaction}(d < d_{max}) = \exp(-\frac{d_{max}}{\lambda_{int}}), \tag{5.6}$$

   where $\lambda_{int} = 57cm$ is the interaction length for the bubble chamber [16].

5.2.3 Measurement Error Correction

The next step in simulating the experiment is to add the errors in track measurements to the Lund Monte-Carlo tracks. The quantities that are easiest to modify are the track parameters that have a gaussian error distribution — the same ones that are output from TVGP (with θ, ϕ being the spherical coordinate angles):

1. The inverse momentum: $k = 1/p\cos\lambda$.

2. The tangent of the dip angle: $\tan\lambda \approx \lambda = \pi/2 - \theta$.

3. The azimuth: ϕ.

The error in momentum is found in a similar manner to the way TVGP would perform the calculation [19]. A particle traveling with momentum $p(GeV/c)$ perpendicular to a magnetic field describes an arc in space with a curvature $r(cm)$:

$$p = 2.9979 \times 10^{-4} r B, \tag{5.7}$$

where B is the magnetic field in kilogauss. A more convenient quantity to work with, is the sagitta of the track defined as the maximum distance between the arc and its chord. From geometry, the sagitta in microns is equal to:

$$s = r[1 - \cos(\frac{l}{2r})] \times 10^4 \tag{5.8}$$

where l is the length of the track in cm. The sagitta is a convenient quantity to employ, since neglecting the small errors in the measurement of the length and magnetic field, gives the simple relation:

$$\frac{\sigma_s}{s} \simeq \frac{\sigma_p}{p} \simeq \frac{\sigma_k}{k}. \tag{5.9}$$

This enables us to find the error in momentum from the error in sagitta.

The first contribution to the error in sagitta is the multiple coulomb scattering in freon. This can be estimated from [23]:

$$\sigma_s^{coul} = \frac{141 l^{3/2}}{4p\beta(3\lambda_{rad})^{1/2}}[1 + \frac{1}{9}\log_{10}(\frac{l}{\lambda_{rad}})]. \tag{5.10}$$

The second contribution to the sagitta error is the digitization error of the track points on film. The full TVGP procedure is simulated to find the sagitta error. The original track momentum and length are supplied, and a track arc is created. The number of measured points is determined from the length, and these points are evenly distributed along the arc with an error setting of $12\mu m$ on film, which seemed to give the best agreement between the Monte-Carlo and the data. The

TVGP circle fit routines are then used to find σ_s^{meas}. Finally the total error on the sagitta is found from:

$$\sigma_s = \sqrt{\sigma_{coul}^2 + \sigma_{meas}^2}. \tag{5.11}$$

The errors on the dip and azimuth of tracks, emerging from TVGP when split into different length bins, were seen to have the following characteristics (Fig. 5.2): The errors are distributed in an approximate gaussian, with the average and standard deviation being a function of the length of the track. When plotted, as a function of the inverse momentum, there seems to be a linear lower limit on the error. To find a value for the error, a random number is generated from the shape of a gaussian distribution with the appropriate average and standard deviation, and kept if it is above the lower linear bound.

To actually incorporate the error values, a random number is generated according to a gaussian distribution with a mean of zero and a standard deviation of one, multiplied by the estimated error and then added to the actual value of k, λ, or ϕ. With k, this procedure is not neccesary, since σ_k is generated in a random manner apriori. For neutral tracks that convert to visible form in the bubble chamber, the length of the visible portion is generated from the previously mentioned probability distributions, and the calculated error is then multiplied by a factor of $\sqrt{2}$ [18]. This is done to compensate for the fact that in the bubble chamber the neutral track parameters are usually calculated by the addition of two (or more) daughter tracks, each with roughly the same errors. An extensive comparison of multiplicities and kinematical variables between the experiment and the Monte-Carlo is presented in Figs. 5.3, 5.4, 5.5, 5.6. The only normalization applied to all the curves is to equate the area under the curves. The agreement is very good with some understood exceptions:

1. The Lund Monte-Carlo is a simulation designated for deep inelastic scattering, a process where the neutrino interacts with one of the quarks in the

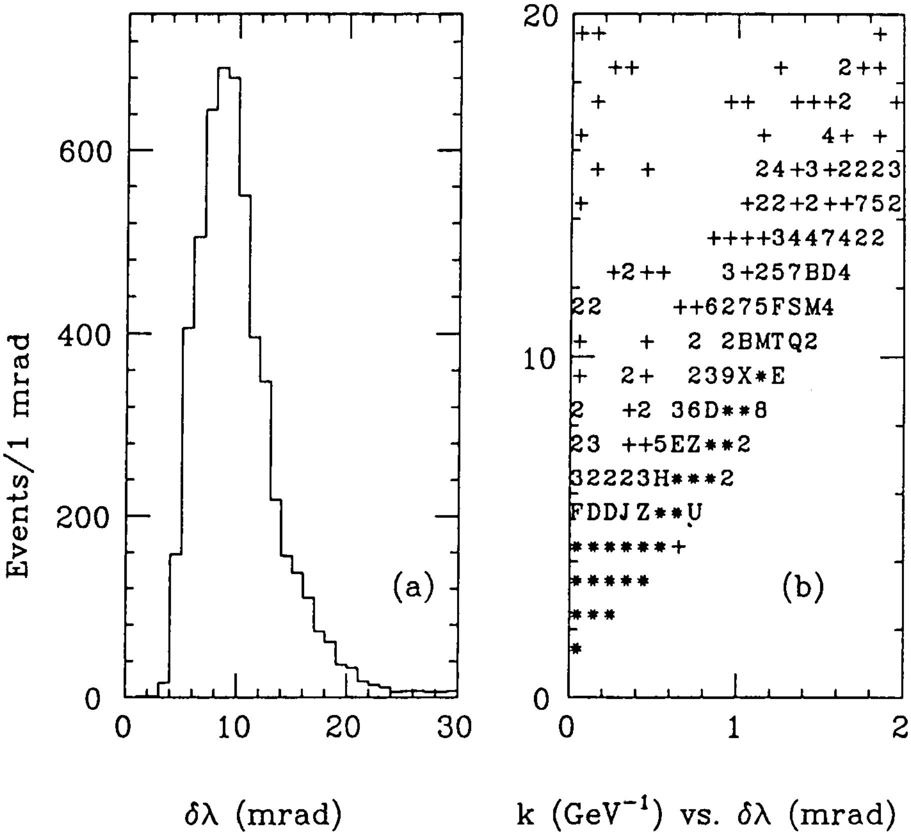

Figure 5.2: (a) $\delta\lambda$ for tracks of length $45 < l < 55$ cm. (b) k vs. $\delta\lambda$.

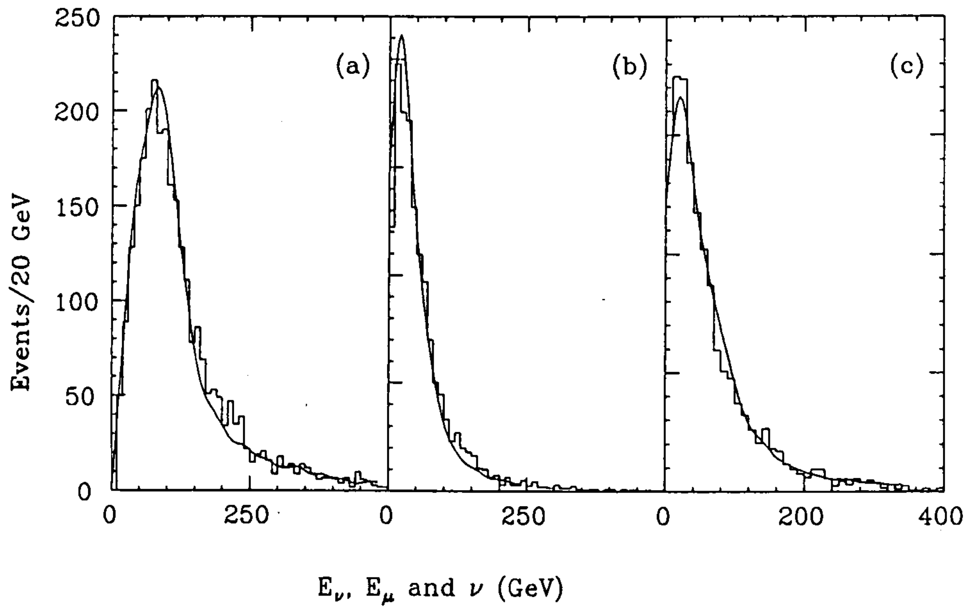

Figure 5.3: Comparison of the data (histogram) and the Monte-Carlo (solid curve) of (a)E_ν; (b)E_μ; (c)ν.

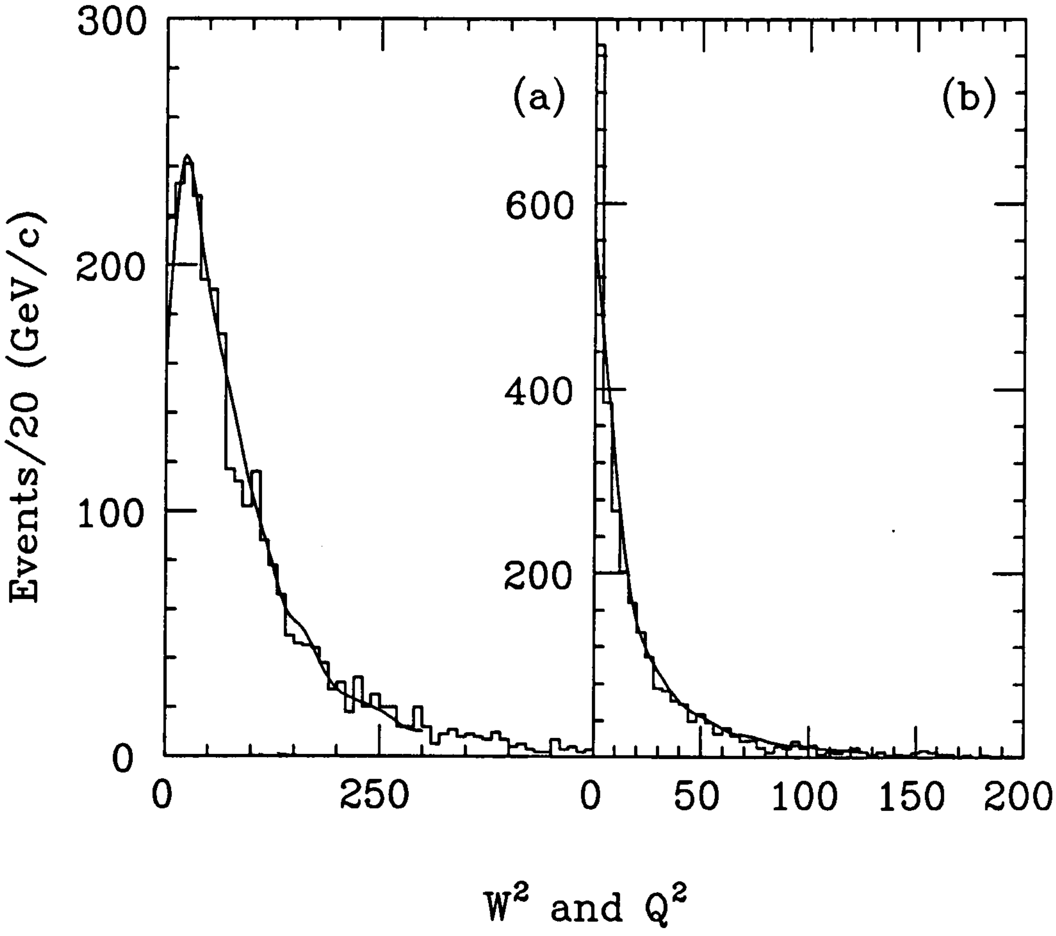

Figure 5.4: Comparison of the data (histogram) and the Monte-Carlo (solid curve) of (a)W^2; (b)Q^2.

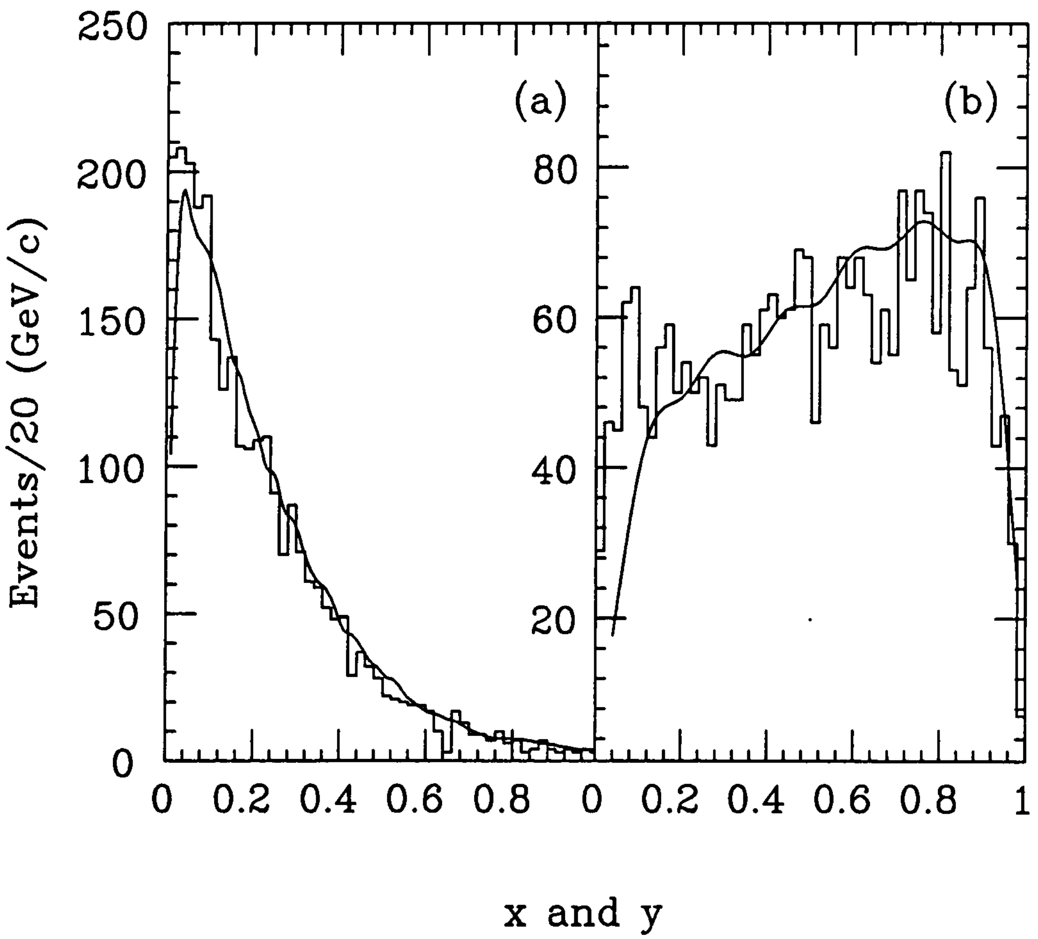

Figure 5.5: Comparison of the data (histogram) and the Monte-Carlo (solid curve) of (a)x; (b)y.

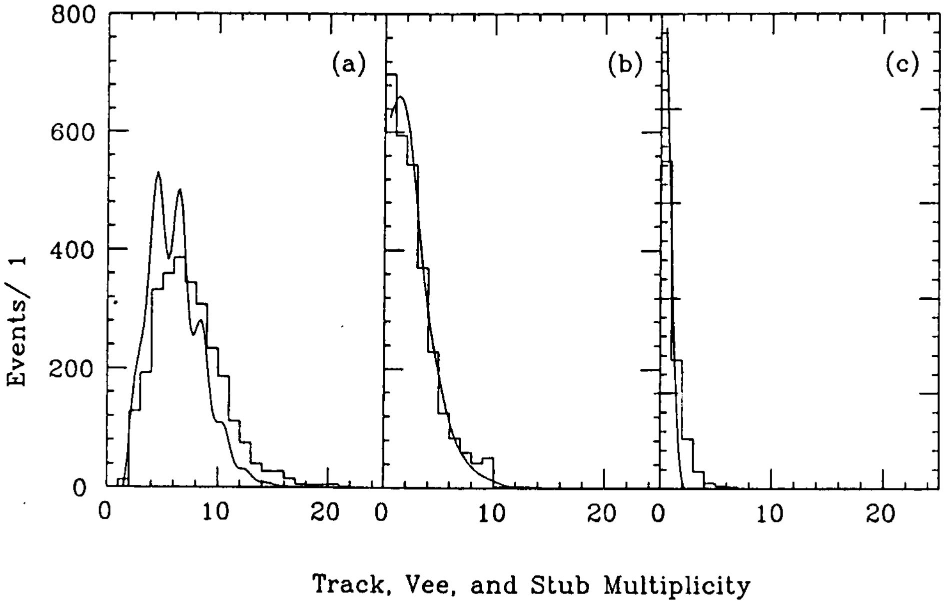

Figure 5.6: Comparison of the data (solid histogram) and the Monte-Carlo (dashed histogram) of (a)track; (b)vee; and (c)stub multiplicity.

nucleus. It is not as succesful for diffractive interactions where the collision is a glancing reaction with the nucleon. The agreement with the data in the first bin of the kinematical parameter plots is not as good as with the other bins.

2. Stubs are nuclear debris that arises when the nucleus breaks up in an interaction. On film these low energy protons appear as short tracks emerging from the vertex. The discrepancy in the stub multiplicity occurs because the Monte-Carlo only simulates interactions on free protons and neutrons.

3. The peaks at even track multiplicity that the Monte-Carlo generates, arise for the same reason. Our beam is mostly made of neutrinos which generate W^+'s, which can only interact with the down quark (charge $-\frac{1}{3}$). Neutrons have twice as many valence down quarks as do protons, so the preferred interaction for the simulation is neutrino on neutron, and conservation of charge requires an even multiplicity. In the real world, the interaction involves the nucleus, and as we know from the EMC effect [62,28], quarks behave differently in a nuclear environment.

4. The higher multiplicity of the data arises from secondary interactions in the bubble chamber that occur very close to the primary vertex, and can't be distinguised by the scanners. Another effect is artificial and arises from the normalization failing to take into account the discrepancies at the even multiplicities.

5.3 Muon Identification

When hybrid information was not available for an event the F_{max} kinematical method [25] was used to find the muon. The method involves finding the track with the maximum value of the F parameter. The F parameter is defined as:

$$F = \frac{F_1 F_2}{F_3}, \tag{5.12}$$

where the calculation of each one of the parts of F will be illustrated on track number 1 of an n track event. $\vec{p_i}$ will designate the momentum vector of the ith track. $\vec{b}$ will designate the beam direction, and a hat will designate a unit vector.

1. F_1 is the transverse momentum of the track relative to the beam direction:

   $$F_1(1) = |\vec{p_1}|\sqrt{1 - (\hat{p}_1 \cdot \hat{b})^2}. \tag{5.13}$$

   F_1 will function as an analyzer, since the muon usually has a higher transverse momentum than other tracks in the event.

2. Defining the sum of the rest of the tracks as $\vec{p_r} = \sum_{i=2}^{n} \vec{p_i}$, F_2 is the transverse momentum of the track relative to $\vec{p_r}$:

   $$F_2(1) = |\vec{p_1}|\sqrt{1 - (\hat{p}_1 \cdot \hat{p}_r)^2}. \tag{5.14}$$

   F_2 is useful in discriminating the muon from the other tracks, since the muon goes off with opposite transverse momentum to the other hadrons.

3. F_3 is a composite of F_2 from all the other tracks, and is defined as the root of the sum of the squares of the transverse momentum of the rest of the tracks relative to $\vec{p_r}$:

   $$F_3(1) = \sqrt{\sum_{i=2}^{n} |\vec{p_i}|^2 (1 - (\hat{p}_i \cdot \hat{p}_r)^2)} \tag{5.15}$$

Each of the above can be used individually to separate the muon track, but together they are more efficient. The events that did hybridize succesfully, form an excellent sample of events with which to check our procedure. In a sample of hybridized events for which the muon is known, the F_{max} method proved to be 93 ± 4% efficient in good agreement with the Monte-Carlo result of 94%. An illustration of the efficiency of the F_{max} method is presented in Fig. 5.7.

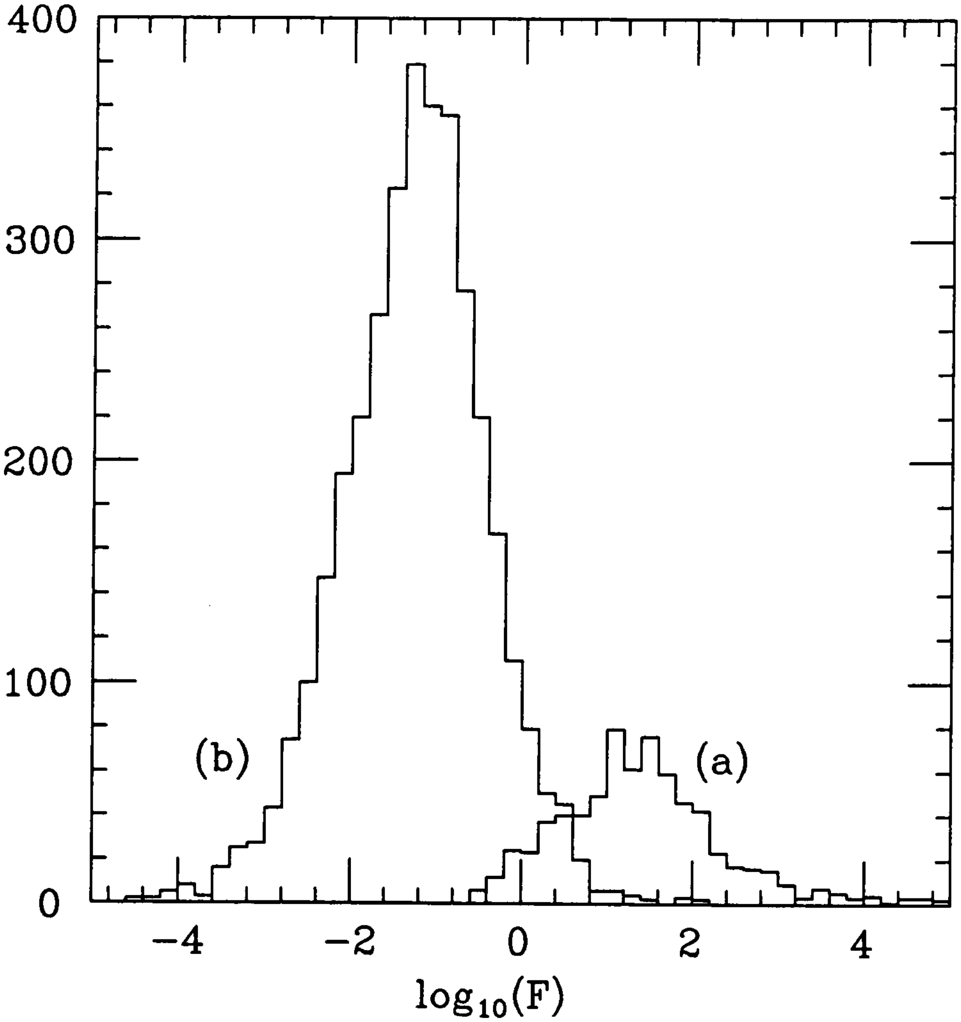

Figure 5.7: Curve (a) is the F distribution for tracks identified as muons by hybridization. Curve (b) is for the other tracks in the same events.

5.4 Charged Current Selection

The main background to charged current events came from two different sources:

1. Neutral current events which are expected in known numbers [24] and can be well simulated and studied with the Lund Monte-Carlo. The important characteristic of these events, that helps in eliminating them from our sample, is the lack of a muon and a lower visible energy, since the departing neutrino carries much of the energy.

2. Neutral hadrons such as K_L^0 and neutrons are expected to be generated from neutrino interactions upstream of the bubble chamber, such as in the magnet. Some of these make it to the bubble chamber and interact creating fake neutrino events. These cannot be simulated with the Monte-Carlo, but fortunately a sample of these events is available [15]. To get a sample that simulates the neutral hadron background we take all neutral secondary interactions in the bubble chamber. This sample consists of 824 events with some contamination from events with two neutrino events in the same frame. From the 200,000 pictures taken in E745, and the 5959 neutrino candidate events, only about 60% are neutrino events (a rough estimate from the events remaining after the longitudinal momentum cut). This makes the probability for two neutrino reactions to occur in the same frame about 1:3000, so this happens for approximately 60 events. The main feature of these events is, as before, a lack of a muon and a very low visible energy, since the hadrons carry less energy than the neutrinos.

As in the F_{max} case, the hybridized events form a sample of charged current events, with which to check the efficiency of the selection algorithm. The list of criteria an event must follow to be included in the final sample, is:

1. It must pass TVGP with at least two good tracks.

2. The total visible longitudinal momentum must be above $10 GeV/c$. This eliminates a big portion of the neutral hadron reactions that have a lower average energy. Fig. 5.8 compares the longitudinal momentum distribution of charged current events to neutral current and neutral hadron events. The number of remaining neutral hadron events after after this cut is larger than expected (~ 110), because of the neutrino contamination mentioned earlier.

3. The transverse component of the selected muon track, with respect to the other hadrons in the event, must be larger than $1.5\,GeV/c$. This again selectively eliminates more of the neutral current and neutral hadron events, than the charged current ones. Fig 5.9 illustrates this cut.

4. The angle Φ, defined as the angle between the muon and the vector sum of the rest of the hadrons in the y-z plane, must be larger than $60°$ [25]. In a charged current event with all hadrons known, $\Phi = 180°$, since the muon takes the opposite amount of transverse momentum to the hadrons. In realistic events, with the neutral hadrons missing, the angle is reduced somewhat, but still remains large. In neutral current or neutral hadron events Φ is approximately evenly distributed, so the cut further reduces the background. The differences between the distributions is shown in Fig. 5.10.

5. The distance from the main vertex to the bubble chamber wall must be greater than $20cm$. This is a fiducial volume cut to minimize scanning and measuring losses.

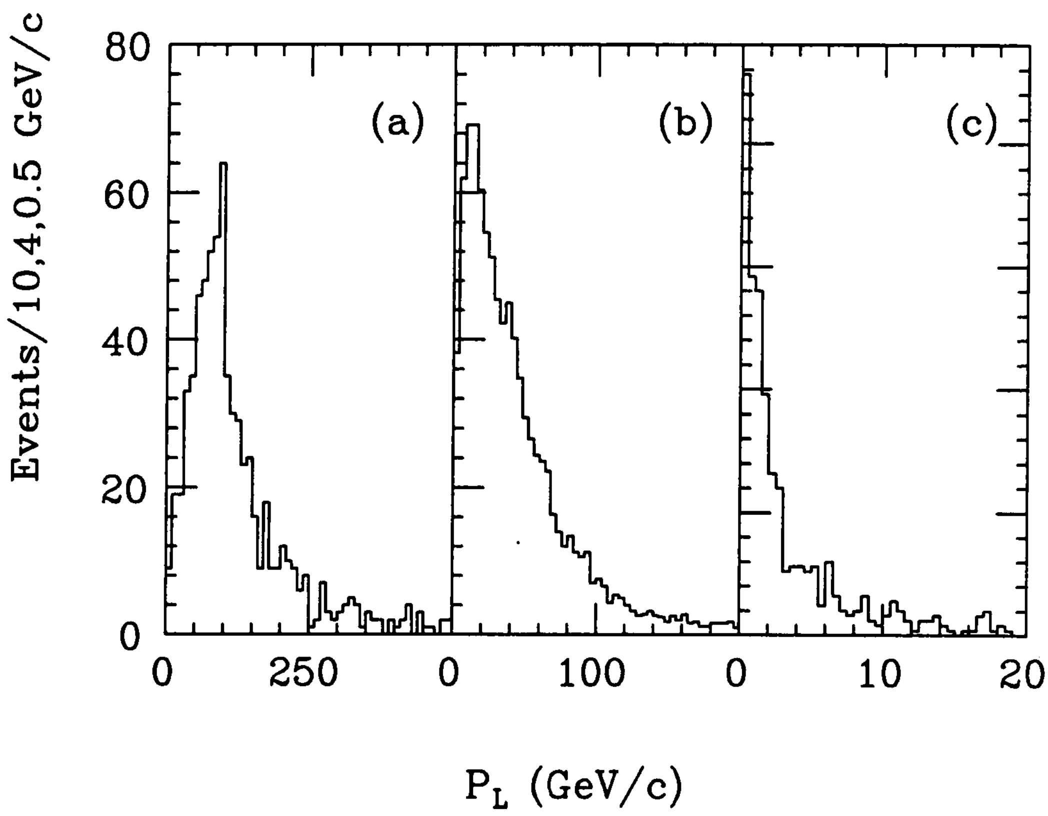

Figure 5.8: (a) $\sum P_L$ for the charged current events (b) for the neutral current (c) for the neutral hadron.

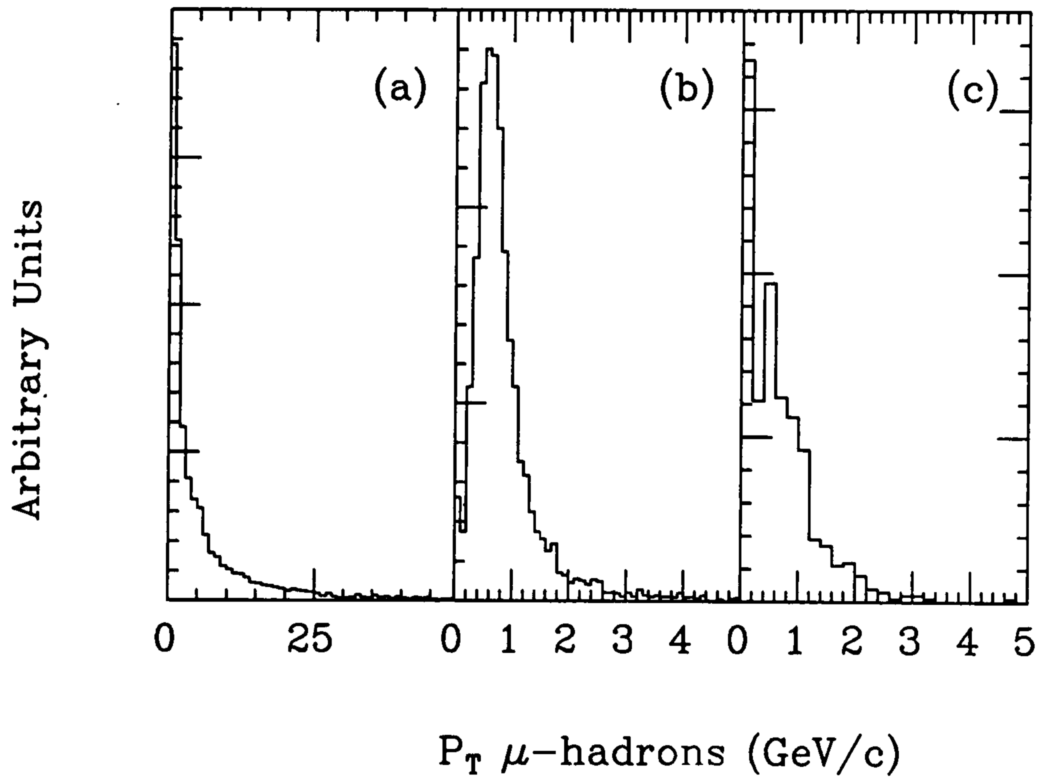

Figure 5.9: (a) $P_T^{\mu-hadrons}$ for the charged current events (b) for the neutral current (c) for the neutral hadron.

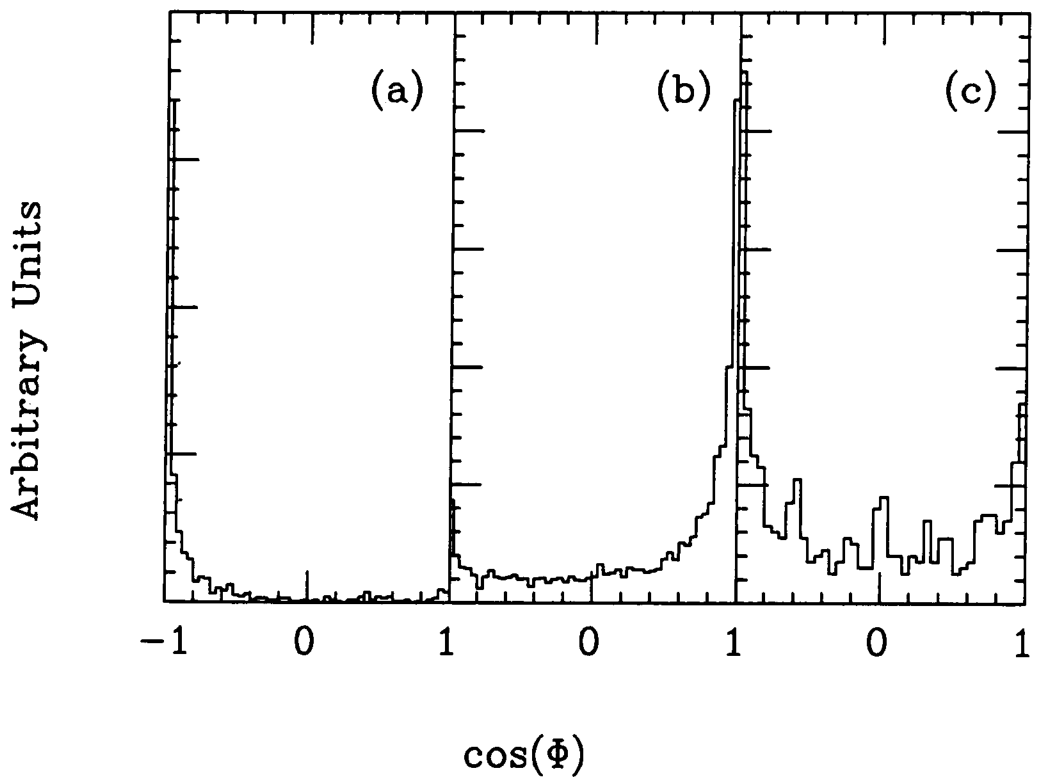

Figure 5.10: (a) $\cos\Phi$ for the charged current events (b) for the neutral current (c) for the neutral hadron.

6. The error in the muon momentum must be smaller than half the value of the momentum itself, or: $\sigma_p/p \leq 0.5$. This again insures that the event is well measured and there is a high probability that the muon charge is correct.

7. The kinematical variables must have physically possible values such as: $1 > x > 0$, $\nu > 0$, $W^2 > 0$, $Q^2 > 0$. This eliminates events that have bad measurement errors.

A summary of the cuts and their effect on the data is presented in Table 5.1. The table shows the number of charged current events remaining after each cut, the charged current efficiency and background. The efficiency is the fraction of charged current events remaining in the final sample from the estimated total number in the beginning. The background is the estimated fraction of non- charged current events remaining in the final sample. The table has been calculated only with the neutral current background, since the Monte-Carlo cannot simulate the the neutral hadron background. A separate study on our neutral hadron sample [15] indicated that only 1.2% of the neutral hadron events can pass through the cuts; that indicates that fewer than 5 of these events are in the final sample, a result too small to appreciably affect the numbers presented.

5.5 Energy Determination

Much time was spent studying different methods to find the neutrino energy, but in the final analysis, the simplest and most straightforward method turned out to give the best results. The Bonn method [26] makes the assumption that the missing neutral momentum in the event is on the average in the same direction as the visible hadronic momentum. Since the neutral transverse momentum is known to equal the missing transverse momentum in the event, a simple calculation gives the missing longitudinal momentum. Conservation of transverse

Table 5.1: Event Selection Table.

Cut	No. Events	Efficiency	Background
Total Number	8902		
Pass TVGP	7373		
μ exists	7319		
$\sum P_L > 10GeV/c$	5529	0.94	0.26
$P_T^{\mu-h} > 1.5GeV/c$	4087	0.68	0.071
$\cos\Phi < 0.5$	3625	0.61	0.041
Fiducial $l > 20cm$	3059	0.57	0.035
$\delta p_\mu/p_\mu < 0.5$	2384	0.46	0.035
Kinemtic cuts	2323	0.46	0.035
Charged Current	1792	0.45	0.032

momentum gives:

$$|\vec{p}_T^{neutral}| = \vec{p}_T^{\mu} + \vec{p}_T^{charge}, \tag{5.16}$$

and conservation of longitudinal momentum gives:

$$E_\nu = p_\nu = p_L^\mu + p_L^{charge} + p_L^{neutral}. \tag{5.17}$$

The assumption of the Bonn method is that:

$$\frac{p_L^{charge}}{p_T^{charge}} = \frac{p_L^{neutral}}{p_T^{neutral}}. \tag{5.18}$$

Substituting for $p_L^{neutral}$, we get an estimate of the energy in terms of known quantities:

$$E_\nu = p_L^\mu + p_L^{charge}\left[1 + \frac{p_T^{neutral}}{p_T^{charge}}\right] \tag{5.19}$$

The error introduced by this approximation can be checked with the Monte- Carlo, and is represented in Fig 5.11 with the average error being of the order of 17%.

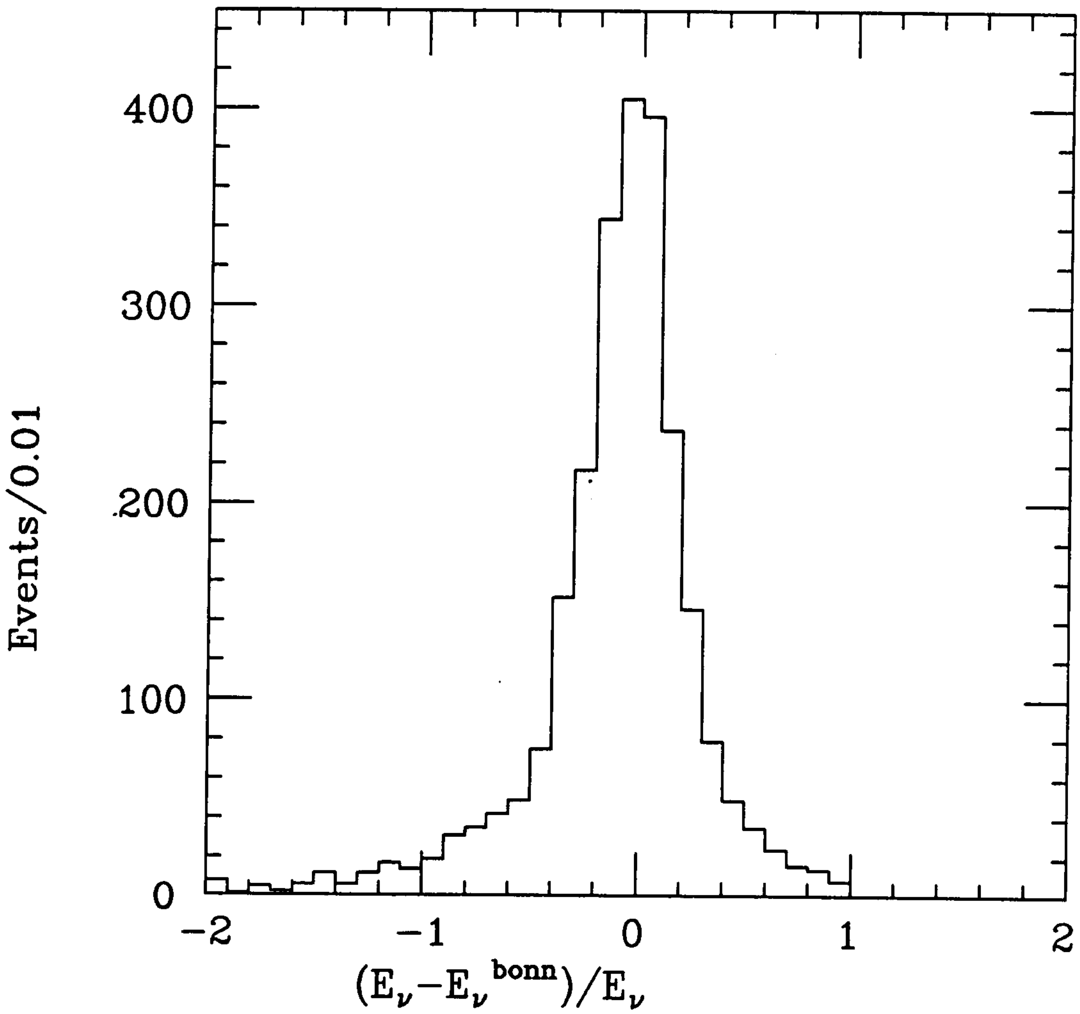

Figure 5.11: Error distributions of the neutrino energy from the Bonn method

CHAPTER 6

S-CHANNEL HELICITY CONSERVATION IN PHOTOPRODUCTION

After presenting the VDM predictions in chapter 2 we proceed to check their consequences. In this chapter we investigate the results from the BC 72-73 photoproduction experiment at SLAC. Since the author only joined this experiment at a late stage no details of the experiment will be given other than than those mentioned in the following reproduction of the published reference [1]. This worked served as the motivation for the neutrino experiment analysis presented in the next chapter.

6.1 Introduction

Conservation of s-channel helicity (SCHC) in hadronic diffraction has been of experimental [29]-[36] and theoretical [37]-[39] interest for over a decade. SCHC follows naturally from QCD-based models of the Pomeron, such as two gluon exchange [9]. Evidence for SCHC has been reported in the elastic- diffraction processes $\gamma p \rightarrow \rho p$ [29] and $\pi N \rightarrow \pi N$ [30]. It has been speculated that it might also be valid in inelastic diffraction [37], but this is not found to be true in πp [31], Kp [32], and pp [33,38] experiments. Thus, SCHC is no longer viewed as a general rule for inelastic diffraction, although evidence suggests that in some cases the inelastic diffraction which displays nonconservation of s-channel helicity may result from two production mechanisms, one of which exhibits SCHC [34,35]. Furthermore, analysis based on the Deck model has explained the patterns of s- and t-channel helicity conservation in meson-diffraction dissociation [39].

Polarized ρ mesons produced by linearly polarized photons on hydrogen provide a good test of SCHC. Previous work has shown evidence for SCHC in inclusive inelastic ρ_0 photoproduction [36,40]. If SCHC holds in the inelastic-diffractive reaction $\gamma p \rightarrow \rho N^*$, the polar- and azimuthal- angular distribution of the ρ^0 decay in the helicity system will follow the well-known prediction [41]:

$$W(\cos\theta, \psi) = (3\sin^2\theta/8\pi)(1 + P_\gamma \cos 2\psi) \qquad (6.1)$$

independent of t. In what follows we report evidence of SCHC in $\gamma p \rightarrow \rho N^*$ from an analysis of a clean sample of 1934 such events produced in the SLAC Hybrid Facility exposed to a linearly polarized $20 - GeV$ photon beam.

6.2 Experimental Details

The experiment has been described in previous publications [42,43,44,45]. The linearly polarized monochromatic photon beam is formed by backscattering and ultraviolet laser beam from the SLAC $30 - GeV$ primary electron beam. The backscattered photons have a 52% lenear polarization. The SLAC Hybrid Facility consists of a $40in.$ hydrogen bubble chamber, with its flashlamps triggered by signals from downstream detectors: proportional wire chambers [43], Cherenkov counters [44], and a lead-glass wall [45]. The trigger accepts $(88 \pm 3)\%$ of the total cross section. The data predented here have been corrected on an event-by-event basis for the relatively small losses in the trigger efficiency. The average weight is 1.11 for the inelastic ρ^0 production events and the acceptance varies less than 20% over the t', mass, and the angle ranges of the events used in the reaction $\gamma p \rightarrow \rho^0_{fast} p\pi^+\pi^-$.

6.3 Evidence for Diffractive Inelastic ρ^0 Photoproduction

A sample of 6468 events having a three-constraint fit to the reaction $\gamma p \rightarrow p\pi^+\pi^+\pi^-\pi^-$ with total energy between 15 and 20 GeV has been selected from the 300,000 hadronic events measured in this experiment. Fig. 6.1(a) shows the two-pion effective masses for this final state; histogram A is the spectrum for all $\pi^+\pi^-$ combinations (four per event), while curve B is the sum of spectra for the two same- sign combinations. The four-pion effective mass distribution, shown in Fig. 6.1(b), is dominated by $\rho'(1600)$ production. Fig. 6.2 gives the two-pion momentum spectra for selections described below. From Figs. 6.1 and 6.2 the following qualitative conclusions can be drawn.

(a) The $\pi^+\pi^-$ mass spectrum [histogram A, Fig. 6.1(a)] shows a prominent ρ^0 signal which rises above the combinatorial background represented by histogram B.

(b) The $\rho'(1600)$ signal is enhanced if only those $\pi^+\pi^-$ masses in the ρ^0 region ($M_{\pi^+\pi^-} < 1000 MeV/c^2$) are selected from histogram A in Fig. 6.1(a); this effect is demonstrated by histogram B in Fig. 6.1(b) and indicates that there is a substantial ρ^0 signal coming from the decay of $\rho'(1600)$.

(c) If the $\pi^+\pi^-$ system is further restricted to have momentum $> 16 GeV/c$ and $|t'| = |t - t_{min}| < 0.5\ (GeV/c)^2$ the histogram C of Fig. 6.1(b) is obtained; the $\rho'(1600)$ signal is completely suppressed. This indicates that the ρ^0's coming from $\rho'(1600)$ decay have a much softer momentum spectrum than those produced diffractively.

(d) Curve A in Fig. 6.2 shows the momentum spectrum for $\pi^+\pi^-$ combinations having masses in the ρ^0 region ($M_{\pi^+\pi^-} < 1000 MeV/c^2$) with $|t'| < 1.0 (GeV/c)^2$. Only the largest momentum $\pi^+\pi^-$ pair in each event is included. There is a broad contribution centered at $10 GeV/c$ with a hard component beyond $16 GeV/c$; this supports the conclusion, in (c) above, that the ρ^0's are produced both diffractively and in $\rho'(1600)$ decay. Those arising from $\rho'(1600)$ decay are shown by curve B where the mass of the four pions is less that 2400 MeV/c. An estimate from this distribution of the nondiffractive background above 16 GeV/c yields $(20 \pm 5)\%$.

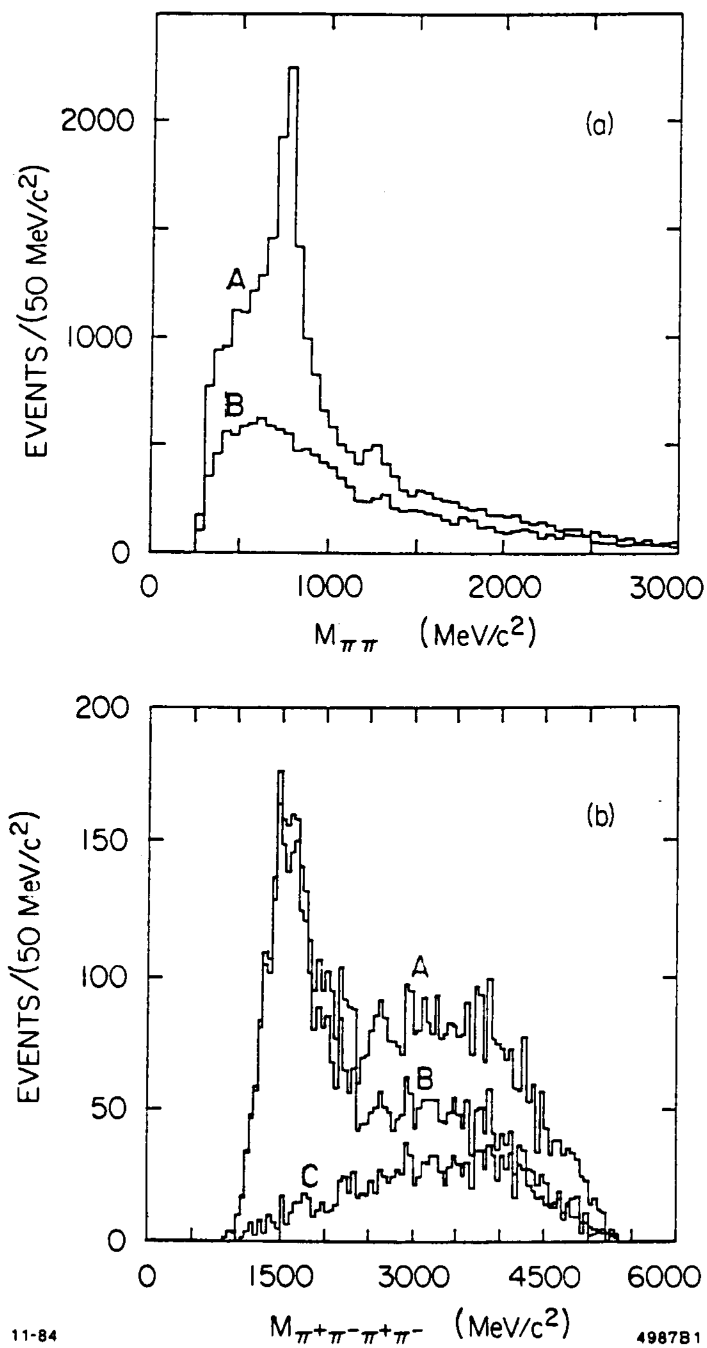

Figure 6.1: (a) The $\pi\pi$ mass distribution for 6468 events of the reaction $\gamma p \rightarrow p\pi^+\pi^+\pi^-\pi^-$. A is $\pi^+\pi^-$ and B is $\pi^\pm\pi^\pm$. (b) The 4π mass distribution for the reaction. See text for details.

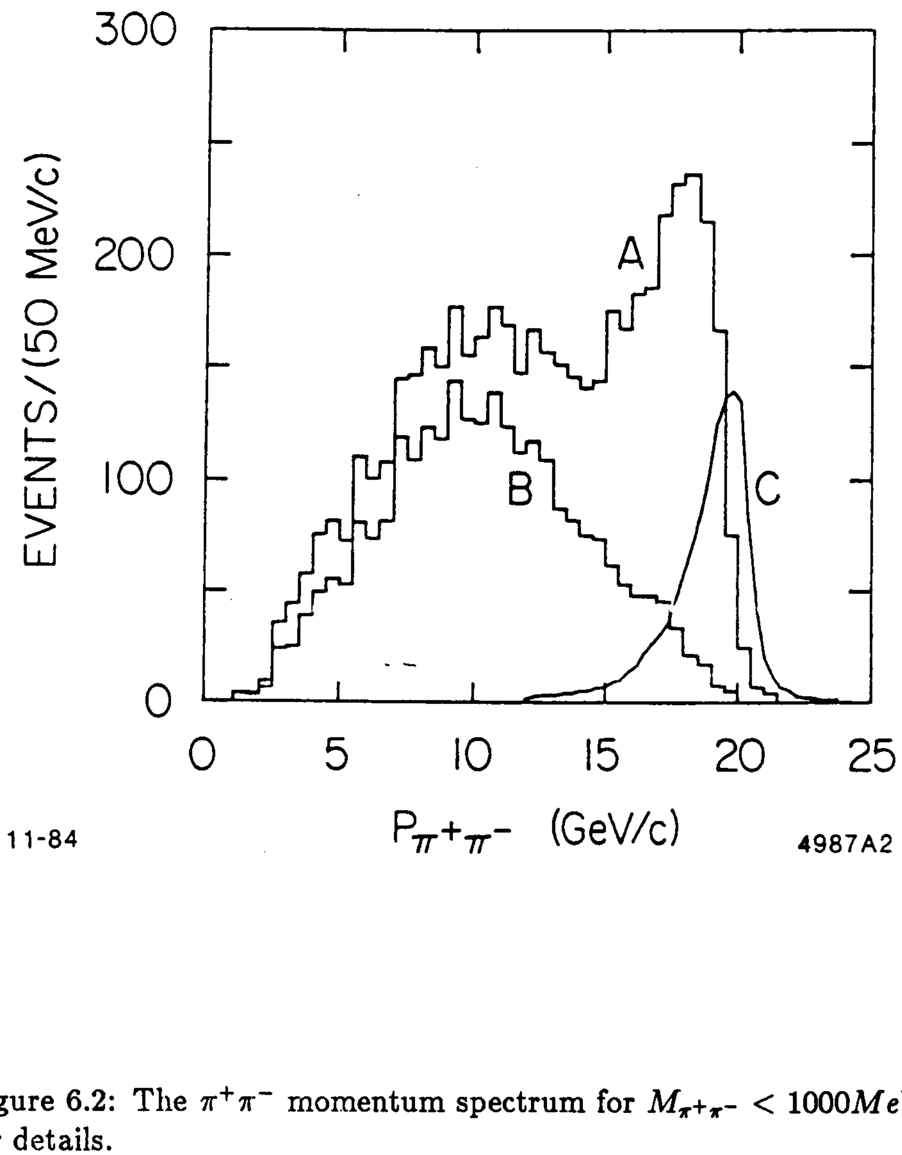

Figure 6.2: The $\pi^+\pi^-$ momentum spectrum for $M_{\pi^+\pi^-} < 1000 MeV/c^2$. See text for details.

(e) The momentum spectrum shape for ρ^0's produced elastically at the same incident gamma energy in the reaction $\gamma p \rightarrow p\pi^+\pi^-$ is shown in histogram C in Fig. 6.2 where there is a striking similarity with the hard component of histogram A, although histogram A is shifted to lower momenta by the more restrictive phase space resulting from the massive recoiling baryon system.

(f) Finally, selecting only those events containing $\pi^+\pi^-$ pairs having momentum greater than 16 GeV/c gives the mass spectrum shown in Fig. 6.3(a) which is clearly dominated by ρ^0 production and displays the mass-skewing exhibited in the quasieleastic reaction $\gamma p \rightarrow \rho^0 p$ shown in Fig. 6.3(b).

This selection of events with $\pi^+\pi^-$ pairs having a momentum in excess of 16 GeV/c produces a sample of diffractively produced ρ^0's from the reaction $\gamma p \rightarrow p\pi^+\pi^-\pi^+\pi^-$, which is free from $\rho'(1600)$ feedthrough. The $\pi^+\pi^-$ mass distribution has been fitted by a curve representing the Sõding model [46] of the form

$$\frac{d\sigma}{dm} = (f_{\rho D} + f_{\rho ND})\sigma_\rho(m) + f_I I(m) + f_D D(m) + f_B B(m). \tag{6.2}$$

The four terms which contribute to this expression have the following origin:

(a) The Breit-Wigner term representing ρ production, both diffractive and nondiffractive:

$$\sigma_\rho(m) = \frac{m}{q}\frac{m_\rho \Gamma_\rho(m)}{(m_\rho^2 - m^2)^2 + m_\rho^2 + m_\rho^2\Gamma^2(m)}. \tag{6.3}$$

(b) the Drell amplitude, which represents the nonresonant $\pi^+\pi^-$ production from the photon:

$$D(m) = \frac{(m^2 - m_\rho^2)^2}{(m_\rho^2 m^2)^2 + m_\rho^2 + m_\rho^2\Gamma^2(m)}. \tag{6.4}$$

(c) A term representing the interference of the diffractive ρ amplitude with the Drell amplitude:

$$I(m) = \frac{m^2 - m_\rho^2}{(m_\rho^2 m^2)^2 + m_\rho^2 + m_\rho^2\Gamma^2(m)}. \tag{6.5}$$

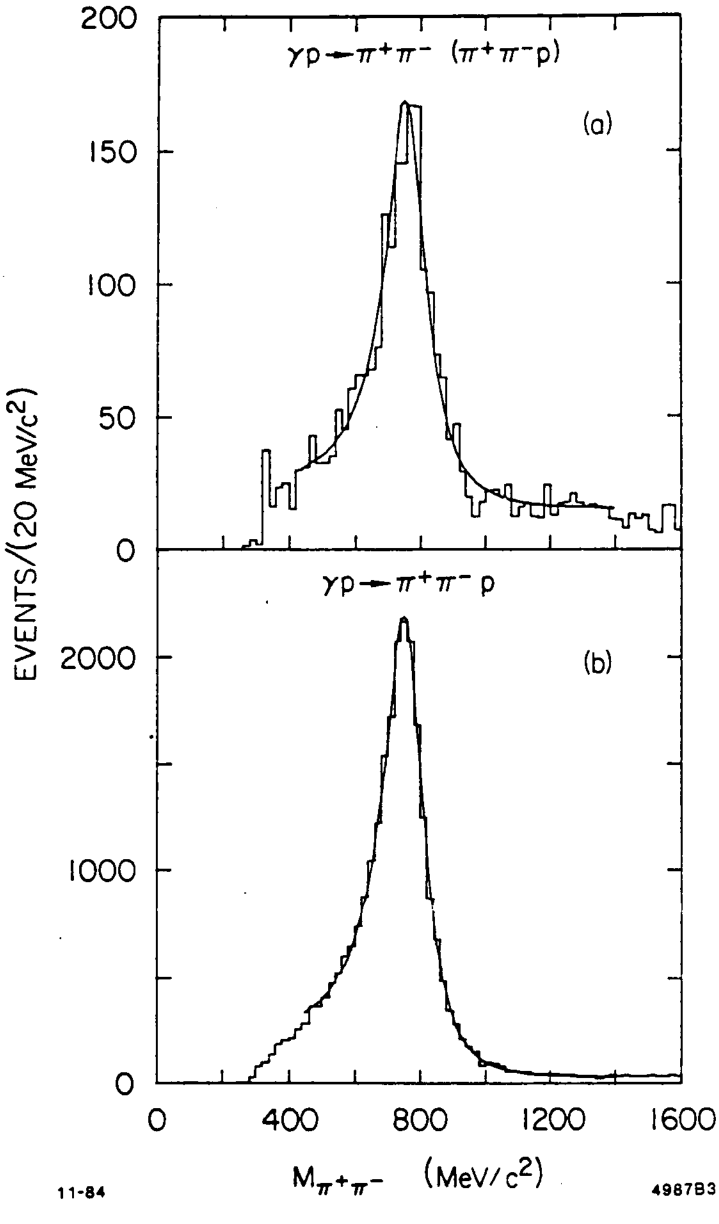

Figure 6.3: (a) The $\pi^+\pi^-$ mass distribution for the fast pairs. The fit is to the SÖding model (see text). (b) Söding model fit to the $\pi^+\pi^-$ distribution for the reaction $\gamma p \rightarrow p\rho^0$ at $20 GeV/c$.

(d) A polynomial nonresonant background:

$$B(m) = (m - 2m_\pi) + b(m - 2m_\pi) + b(m - 2m_\pi)^2 + c(m - 2m_\pi)^3, \qquad (6.6)$$

where b and c are paramenter of the fit.

The parameters $f_{\rho D}, f_{\rho ND}, f_D, f_I$, and f_B represent the strengths of the following terms: the diffractive ρ^0, the nondiffractive ρ^0, the Drell mechanism, and Drell-ρ interference, and the nonresonant background. A fit to the quasielastic distribution shown in Fig. 6.3(b) was done with $f_{\rho ND}$ and f_B set to zero. The relative strengths of f_D, f_I and $f_{\rho D}$ were then fixed in the inelastic fit. The integrated contribution from $f_{\rho ND}$ and f_B below 1000 MeV/c^2 was contrained to 20% as suggested earlier from Fig. 6.2. In the above,

$$\Gamma_\rho(m) = \Gamma_0[q(m)/q(m_\rho)]^3 \frac{\rho(m)}{\rho(m_\rho)}, \qquad (6.7)$$

$$\rho(m) = [q^2(m) + q^2(m_\rho)]^{-1}, \qquad (6.8)$$

where q is the pion momentum in the center of mass of the dipion system and m_ρ and Γ_0 are the ρ^0 mass and width ($769 \pm 3 MeV/c^2$ and $154 \pm 5 MeV/c^2$, respectively). The ρ^0 mass and width were allowed to vary in the final fit, the effects of which were included in the χ^2 with the above cited errors.

The Breit-Wigner term is symmetric around the position of the ρ mass; asymmetry about the ρ pole is produced by the interference term. Skewness in the mass spectrum is therefore evidence for a departure from pure ρ production. Fractions of each process present have been fitted to the mass spectrum using a minimum χ^2 method; the full form shown above gives a χ^2 of 75 for 42 degrees of freedom compared to a value of 1088 if only the Breit-Wigner term is allowed to contribute.

In order to isolate the reaction $\gamma p \rightarrow \rho^0(p\pi^+\pi^-)$ we select only those events from Fig. 6.3 with $M_{\pi\pi} < 1000 MeV/c^2$. Figure 6.4(a) shows the $p\pi^+\pi^-$

mass distribution for the pions opposite the selected $\pi\pi$ systems and compares this distribution with that of the diffractive reaction [47] $\pi^{\pm}p \rightarrow \pi^{\pm}(p\pi^{+}\pi-)$ at 14 GeV/c. If we are indeed observing a diffractive reaction we would expect to be able to relate it to the pion-induced diffraction through the equation

$$\sigma_{\gamma p \rightarrow \rho N^*} = \frac{\alpha}{2} \left(\frac{f_\rho^2}{4\pi} \right)^{-1} (\sigma_{\pi^+ p \rightarrow \pi^+ N^*} + \sigma_{\pi^- p \rightarrow \pi^- N^*}), \tag{6.9}$$

where$f_\rho^2/4\pi = 2.18$, determined by comparing quasielastic $\gamma p \rightarrow \rho^0 p$ to elastic $\pi^{\pm}p$ scattering [3]. Figure 6.4(a) shows a comparison of our data with such a renormalization of the π-induced diffraction. The agreement is very good in the relevant region ($M_{p\pi^+\pi^-} < 2000 MeV/c^2$). Both distributions show similar features, with the photoproduction being about 10% less. The diffractive nature is further supported by observing the near equality of our measured cross section of $0.90 \pm 0.1 \mu b$ with the value reported [48] for $\gamma p \rightarrow \rho^0 \Delta^{++} \pi^-$ at 9.3 GeV of $1.0 \pm 0.3 \mu b$. Figure 6.4(b) shows the $p\pi^+$ mass distribution from the $p\pi^+\pi^-$ system. The $p\pi^+\pi^-$ system is clearly cominated by $\Delta^{++}\pi^-$. We have also observed a small component of $\Delta^0\pi^+$, consistent with the expected $\frac{1}{9}$ contribution for the decay of an N^* isotopic spin $\frac{1}{2}$. The t' distribution for the reaction has a slope which depends on the mass of $p\pi^+\pi^-$ system as shown in Table 6.1, with the largest slopes occurring for the smaller masses. This is the same dependence as in π-induced diffraction and similar to the varioation observed with $\pi\pi$ mass in elastic $\pi\pi$ photoproduction.

To summarize, we have observed diffractive inelastic ρ^0 production as evidenced by the peripheral nature, the ρ-mass skewing, the similarity and scaling of the $p\pi^+\pi^-$ mass distribution to π- induced diffraction, and the isotopic spin-$\frac{1}{2}$ behavior of the $\Delta\pi$ branching ratios.

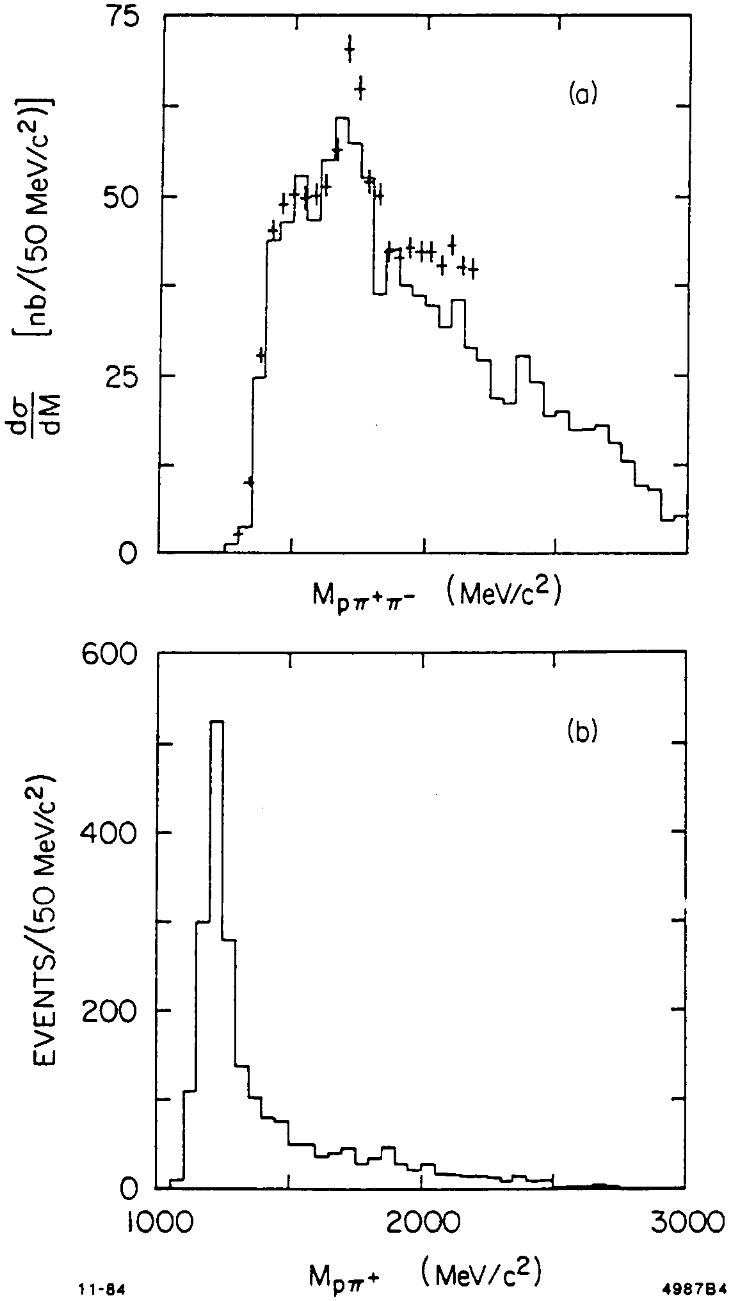

Figure 6.4: (a) The $p\pi\pi$ mass distribution. The data points are from the reaction $\pi^{\pm}p \rightarrow \pi^{+}_{fast}(p\pi^{+}\pi^{-})$. (b) The $p\pi^{+}$ mass distribution for the events in (a).

Table 6.1: The slope b of the differential cross section ($dN/dt' = Ae^{bt'}$) as a function of the ($p\pi^+\pi^-$) mass.

$M_{p\pi^+\pi^-}(MeV/c^2)$	$b[(GeV/c)^{-2}]$
< 1500	8.75 ± 0.49
$1500 - 1600$	10.66 ± 0.60
$1600 - 1800$	5.08 ± 0.30
$1800 - 2100$	5.53 ± 0.31
> 2100	3.21 ± 0.23

6.4 The test of s-channel helicity conservation

To test SCHC of the ρ^0 we have examined the distributions of conventional helicity angles [10]. Figure 6.5 illustrates these angles. The polar angle of the π^+ in the ρ-rest frame relative to the ρ direction of flight is denoted by θ. The difference between the azimuthal angles (Φ, the angle between the photon polarization vector and the production plane in the center-of-mass system, and ϕ, the azimuthal angle of the ρ decay in the ρ-rest frame measured as the angle between the decay plane and the production plane) is denoted by $\psi(\psi = \phi - \Phi)$. If s-channel helicity is conserved the ρ will have helicity ± 1 and

$$W(\cos\theta, \psi) = (\frac{3}{8\pi}\sin^2\theta)(1 + P_\gamma \cos 2\psi). \tag{6.10}$$

P_γ=0.52 is the calculated degree of photon polarization, verified by the elastic ρ measurements [49].

Figure 6.6 presents the distributions for $\cos\theta$ and ψ for this reaction (22% of the experiment was excluded from the angular distrubution analysis [49] since the ultraviolet laser photons had a deteriorated polarization) with the further restriction, $720 < M_{\pi\pi} < 820 MeV/c^2$ (along with the previous cuts $P_{\pi^+\pi^-} > 16 GeV/c, M_{p\pi^+\pi^-} < 2200 MeV/c^2$). The solid curves give the prediction for SCHC and include a contribution from 20% background which is assumed to be isotropic,

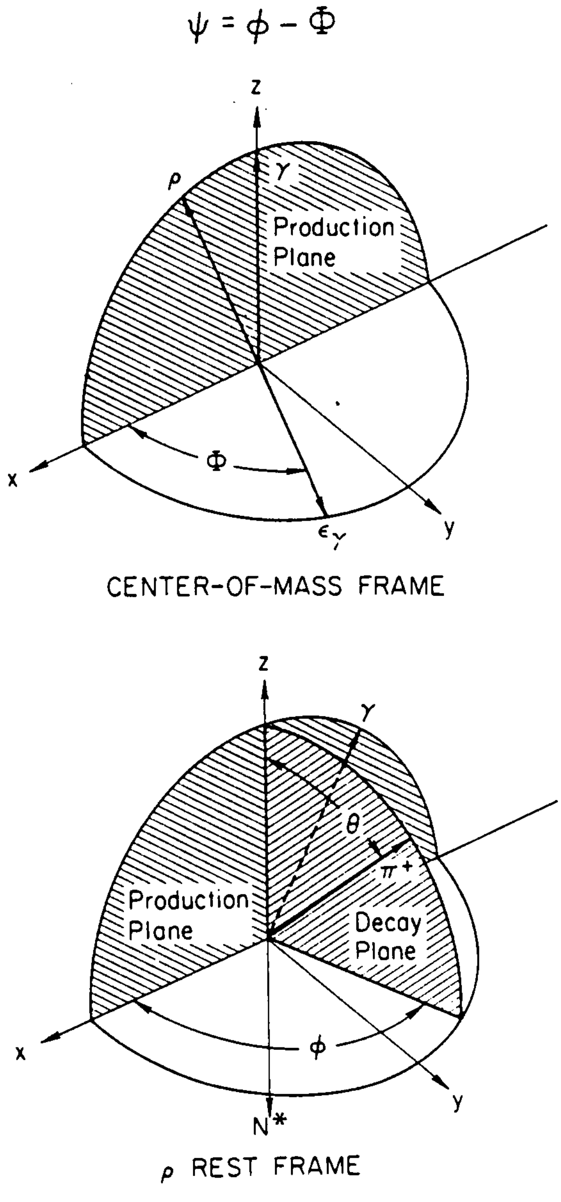

Figure 6.5: The angles used in the study of ρ^0 decay.

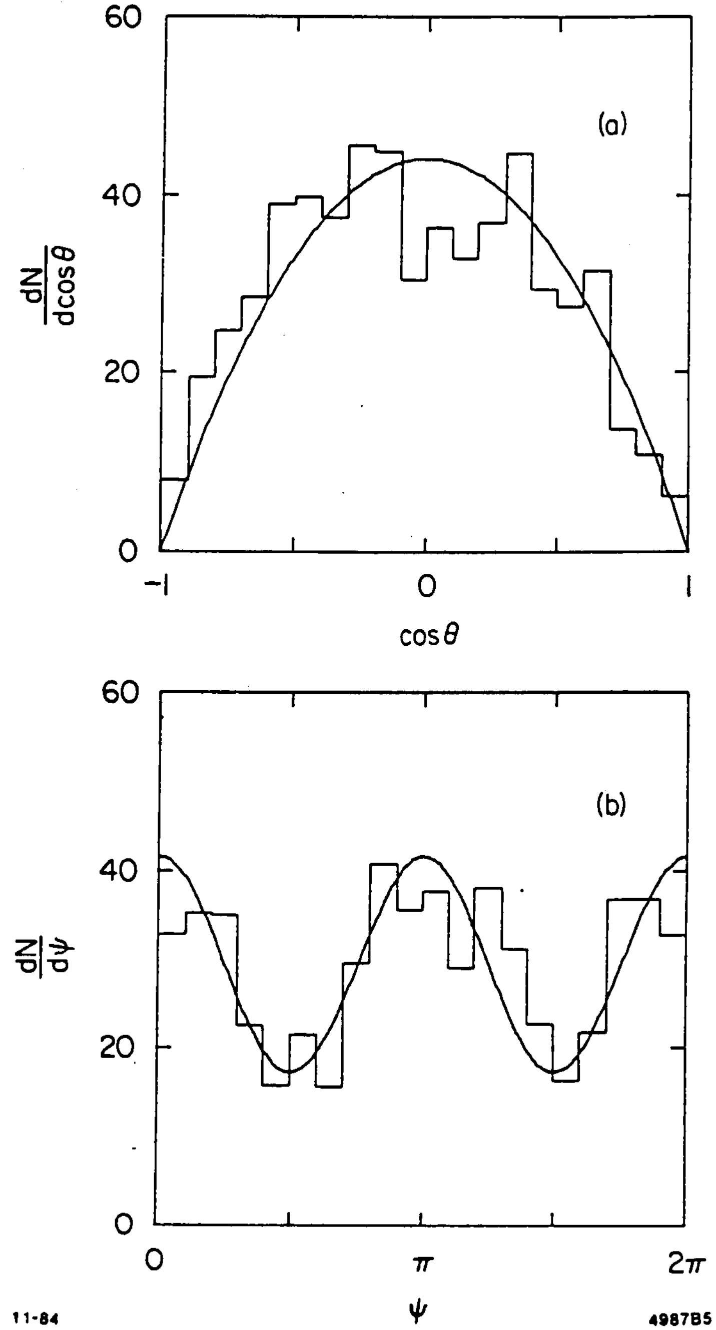

Figure 6.6: The decay-angular distributions of the $\pi^+\pi^-$ system in the helicity frame for the mass range $720 < M_{\pi^+\pi^-} < 820 MeV/c^2$.

$W(\cos\theta, \psi) = 1/4\pi$. This angular ditribution for the background was found to be consistent with that of the $\pi^+\pi^-$ pairs in the region $P_{\pi^+\pi^-} \sim 10 GeV/c$. There is good agreement with the expected SCHC behavior indicating that this reaction is dominated by SCHC.

To assess quantitatively the degree of s-channel helicity conservation for inelastic ρ^0 production, the density matrix elements of the ρ^0 decay in the helicity rest frame have been determined. The decay angular distribution can be expressed in terms of nine independent measurable spin-density-matrix elements ρ^{α}_{ik}

$$\begin{aligned} W(\cos\theta, \phi, \Phi) &= \frac{3}{4\pi}\{\frac{1}{2}(1-\rho^0_{00}) + \frac{1}{2}(3\rho^0_{00}-1)\cos^2\theta \\ &\quad -\sqrt{2}Re\rho^0_{10}\sin 2\theta\cos\phi - \rho^0_{1-1}\sin^2\theta\cos 2\phi \\ &\quad -P_\gamma\cos 2\Phi[\rho^1_{11}\sin^2\theta + \rho^1_{00}\cos^2\theta \\ &\qquad -\sqrt{2}Re\rho^1_{10}\sin 2\theta\cos\phi - \rho^1_{1-1}\sin^2\theta\cos 2\phi] \\ &\quad -P_\gamma\sin 2\Phi[\sqrt{2}Im\rho^2_{10}\sin 2\theta\sin\phi + Im\rho^2_{1-1}\sin^2\theta\sin 2\phi]\}. \end{aligned} \tag{6.11}$$

For transverse and linearly polarized photons, one expects, in the case of SCHC, that only two spin-density-matrix elements are nonzero

$$\rho^1_{1-1} = \frac{1}{2} \tag{6.12}$$

$$Im\rho^2_{1-1} = -\frac{1}{2}. \tag{6.13}$$

The values for two t' bins are shown in Table 6.2; these are from the angular distributions after removal of the 20% isotropic background. In general, the helicity flip density matrices remain small as t' increases, e.g., $\rho^0_{00} \sim 0$ for all t', and the nonflip terms are consistent with their expected values.

Table 6.2: The spin-density-matrix elements for the diffractive ρ^0 meson in the helicity reference frame.

	$0.0 < \lvert t' \rvert < 0.4 (GeV/c)^2$	$0.4 < \lvert t' \rvert < 1.0 (GeV/c)^2$
ρ^0_{00}	-0.01 ± 0.02	-0.01 ± 0.03
$Re\rho^0_{10}$	0.03 ± 0.02	-0.01 ± 0.05
ρ^0_{1-1}	-0.02 ± 0.03	-0.02 ± 0.06
ρ^1_{11}	0.05 ± 0.08	0.14 ± 0.19
ρ^1_{00}	0.04 ± 0.11	0.38 ± 0.18
$Re\rho^1_{10}$	0.10 ± 0.08	-0.10 ± 0.15
ρ^1_{1-1}	0.28 ± 0.11	0.61 ± 0.24
$Im\rho^2_{10}$	-0.05 ± 0.07	0.37 ± 0.17
$Im\rho^2_{1-1}$	-0.39 ± 0.12	-0.69 ± 0.24

CHAPTER 7

EXPERIMENTAL RESULTS

In this chapter we present the results from the E745 neutrino experiment. In the first section, we report on the observation of coherent diffractive production of the a_1^+ axial vector meson. In the second section, we report on a search for the charmed strange vector meson, the D_s^*, and present some upper limits on its diffractive cross section.

7.1 a_1^+ Results

Coherent production, a subgroup of diffractive production, is especially emphasized in the theoretical literature and in recent experimental work. In coherent interactions, the nucleus is nudged gently, and recoils as a unit without breakup, and with too little energy to be detected in the bubble chamber. These interactions exhibit a sharply falling exponential t distribution:

$$\frac{d\sigma}{dt} \sim e^{-b|t|}, \tag{7.1}$$

where t is the four momentum transfer to the nucleus, and b is a function of the size of the nucleus.

Recent experimental work includes inclusive coherent charged current interactions on neon, from two groups [50,51]. The exclusive coherent channels reported include:

- π^- and ρ^- production from antineutrinos on neon [52,53].
- $\pi^\pm$ production from (anti)neutrinos on freon [54].
- ρ^+ production from neutrinos on neon [55].

- π^0 production from neutral current interactions in several experiments [54,56],- and [57,58,59,60].

The following sections look at the coherent exclusive production of a_1^+ from neutrinos on freon in the reaction:

7.1.1 Cross Section

The cross section for coherent diffractive scattering derived earlier (Eq. 2.34):

$$\frac{d^3\sigma}{dt dQ^2 d\nu} = \frac{G^2}{2\pi^2 E_\nu^2 g_a^2}\left(\frac{m_a^2}{Q^2+m_a^2}\right)^2 \frac{Q^2\nu(1+\epsilon R)}{1-\epsilon}\frac{d\sigma_T}{dt}, \tag{7.2}$$

where:

- G is the weak coupling constant ($G = 1.166 \times 10^{-5} GeV^{-2}$).
- m_a is the a_1 mass ($m_a = 1.275\ GeV/c^2$).
- g_a is a coupling constant related to the leptonic decay width of the a_1:

$$\Gamma_{a_1 \to \mu\nu} = \frac{4\pi\alpha^2}{3}\frac{m_a}{g_a^2}. \tag{7.3}$$

  The previous constant f_a, which designates the coupling of the a_1 to the intermediate vector boson, is related to g_a by $f_a = \sqrt{2}m_a^2/g_a$. We will use the hypothesis from reference [5] that the leptonic decay width of the a_1 is equal to that of the ρ; this leads to $g_a^2/g_\rho^2 = m_a/m_\rho$. The value for g_ρ is taken from [23] as $g_\rho^2 = 2.0 \times 4\pi$.

- ϵ is the polarization of the intermediate vector boson and is shown to be (Eq. 2.33):

$$\epsilon = \frac{4E_\nu(E_\nu - \nu) - Q^2}{4E_\nu(E_\nu - \nu) + Q^2 + 2\nu^2}. \tag{7.4}$$

- R is the ratio of longitudinal $d\sigma_L/dt$ to transverse $d\sigma_T/dt$ cross section (Eq. 2.31). At $Q^2 = 0$, gauge invariance requires $R = 0$ [7]. Experimental evidence [61,62] indicates that our assumption of $R = 0$ is good at higher Q^2 also.

An approximation for $d\sigma_T/dt$ which follows from the optical theorem [5,50,56] is:

$$\frac{d\sigma_T}{dt} = \frac{A^2}{16\pi}\sigma_{tot}^2(a_1^+ N)e^{-b|t|}F_{abs}, \tag{7.5}$$

where:

- A is the atomic weight of the struck nucleus. The mixture of Freon in the bubble chamber contained Fluorine ($A = 19.00$), Carbon ($A = 12.01$), and Chlorine ($A = 35.45$), with the relative amounts; $F : C : Cl = 0.66 : 0.25 : 0.09$. All the calculations are done independently for each nuclear type and then averaged to get the final cross section.

- $\sigma_{tot}(a_1^+ N)$ is the total a_1^+ nucleon cross section. From the additive quark model [5], it is equal to: $\sigma_{tot}(\rho^+ N) = \sigma_{tot}(\pi^+ N) \simeq 26mb$.

- b is a parameter related to the nuclear radius, $b = r^2/3$. The nuclear radius is calculated from $r = r_0 A^{1/3}$, with $r_0 \simeq 1.1fm$. This gives, in units of $GeV^{-2}: b(F) = 74.0,\ b(C) = 54.5$ and $b(Cl) = 112.2$.

- F_{abs} takes into account secondary interactions inside the nucleus. We employ a simple model, with $F_{abs} = e^{-\langle x\rangle/\lambda}$ and $\langle x\rangle = \frac{3}{4}r$, being the average path length traversed in a homogeneous spherical nucleus. λ is the mean free path defined by $\lambda^{-1} = \sigma_{inel}\rho$, with ρ being the nuclear density ($\rho = A/\frac{4}{3}\pi r^3$). The value of $\sigma_{inel}(a_1^+ N) \simeq 20mb$ used, comes from the ρ case [5]. For the elements in Freon: $F_{abs}(F) = 0.45, F_{abs}(C) = 0.51$, and $F_{abs}(Cl) = 0.38$.

Changing variables in terms of $y = \nu/E$ and substituting the constants gives, in units of cm^2/GeV^4:

$$\frac{d^3\sigma}{dtdQ^2dy} = B \times 10^{-38} \left(\frac{m_a^2}{Q^2 + m_a^2}\right)^2 \frac{Q^2 y}{1-\epsilon} e^{-bt}, \tag{7.6}$$

where B is an element dependent constant: $B(F) = 93, B(C) = 42$, and $B(Cl) = 273$. This will be compared to the known neutrino cross section per nucleon [23]:

$$\frac{\sigma}{E_\nu} = 0.67 \times 10^{-38} cm^2/GeV. \tag{7.7}$$

A full comparison of these equations to our data will be effected in subsequent sections.

The expected angular distribution is derived in section 2.3 and given in Eq. 2.109. The assumption, $R = 0$, eliminates most of the terms, leaving only (Eq. 2.110):

$$W(\theta, \phi, \Phi) = 2 - \sin^2\theta(1 + \epsilon\cos 2\psi) \tag{7.8}$$

where $\epsilon \simeq 1$ for most of the events in our sample. Φ is the angle between the lepton plane (defined by the neutrino and muon) and the hadron plane (defined by the momentum transfer and the vector meson). θ and ϕ are the polar and azimuthal angles of the normal, to the decay plane in the a_1 rest system. ψ is defined as $\phi - \Phi$.

7.1.2 a_1 signal

The event sample selected consisted of four prong events with two positive and two negative tracks. One of the negative tracks was required to be an identified muon. Only events without an associated vee or gamma were considered. The $\pi^+\pi^+\pi^-$ mass of the 89 selected events is shown in Fig. 7.1, and shows an excess of events in the a_1 mass region. The a_1 signal stands out above the background curve generated with the Lund Monte-Carlo. Further verification of this follows from

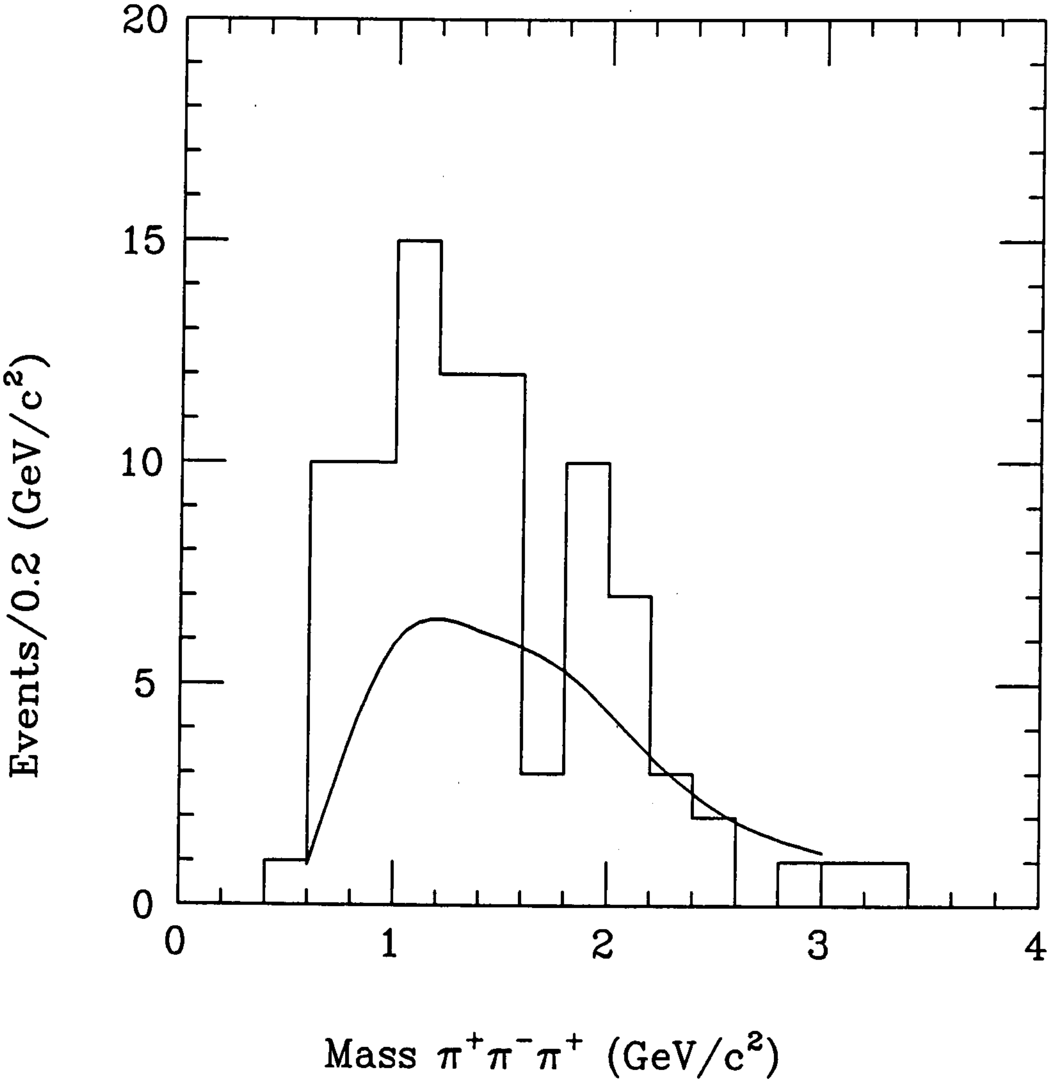

Figure 7.1: Mass of $\pi^+\pi^+\pi^-$. The superposed background curve is from the Lund Monte-Carlo.

the $\pi^+\pi^-$ mass spectrum (two combinations from each event) in Fig. 7.2, where a ρ^0 signal is present. Fig. 7.3 shows the $\rho_0\pi^+$ mass spectrum ($0.5 \leq m_\rho \leq 1.0GeV$). This eliminates much of the background present in Fig. 7.1. The full sample of 60 $a_1's$ is selected from this plot. This signal is fit to a Breit-Wigner curve and a quadratic background to give an a_1 mass of $1.20 \pm 0.02GeV/c^2$.

The dominant feature expected from the coherent a_1 signal is a steep exponential dependence on t. The next step in isolating the coherent a_1 signal is to calculate t.

7.1.3 The t calculation

To calculate t for the coherent case, the assumption is made that an entire nucleus in the Freon molecule interacts coherently. In four vector notation:

$$t = (P - P')^2 = (M_{Fr} - E_{Fr})^2 - (0 - \vec{p}_{Fr})^2 = T_{Fr}^2 - |\vec{p}_{Fr}|^2, \tag{7.9}$$

where T_{Fr} is the kinetic energy of the nucleus. Under the assumption that no neutral particles are present, the transverse momentum of the Freon is known, since it is the missing transverse momentum in the event $p_T^2 = |p_{Fr}^T|^2$. To find the longitudinal momentum, we employ conservation of energy and longitudinal momentum for the interaction:

$$\begin{aligned} E_\nu + M_{Fr} &= E_\mu + E_a + E_{Fr} & (7.10)\\ p_\nu &= p_\mu^L + p_a^L + p_{Fr}^L, & (7.11) \end{aligned}$$

subtracting Equation 7.11 from Equation 7.10 and using $D = E_\mu - p_\mu^L + E_a - p_a^L$, one gets $p_{Fr}^L = D + T_{Fr}$, and after substitution in the expression for t:

$$-t = |t| = p_T^2 + D^2 + 2DT_{Fr}. \tag{7.12}$$

The last term is small, but can be calculated by using:

$$T_{Fr} = E_{Fr} - M_{Fr} = [\vec{p}_{Fr}^{\,2} + M_{Fr}^2]^{1/2} - M_{Fr}, \tag{7.13}$$

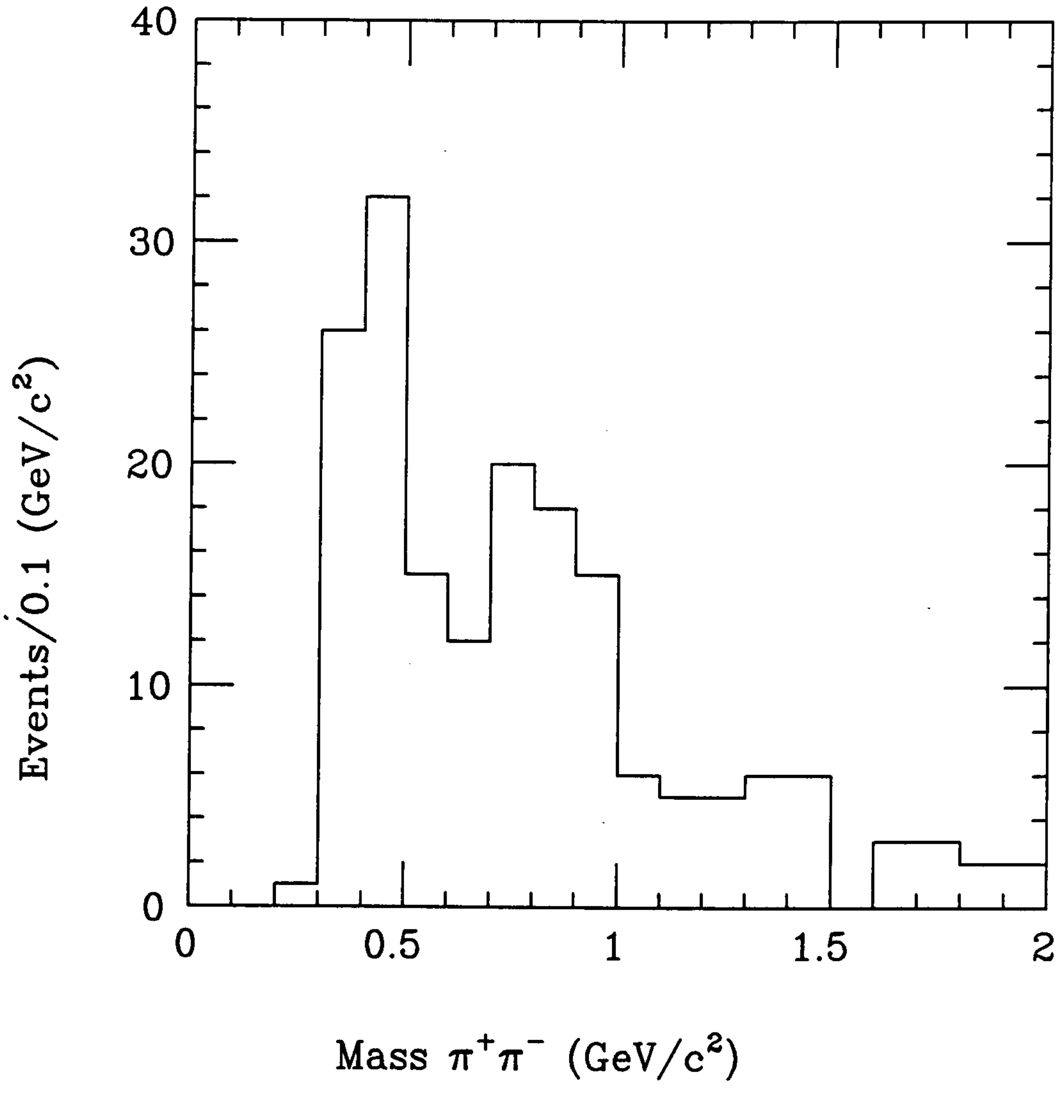

Figure 7.2: Mass of $\pi^+\pi^-$ combinations.

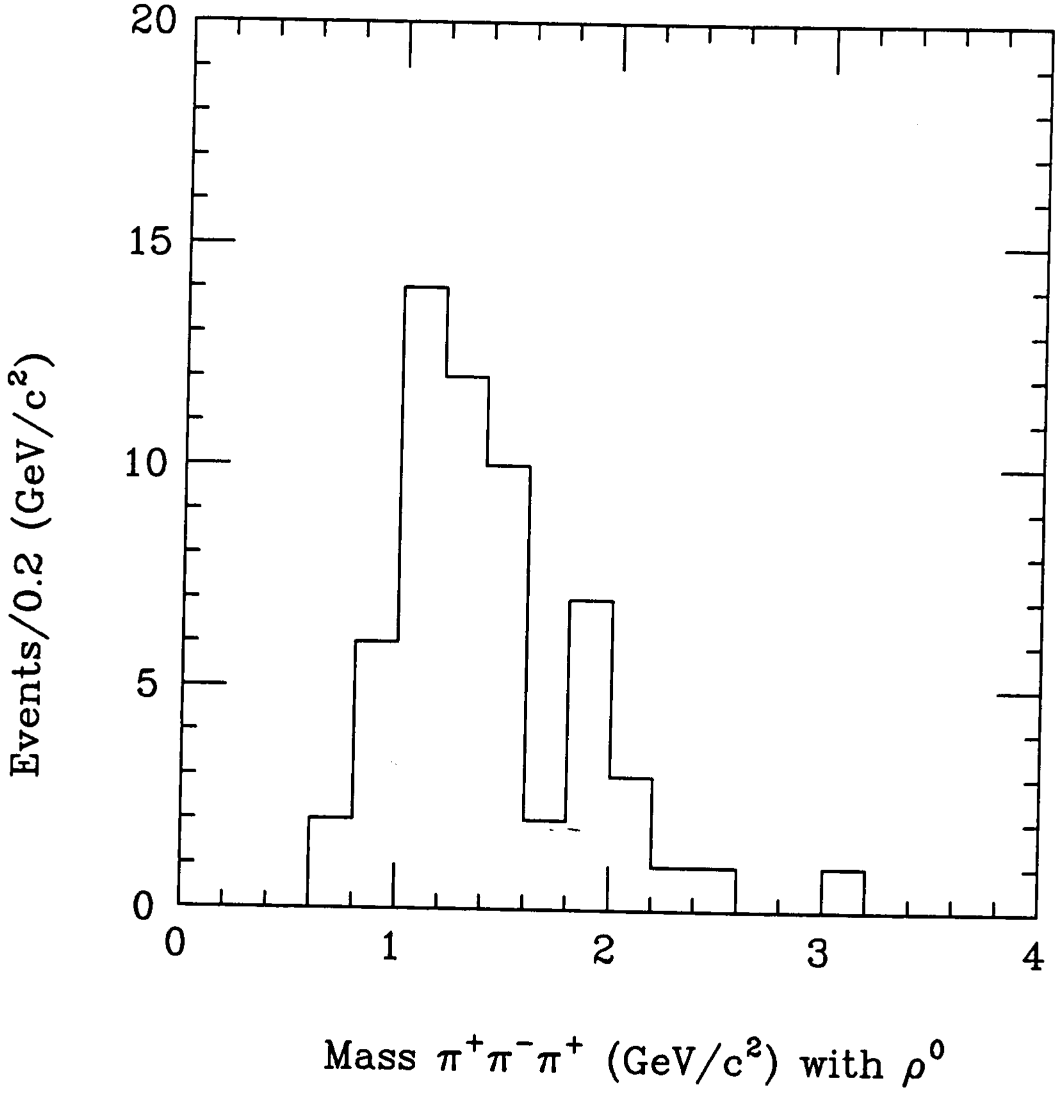

Figure 7.3: Mass of $\pi^+\pi^+\pi^-$ after ρ^0 mass cut.

and eliminating p^L_{Fr}, as above. The final result is, (dropping the absolute value sign from here on):

$$t = \frac{p_T^2 + D^2}{1 - D/M_{Fr}}. \tag{7.14}$$

The t distributions for the events with a proton, and without one, are plotted in Fig. 7.4(a),(b). The events with an identified proton are not expected to contribute to the coherent signal, since the existence of the proton indicates that the nucleus has been disturbed in the reaction, but they are useful as a background signal.

7.1.4 The Coherent Sample

Among the events with no identified proton, 8 events have $t < 0.4$ $(GeV/c)^2$. These are interpreted as the coherent signal, since none of the events with an identified proton has $t < 0.4(GeV/c)^2$. The error in t vs. t is presented in Fig. 7.4(c). t is bounded from below so any error on the small t values will tend to skew them to larger values. Distributions of Q^2 and of the hadronic energy are presented in Fig. 7.5 and Fig. 7.6. In all figures, part (a) presents the coherent sample events with $t < 0.4(GeV/c)^2$ and no stub, part (b) presents the $t > 0.4(GeV/c)^2$ events with no stub, and part (c) presents the events with an identified proton. The differences in the distributions strengthen our hypothesis that the coherent sample arises from a different reaction mechanism.

7.1.5 Background Estimation

The background events in the $t < 0.4(GeV/c)^2$ region arise from two different sources [55]:

1. Incoherent diffractive events from nucleons that also follow an exponential distribution, but with a lower b value. These events will give less of a contribution in the low t region than the coherent events.

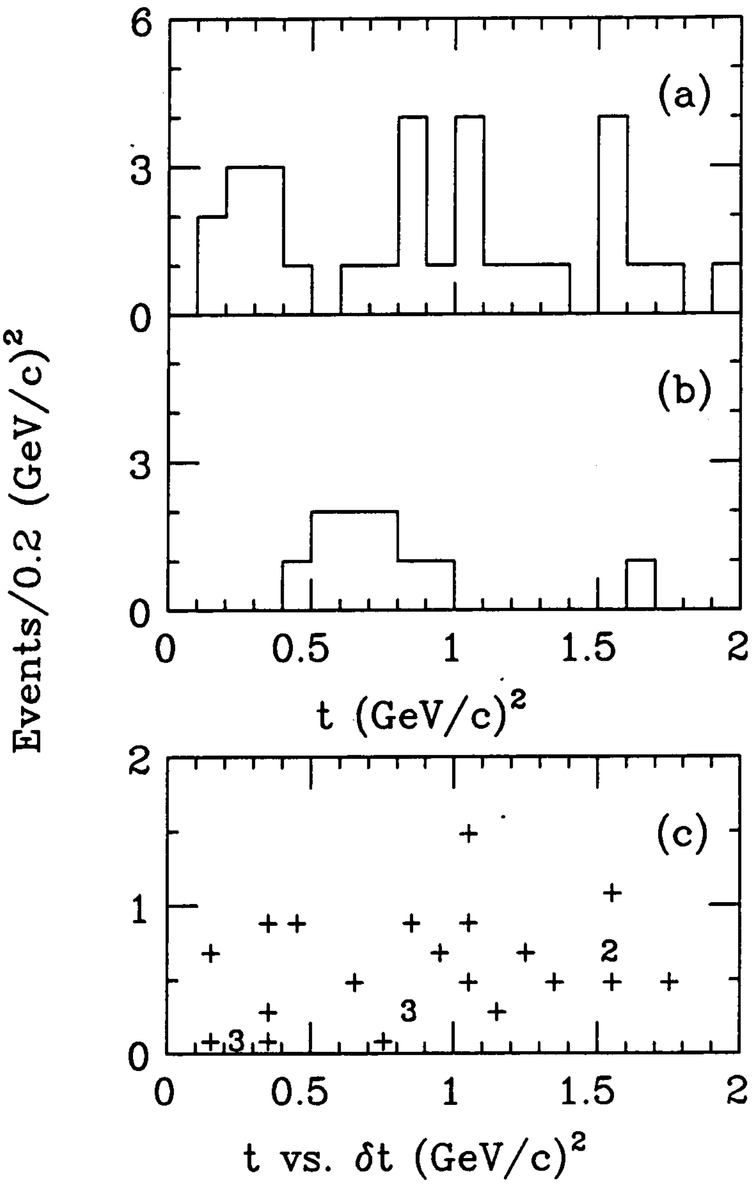

Figure 7.4: t distribution for a_1 events (a)no stub (b)with stub (c)t vs. error in t.

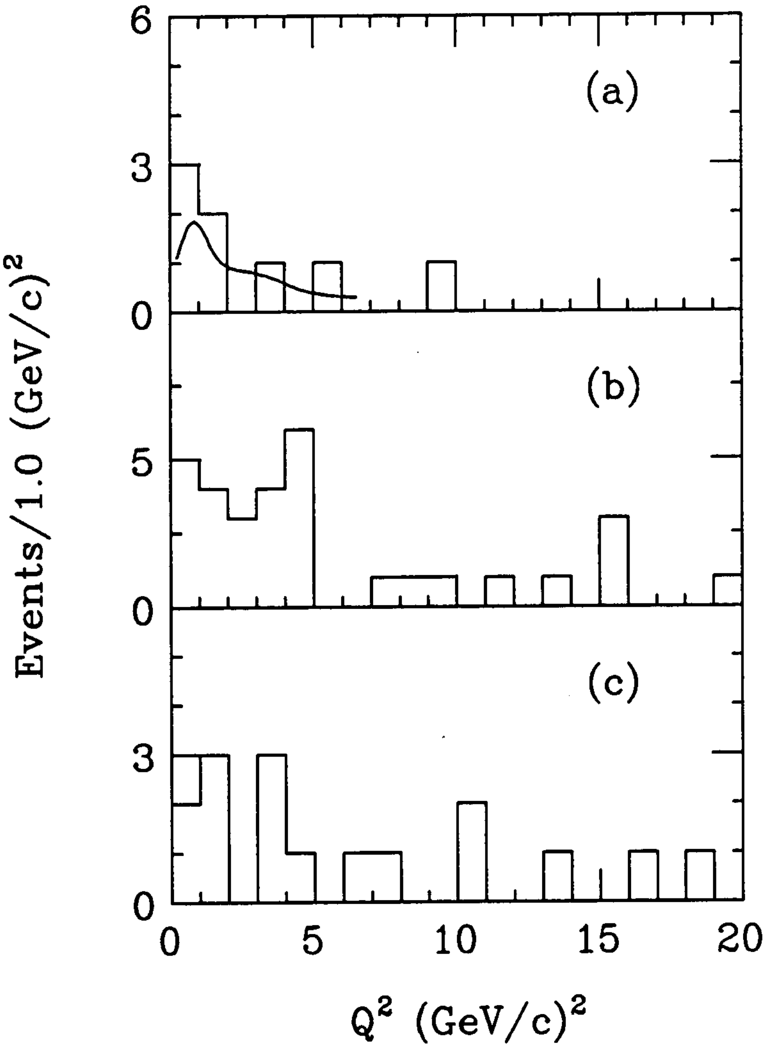

Figure 7.5: Q^2 distribution for a_1 events (a)no stub and $t < 0.4(Gev/c)^2$ (b)no stub and $t > 0.4(GeV/c)^2$ (c)all stub events.

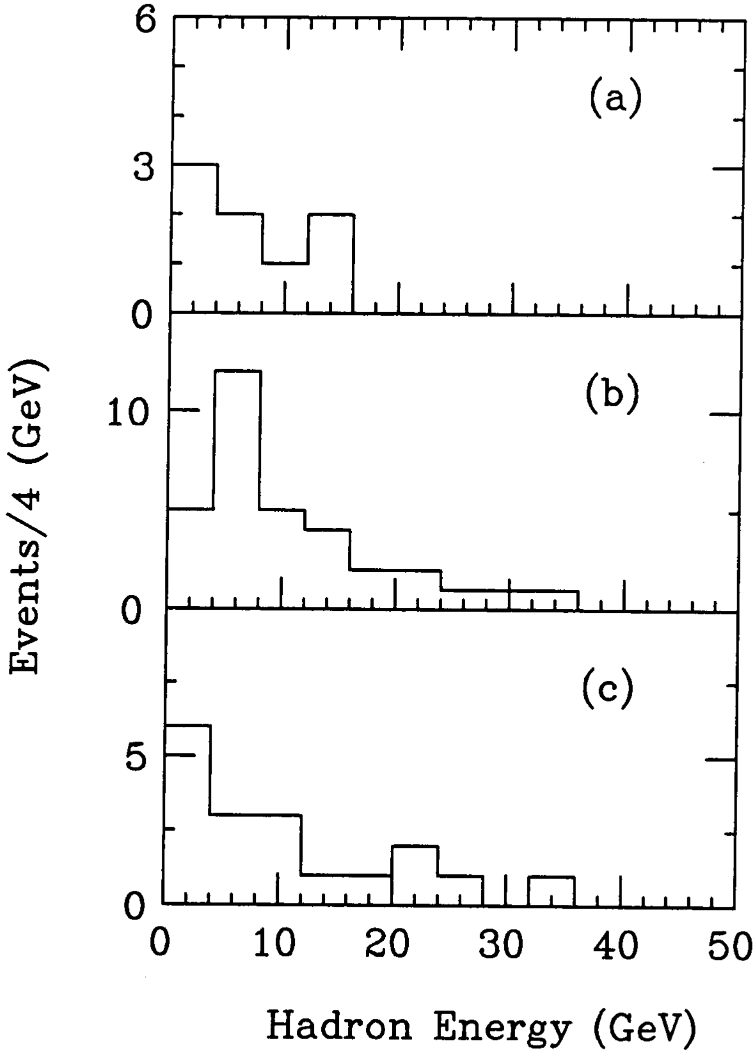

Figure 7.6: Hadronic energy distribution for a_1 events (a)no stub and $t < 0.4(GeV/c)^2$ (b)no stub and $t > 0.4(GeV/c)^2$ (c)all stub events.

2. Misidentified events with missing neutrals or stubs too short to be detected, whose calculated t value only approximate.

To obtain a background estimate, we compare the events with $t > 0.4(GeV/c)^2$ and no identified proton (or no stub events), where no coherent signal is expected, to two different sources:

1. The t distribution of events with identified proton stubs should indicate the kind of background expected from both of the above sources. Since very short stubs can't be seen by the scanners, a calculation utilizing only this source would be an underestimate. In addition, the unseen-stub events will appear in the no-stub plot causing an excess of events there. In [28], the estimate was that a third of the stub events are too short to be detected, and this will be used to partially correct the calculation. Since no events appear in the $t < 0.4(GeV/c)^2$ region, the best estimate of background is zero. The error in this quantity is calculated from the events with t between $0.4 - 1.0(GeV/c)^2$, assuming one of the missed stub events appears in the low t region to give an error of 0.5.

2. The Lund Monte-Carlo gives a prediction for the t distribution of the incoherent, no-stub events. It takes into account the measurement errors, acceptance of the bubble chamber and the missed neutrals. As mentioned previously, there is an excess of events in the $t > 0.4(GeV/c)^2$ region of the no-stub events, so this will give an overestimate which will be partially corrected for as above. From the Monte Carlo, about 20% of the events appear with a $t < 0.4(GeV/c)^2$, and about 30% are with t between $0.4-1.0(GeV/c)^2$. Comparing to the data in those regions gives a background of 2.7 ± 1.3 events in the $t < 0.4(GeV/c)^2$ region.

Since neither estimate is, a priori, superior to the other, we take their average value, 1.3 ± 0.7 which leaves a net signal of 6.7 ± 2.9 events.

7.1.6 Acceptance Corrections

To correct for experimental acceptance, the following factors are taken into account:

1. The branching ratio for the studied decay $a_1^+ \rightarrow \pi^+\pi^+\pi^-$ is 0.5 (from isospin consideration, the other half decay via $a_1^+ \rightarrow \pi^+\pi^0\pi^0$. These events have a small acceptance in the bubble chamber and do not appear in the 4-prong event sample).

2. The probability that the measured t with errors be within the cut when the real t is less than $0.4(GeV/c)^2$ is 0.68 (from the Lund Monte-Carlo).

3. The measuring efficiency for four prong events was 0.93 ± 0.07 [17].

This gives a signal of 21.2 ± 9.1. The 1792 events used, corrected for an overall measuring efficiency of 90.8 ± 3.6, give an a_1 production rate of $(1.1 \pm 0.47)\%$.

7.1.7 Comparison to Theory

The theoretical predictions of the model for our experiment were extracted by using the Monte-Carlo events to simulate the distributions of the differnt kinematical quantities. The Monte-Carlo prediction for the total coherent a_1 rate is 0.96%, which is in good agreement with the experimental value. The coherent signal gives an a_1 mass of $1.28 \pm 0.3 GeV/c^2$; other kinematical parameters are presented in Table 7.1 with their theoretical predictions. The theoretical Q^2 distribution is superposed on the data in Fig. 7.5. Despite the limited statistics, we can see that the model predictions are in general agreement with the data. The

Table 7.1: Mean values of a_1 kinematical parameters

Parameter	Data	Model
$E_\nu(GeV)$	70 ± 54	88
$E_\mu(GeV)$	63 ± 53	72
$\nu(GeV)$	6.9 ± 4.8	16
$Q^2(GeV^2)$	2.8 ± 2.8	4.5
$W^2(GeV^2)$	11 ± 7.5	26
x	0.21 ± 0.14	0.22
y	0.18 ± 0.18	0.19

major discrepency seems to be softer distributions in ν, Q^2 and W^2; this can possibly be related to the Monte-Carlo treatment of errors in high momentum muons. On the other hand, references [55,52,53] see a similar, effect so this slight effect could indicate an inaccuracy in the model itself. The angular distributions for the no stub a_1 data are presented in Fig. 7.7, with the theoretical prediction of $R = 0$ superposed. A maximum likelihood calculation indicated that $R = 0$ is consistent with the data but the errors were too large to make a definite prediction.

Until now, we have been assuming the model of Gaillard *et al.*[5], since it gives the best fit to the data. As mentioned earlier, they assume that the leptonic decay width of the a_1 is equal to that of the ρ, which gives a prediction for the ratio of the $a_1 - W$ coupling constant as $f_a^2/f_\rho^2 = 4.54$. Chen *et al.*[7] assume that the coupling of the a_1 to the W^+ is equal to that of the ρ leading to $f_a^2/f_\rho^2 = 1$. Our data indicates $f_a^2/f_\rho^2 = 5.2 \pm 2.2$, which tends to favor the the Gaillard model.

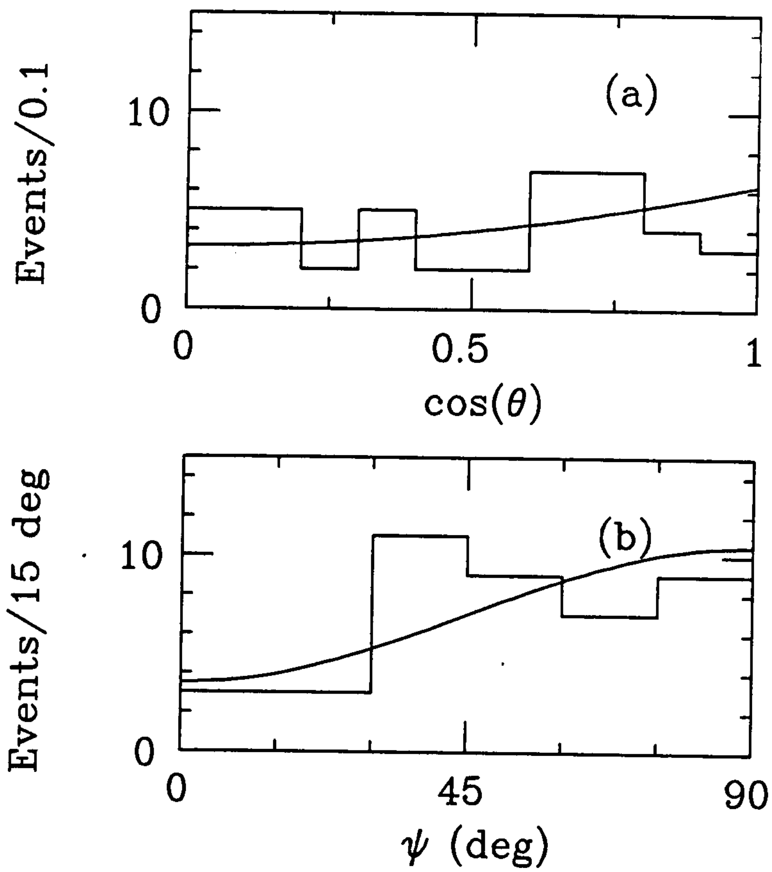

Figure 7.7: Angular distributions of the coherent a_1 decay (a) $\cos\theta$ and (b)ψ. The angle range has been folded because of the limited statistics.

7.2 Charm Strange Meson Results

The Vector Dominance Model predicts the production of mesons other than the ρ and a_1. References [5,7] predict the production of the K^*, D^*, and the D_s^* in this process. The charmed strange vector meson D_s^*, is of special theoretical and experimental interest. Theoretically according to the GIM mechanism [63], we define the weak doublets

$$\begin{pmatrix} u \\ d_c \end{pmatrix}, \begin{pmatrix} c \\ s_c \end{pmatrix}, \tag{7.15}$$

where d_c is the Cabibbo rotated down quark $d_c = d\cos\theta_c + s\sin\theta_c$, and similarly for the rotated strange quark $s_c = s\cos\theta_c - d\sin\theta_c$. This possibly implies a high cross section, since the W^+ can couple strongly to the D_s quark combination of $c\bar{s}$, verses the other charm and strange couplings that are Cabibbo suppressed. Experimentally the D_s^* is interesting since it has been seen by only a few experiments, and its branching ratios are unknown. The decay of the vector D_s^*, to its pseudoscalar form D_s, was first seen by [64]. Only one group [65] reports on the diffractive production of the D_s^* in a neutrino experiment.

7.2.1 Theory

The D_s^* decays exclusively via:

$$D_s^{*\pm} \to \gamma D_s^{\pm}, \tag{7.16}$$

since the strong decay to $\pi^0 D_s^{\pm}$ is forbidden by isospin. The photon produced in this decay can be detected in our heavy liquid bubble chamber, and can serve as the necessary signature to see the D_s^*. Decays of π^0's that are expected to be a source of background, will be checked by the Monte-Carlo. The D_s branching ratios have not been measured. The observed decays include:

$$D_s^{\pm} \to \phi(n\pi) \;\; (n = 1, 2, 3) \tag{7.17}$$

with [67] reporting also a $K^+K^-\pi$ decay mode. To maximize the signal, we look for a $\phi\pi$ system, that will include all of the above decay modes. The $\phi\pi$ system is not necessarily the whole meson, but it is heavier and selected to be more energetic than any possible remaining fragment, So it is treated as if it were the D_s. For example, since the radiative decay is a two body process, the energy of the photon is a constant in the D_s^* rest frame. Following [65], the spread in photon energy is assumed to be small in the $\phi\pi\gamma$ rest system that we detect. The Lund Monte-Carlo tests this assumption, and indicates a spread in photon energy of $\sim 22\%$ when the experimental resolution is taken into account.

7.2.2 Event Selection

The events initially selected are those with at least 4 prongs, none of which is identified as an electron or proton, and at least one primary vee that is consistent with being an electron pair. To keep only charged current events, one of the tracks must be identified as a negative muon. Kaon and pion masses are assigned to tracks to form all combinations of $K^+K^-\pi$. Each combination is treated as a separate event until the final step of the analysis. The following cuts reduce the background of unwanted events:

1. The mass of the $K^+K^-\pi^+$ must be no more than the D_s mass of $1.97Gev/c^2$. Because of our mass resolution, this cut was expanded to $M_{KK\pi} < 2.2GeV/c^2$.

2. Mass of the K^+K^- must lie in the ϕ region. Several different cuts were tried using the Monte-Carlo, because of our poor mass resolution of $\sim 0.05GeV/c^2$. The final preferred choice was $M_{KK} < 1.15GeV/c^2$ (Fig. 7.8).

3. The largest source of photon background originates from decays of π^0's. To eliminate some of these, we initially eliminated any pair of photons that make a π^0 mass ($0.10 < M_{\gamma\gamma} < 0.17GeV/c^2$). After the Monte-Carlo studies, it

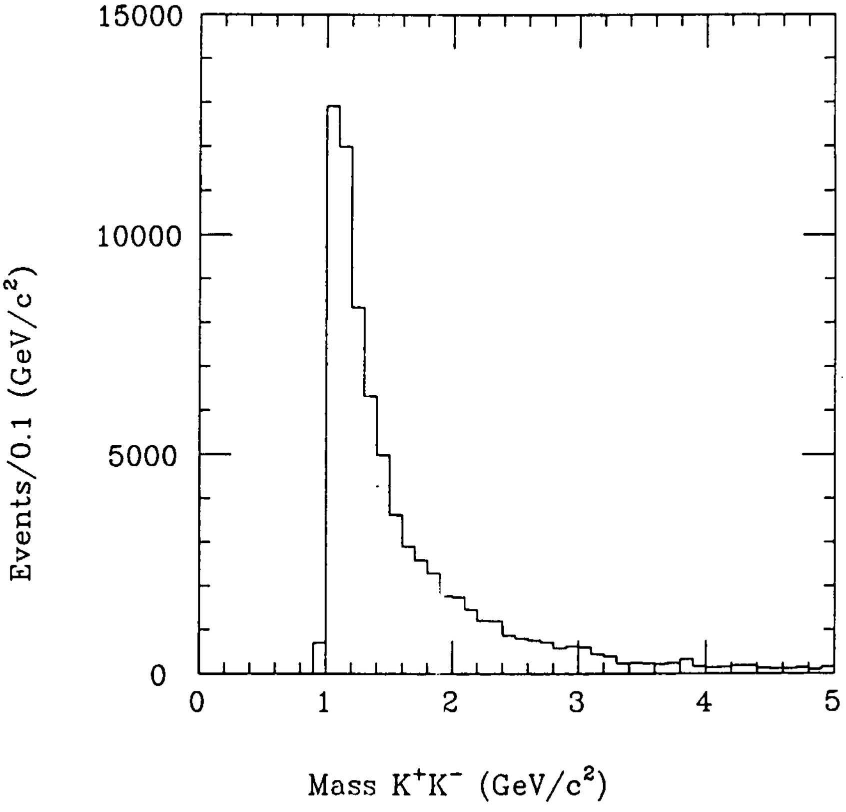

Figure 7.8: Mass of all K^+K^- combinations.

was found to be impossible to impose a set of criteria on the data which reduced the background without destroying much of the signal.

4. Particles produced from a diffractive process, because of the glancing nature of the interaction, carry a large fraction of the energy transfer. In the picture presented earlier, the W^+ converts to a virtual D_s^{*+} that materializes as a real particle, and is expected to carry most of the available energy. The most effective selection for diffractive production utilizes the z parameter, where z is defined as the energy of the particle divided by the energy transfer ν. The actual z of the D_s^* can only be approximated since we only observe the $\phi\pi\gamma$ system. The approximation used is [65]:

$$z(D_s^*) = \frac{z(\phi\pi\gamma)M(D_s^*)}{M(\phi\pi\gamma)}, \tag{7.18}$$

where $M(D_s^*) = 2.11 GeV/c^2$. Only events with $z > 0.7$ were further considered (Fig. 7.9).

5. As seen in the previous analysis of coherent events, the momentum transfer t from the W^+ to the nucleus, plays an important role in the cross section. A plot of the t distribution for events remaining after the previous cuts, is presented in Fig. 7.10. The concentration of events at low t is evident. To select the diffractive events and reduce the background, we require $t < 1.0(Gev/c)^2$.

6. Another characteristic of the events is a low Q^2, and therefore also a low x. The x distribution is presented in Fig. 7.11 after the z and t cut. The region selected for our final sample is $x < 0.3$.

The D_s^* signal, after these cuts, should show up as an approximately monoenergetic distribution of the γ's in the $\phi\pi\gamma$ rest frame. We first check this with the Monte-Carlo.

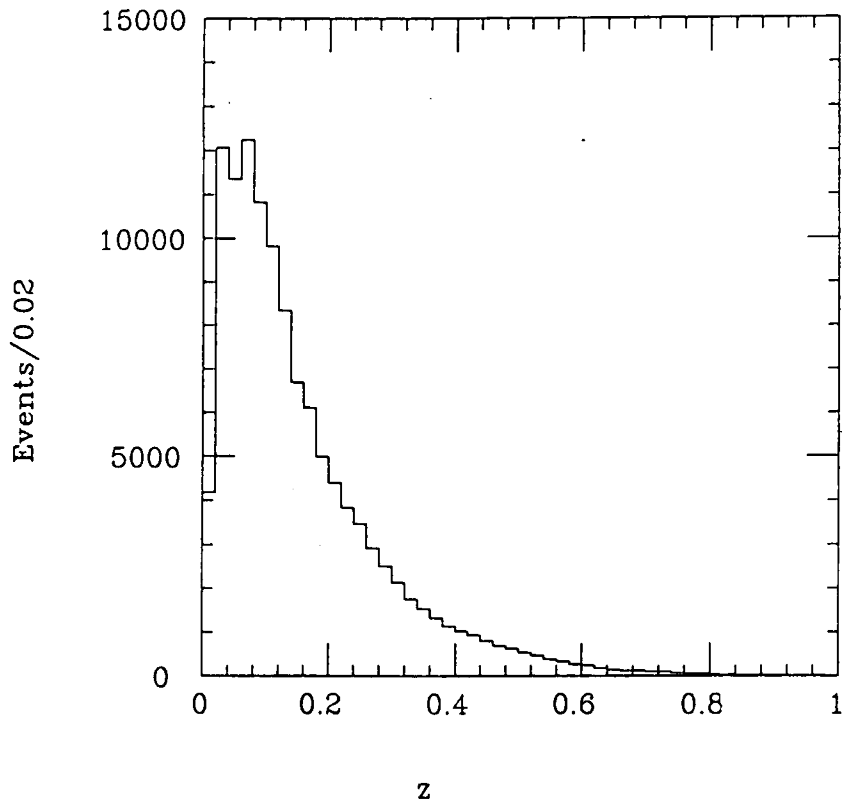

Figure 7.9: z distribution of the candidate $\phi\pi\gamma$'s.

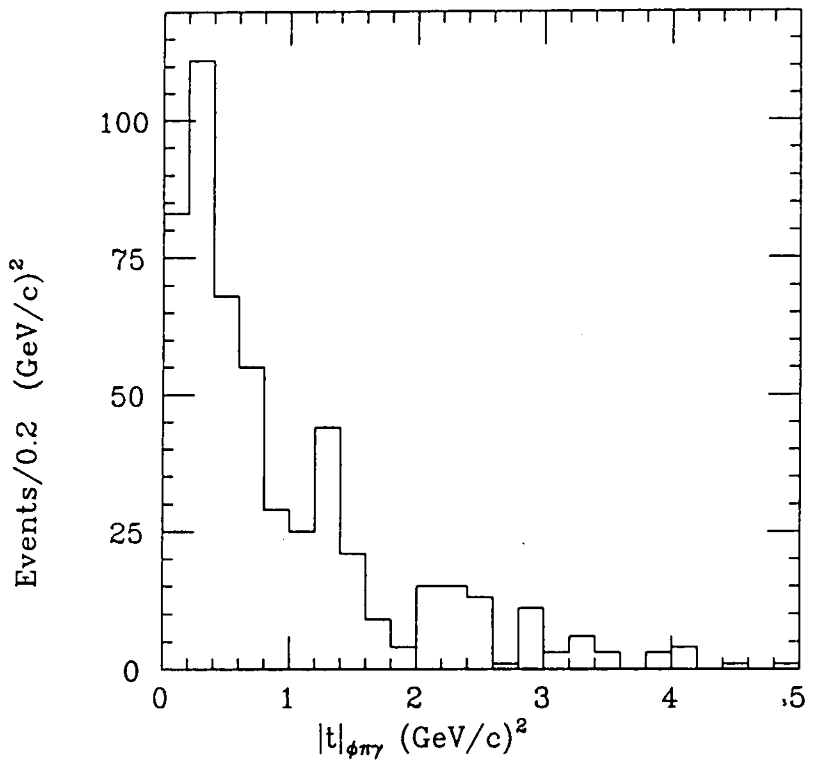

Figure 7.10: t distribution of the candidate $\phi\pi\gamma$'s after the $z > 0.7$ cut.

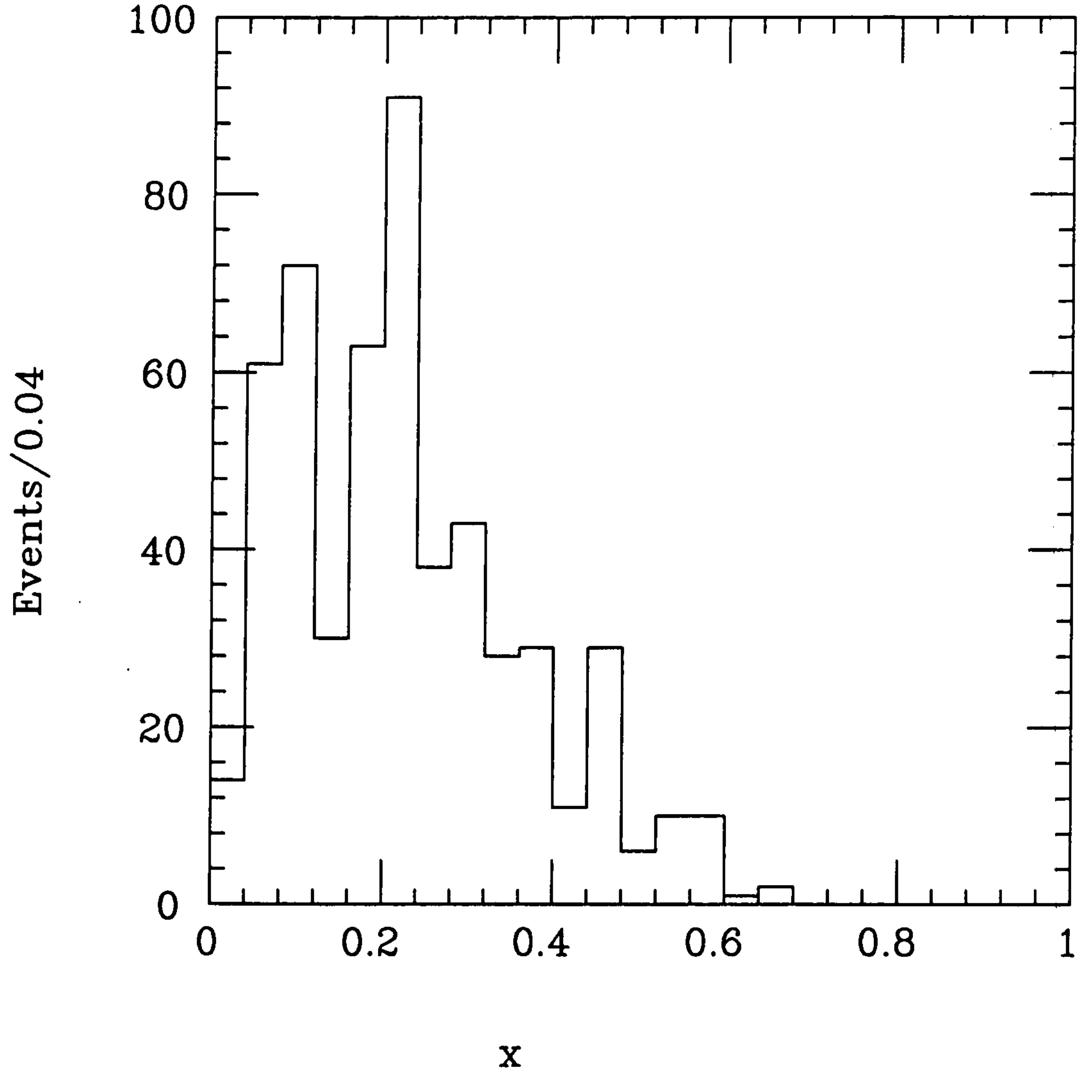

Figure 7.11: x distribution of the candidate $\phi\pi\gamma$'s after the $z > 0.7$ cut.

7.2.3 The D_s^* Monte-Carlo

To check the effectiveness of our selection process, the Lund Monte-Carlo was modified to produce the D_s^* in a diffractive fashion. The events are taken at the jet stage before the fragmentation is performed. The Monte-Carlo is set to give the necessary minimum of energy and momentum to the spectator di-quark. The energy and momentum for the D_s^* are taken from the W^+. In accordance with our diffractive hypothesis, the D_s^* takes most of the energy, and its transverse momentum is calculated from an exponential t distribution typical of diffractive processes. Finally to balance energy and momentum in the event, the parameters of the single struck quark are adjusted. The event is then fragmented.

The Lund model includes in it several decay modes of the D_s that have never been seen, such as the semi-leptonic modes (expected from analogy with the charmed meson D). Since there is some uncertainty as to the branching ratios of these decays, we concentrated only on the experimentally seen decays involving a ϕ in the decay products. The calculations are performed as if the D_s decays exclusively through a ϕ, so depending on what the branching ratios actually are, the results presented will have to be modified.

To provide a background to the pure D_s^* signal, the normal Monte-Carlo, which rarely produces the D_s^*, is run through the same analysis. Fig. 7.12 presents the two resulting curves from the same number of events. It is clear that the D_s^* signal peaks at a higher energy in the $\phi\pi\gamma$ rest frame, but it is disappointingly wide. Reference [7] claims that the D_s^* can be produced at a rate of up to 5% of the charged current cross section. Using this number, the resulting curve is presented in Fig. 7.12 as the dashed line. A quick estimation indicates that to get a one sigma effect in our experiment would require $\simeq 5,000$ charged current events, a number much larger than we actually have. A hydrogen bubble chamber, if it was big enough to see a large fraction of the photons, should do better because of its

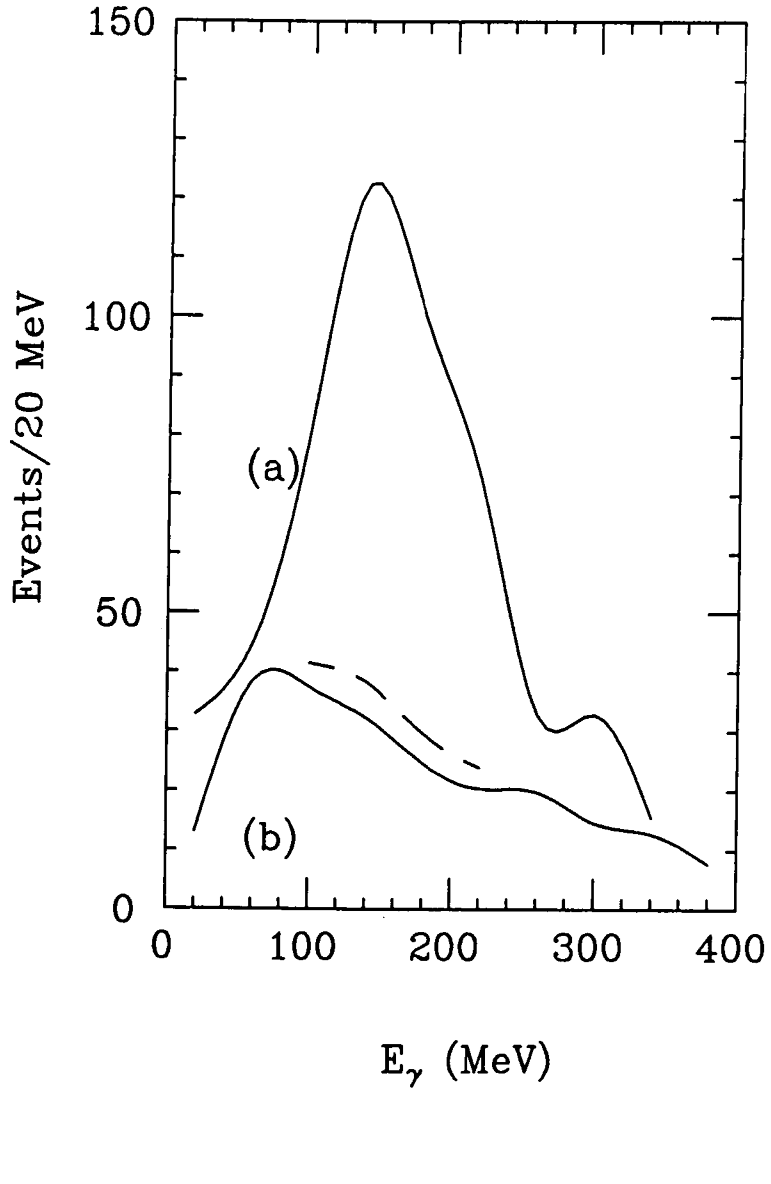

Figure 7.12: Monte-Carlo prediction for (a) The D_s^* photon signal if produced in all events. (b) The background from the same number of events. The dashed curve is the expected experimental curve using an estimate of 5% rate for D_s^* production.

superior mass resolution.

The M_{KK} cut was checked in a similar manner and $M_{KK} < 1.15 Gev/c^2$ seemed to give the best D_s^* signal to background ratio. The ratio decreased when the π^0 cut was attempted on the photons, mainly because our photon acceptance was low (~ 0.45). Our data showed a possible signal with no M_{KK} cut, perhaps indicating a $K^+K^-\pi$ decay mode [67]. The Lund was allowed to decay the D_s according to its built-in decay modes, which include the $K^+K^-\pi$ among them, but again the signal to noise ratio was reduced though only by a factor of ~ 2.

The efficiency of the method presented is reduced by the low photon acceptance of our detector, by the unseen decay modes of the ϕ, and by the x and t cuts. Background events appear from using a π^0 photon instead of the radiative decay photon, or misidentified tracks in the event — either picking a track that does not belong to the D_s, or assigning a K mass to a π track.

7.2.4 The Experimental Signal

In Fig. 7.13(a) we present the photon energy spectrum for the mass cut of $M_{KK} < 1.15 GeV/c^2$. The enhancement standing out above the Monte-Carlo background is suggestive, but as we have noted above, it is unclear, based on the presumed decay parameters of the D_s^*, whether our experiment should be able to see the D_s^*. On closer examination of these events, we find that several of the events are multiple counted. This can happen when an event has several photons. As a background check, the other charge combinations (Fig. 7.13(b),(c),(d)) are shown and a similar curve away from the ϕ mass region $1.15 < M_{KK} < 1.3\ GeV/c^2$ is presented (Fig. 7.14).

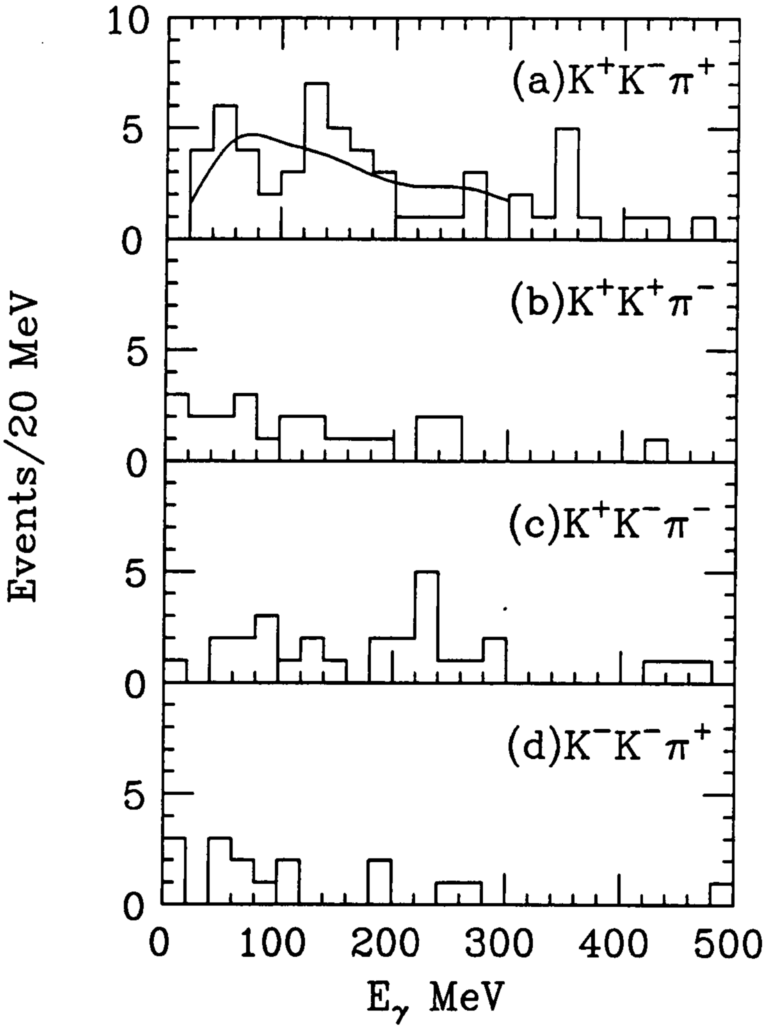

Figure 7.13: Photon energy in the $KK\pi$ rest system for different charge combinations and $M_{KK} < 1.15 GeV/c^2$.

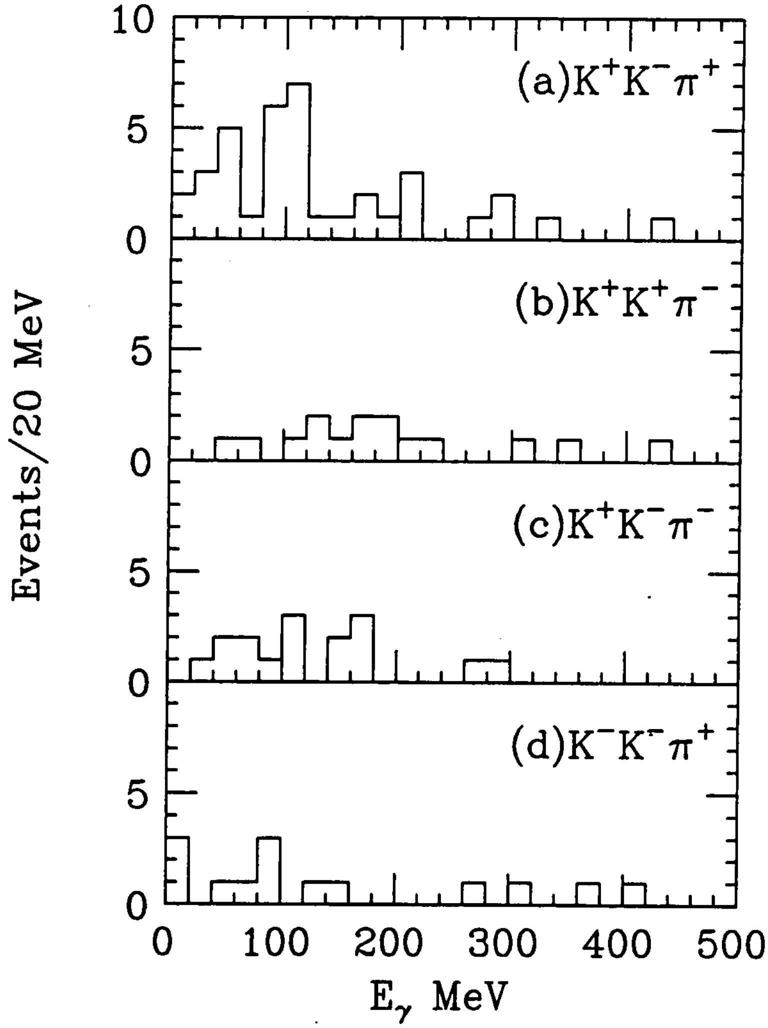

Figure 7.14: Photon energy in the $KK\pi$ rest system for different charge combinations and $1.15 < M_{KK} < 1.3\ GeV/c^2$.

CHAPTER 8

SUMMARY AND CONCLUSIONS

Analysis has been presented of the BC 72-73 and the E745 experiments. In BC 72-73, the SLAC Hybrid Facility consisting of a 40-in. hydrogen bubble chamber and a downstream detector system, was exposed to a linearly polarized photon beam, backscattered from the SLAC 30 GeV primary electron beam.

We find that the features of ρ^0 decay in inelastic diffraction $\gamma p \rightarrow$ are consistent with s-channel helicity conservation as determined from the decay angular distributions and the spin-density matrix elements. Furthermore, the inelastically produced ρ^0 displays the same mass skewing as the elastically produced ρ^0. The nucleon dissociation mass spectrum is similar to that found in pion-induced nucleon diffraction dissociation and its cross section is similar to that calculated from the vector dominance model.

The Tohoku 1m freon bubble chamber has been exposed to the Fermilab wide-band neutrino beam, generated by 800 GeV protons at the Tevatron. The data used, came mainly from the 1985 run with some preliminary data from the 1988 run, and included in the final sample, 1792 charged current neutrino events.

Coherent production of the a_1 axial vector meson has been observed through the reaction:

$$\nu Fr \rightarrow \mu^- a_1^+ Fr, \tag{8.1}$$

$$a_1^+ \rightarrow \pi^+\pi^-\pi^+, \tag{8.2}$$

with a rate of $1.1 \pm 0.47\%$ out of the total neutrino charged current rate. The predicted $a_1 - W$ coupling in the VDM, is $f_a^2/f_\rho^2 = 5.2 \pm 2.2$, which favors the model presented by [5]. The prediction of $R \simeq 0$ is shown to be plausible from the angular distributions, and the VDM is in general agreement with the data, with a slight systematic trend toward higher energies.

A Monte-Carlo study was performed to check the possibility of detecting the radiative decay of the D_s^* in our bubble chamber. Using the most favorable predicted rate through the ϕ branching ratio, it was determined that three times our data sample would be needed for a one σ effect above background.

BIBLIOGRAPHY

BIBLIOGRAPHY

[1] K.Abe, Phys. Rev. D **32**, 2288 (1985).

[2] J.J.Sakurai, Ann. Phys. (N.Y.) **11**, 1 (1960).

[3] T.H.Bauer *et al.*, Rev. Mod. Phys. **50**, 261 (1978).

[4] C.A.Piketty and P.Stodolsky, Nucl. Phys. **B15**, 571 (1970).

[5] M.K.Gaillard, S.A.Jackson, and D.V.Nanopoulos, Nucl. Phys. **B102**, 326 (1976); **B112**, 545 (1976).

[6] M.K.Gaillard, and C.A.Piketty, Phys. Lett. **68B**, 267 (1977).

[7] M.S.Chen, F.S.Henyey, and G.L.Kane, Nucl. Phys. **B118**, 345 (1977).

[8] A.Bartl, H.Fraas, and W.Majerotto, Phys. Rev. D **16**, 2124 (1977).

[9] J. Randa, in Proceedings of the XIth International Winter Meeting on Fundamental Physics, Toledo, Spain, 1983, edited by A. Ferrando (Instituto de Estrudies Nucleares, Madrid, 1983).

[10] K.Schilling, P.Seyboth, and G.Wolf, Nucl. Phys. **B15**, 397 (1970);**B18**, 332 (1970).

[11] K.Schilling, and G.Wolf, Nucl. Phys. **B61**, 381 (1973).

[12] M.Jacob, G.C.Wick, Ann. Phys. **7**, 404 (1959).

[13] S.M.Berman, M.Jacob, Phys. Rev. **139**, B1023 (1965).

[14] F.E.Close, *An Introduction to Quarks and Partons*, Academic Press, NY, 1979.

[15] K.De, Ph.D. Thesis, Brown University, 1988.

[16] T.Kitagaki, E745 note 85-02, presented Nucleophoto-II, Strasbourg, Dec. 1984.

[17] K.Furuno, Ph.D. Thesis, Tohoku University, 1986.

[18] J.Harton, Ph.D. Thesis, MIT, 1988.

[19] Alvarez Group Programming Note P-117, University of California, Lawrence Radiation Lab, 2nd Edition, June, 1966.

[20] Multi: user's guide and source files, Fermilab Programming Notes, 1984.

[21] Nuada: neutrino flux simulation program, Fermilab Programming Notes, 1983.

[22] T. Sjöstrand, University of Lund, LU-TP 85-10, October, 1985.

[23] Review of Particle Properties, Phys. Lett. **170B**, 1 (1986).

[24] T.Kafka *et al.*, Phys. Rev. Lett. **48**, 910 (1983).

[25] J.Bell *et al.*, Phys. Rev. D **19**, 1 (1979).

[26] D.Zieminski *et al.*, Phys. Rev. D **27**, 47 (1983).

[27] J.J.Aubert *et al.*, Phys. Lett. **123B**, 275 (1983).

[28] T.Kitagaki *et al.*, *A new method to investigate the nuclear effect in leptonic interactions*, Submitted to Phys. Lett.

[29] J.Ballam *et al.*, Phys. Rev. Lett. **24**, 960 (1970).

[30] F. Halzen and C. Michael, Phys Lett. **36B**, 367 (1971); A. Delesquez *et al.*, *ibid.***40B**, 77 (1972); G. Gozzika *et al.*, *ibid.*40B, 281 (1972); V. Barger and F. Halzen, Phys. Rev. Lett. **28**, 194 (1972).

[31] Y.M. Antipov *et al.*, Nucl. Phys. **B63**, 153 (1973).

[32] F. Grard *et al.*, Lett. Nuovo Cimento **2**, 305 (1971); J.V. Beaupré *et al.*;. Phys. Lett. **34B**, 160 (1971): B. Buschbeck *et al.*, Nucl. Phys. **B35**, 511 (1971): J.V. Beaupré *et al.*, *ibid.***B47**, 51 (1972); G.W. Brandenburg *et al.*, *ibid.***B45**, 397 (1972); R. Barloutaud *et al.*, *ibid.***B59**, 374 (1972).

[33] N.G.Albrow *et al.*, Nucl. Phys. **B108**, 1 (1976).

[34] G. Berlad *et al.*, Nucl. Phys. **B78**, 29 (1974).

[35] P. Bosetti *et al.*, Nucl. Phys. **B101**, 304 (1975).

[36] E. Kogan *et al.*, Nucl Phys. **B122**, 383 (1977).

[37] F. Gilman, J. Pumplin, A. Schwimmer, and L. Stodolsky, Phys. Lett. **31B**, 387 (1970).

[38] J. Pumplin, Phys. Scr. **25**, 191 (1981).

[39] E.L. Berger and J.T. Donohue, Phys Rev. D **15**, 790 (1977).

[40] K.C. Moffeit *et al.*, Phys. Rev. D **5**, 1603 (1972).

[41] G. Wolf, Nucl. Phys. **B26**, 317 (1971).

[42] K. Abe *et al.*, Phys. Rev. D **30**, 1(1984).

[43] R.C. Field *et al.*, Nucl. Instrum. Methods **200**, 237 (1982).

[44] A. Bevan *et al.*, Nucl. Instrum. Methods **203**, 159 (1982).

[45] J.E. Brau *et al.*, Nucl. Instrum. Methods **196**, 403 (1983).

[46] D. Aston *et al.*, Nucl. Phys. **B209**, 56 (1982); P.Sõding, Phys. Lett. **19**, 702 (1966).

[47] G.B. Chadwick *et al.*, Phys Rev. D **17**, 1713 (1978).

[48] H.H. Bingham *et al.*, Phys. Lett. **41B**, 635 (1972).

[49] K. Abe *et al.*, Phys. Rev. Lett. **53**, 751 (1984).

[50] P.Marage *et al.*, Phys. Lett. **140B**, 137 (1984).

[51] E632 Collaboration, contributed paper No. 40, *Neutrino 86': Neutrino Physics and Astrophysics*, proceedings of the 12th International Conference, Sendai, Japan, 1986, edited by T.Kitagaki and H.Yuta (World Scientific, Singapore, 1986).

[52] P.Marage *et al.*, Z. Phys. **C31**, 191 (1986).

[53] WA59 Collaboration, contributed paper No. 41, *Neutrino 86': Neutrino Physics and Astrophysics*, proceedings of the 12th International Conference, Sendai, Japan, 1986, edited by T.Kitagaki and H.Yuta (World Scientific, Singapore, 1986).

[54] H.J.Grabosch *et al.*, Z. Phys. **C31**, 203 (1986).

[55] H.C.Ballagh *et al.*, Phys. Rev. D **37**, 1744 (1988).

[56] D.Rein and L.M.Sehgal, Nucl. Phys. **B223**, 29 (1983).

[57] H.Faissner *et al.*, Phys. Lett. **125B**, 230 (1983).

[58] E.Ziskel, D.Rein, J.G.Morfin, Phys. Rev. Lett. **52**, 1096 (1984).

[59] F.Bergsma *et al.*, Phys. Lett. **157B**, 469 (1985).

[60] C.Baltay *et al.*, Phys. Rev. Lett. **57**, 2629 (1986).

[61] H.Abramowicz *et al.*, Phys. Lett. **107B**, 141 (1981).

[62] J.J.Aubert *et al.*, Phys. Lett. **121B**, 87 (1983).

[63] S.L.Glashow, J.Iliopoulous, L.Maiani Phys. Rev. **D2** 1285 (1970).

[64] R.Brandelik *et al.*, Phys. Lett. **80B** (1979) 412.

[65] A.E.Asratyan *et al.*, Phys. Lett. **156B** (1985) 441.

[66] H.Albrecht *et al.*, Preprint DESY 84-052, 87-156 (June 1984,1987).

[67] R.Bailey *et al.*, Phys. Lett. **139B** (1984) 320.

[68] C.Quigg, J.L.Rosner, Phys. Rev. D **17**, 239 (1978).

VITA

Joshua Shai Shimony was born in Haifa, Israel on July 4, 1958. He attended various schools in Boston and Haifa, and graduated in New-York from Newtown High School in 1975. The following September, he entered Technion-Israel Institute of Technology, and remained there until being drafted to the IDF in 1977. In 1980, after being discharged, he returned to school and graduated in February, 1982 with a Bachelor in Science in Electrical Engineering. In the fall of 1982, he accepted a teaching assistantship at the Physics Department of the University of Tennessee, Knoxville, and began studying toward a Ph.D degree. In the summer of 1983 he began working as a research assistant with the high energy group at the university.